Department of Precision and Microsystems Engineering

IMPULSE BASED SUBSTRUCTURING UNRAVELLED:
Simulation and Coupling of Structural Dynamics in the time domain

Daniël D. van den Bosch

Report no	:	EM 2014.008
Coach	:	ir. M. V. van der Seijs
Professor	:	prof. dr. ir. A. van Keulen
Specialisation	:	Engineering Mechanics
Type of report	:	MSc Thesis
Date	:	May 23, 2014

Delft
University of
Technology

Challenge the future

IMPULSE BASED SUBSTRUCTURING UNRAVELLED:

Simulation and Coupling of Structural Dynamics in the time domain

MASTER OF SCIENCE THESIS

For the degree of Master of Science in Mechanical Engineering at Delft University of Technology

Daniël D. van den Bosch

May 23, 2014

Faculty of Mechanical, Maritime and Materials Engineering (3mE) · Delft University of Technology

Abstract

One way of deriving the dynamics of a structure, is by combining the dynamics of its substructures. This concept is named 'Dynamic Substructuring' and it allows us to cope with the increasing complexity of models by dividing them into substructures and deriving their structural dynamics independently. This allows an improvement in computational efficiency. Substructuring in the frequency domain is well established nowadays, but it is not per definition best suited for simulations containing impact-like load cases. Impulse Based Substructuring (IBS) has recently been proposed allowing analysis of the high-frequency dynamics induced by these load cases more efficiently than the so-called Frequency Based Substructuring (FBS). Unfortunately IBS is not yet as mature as its frequency based counterpart. Performing a stable substructuring operation without non-physical side-effects using experimentally obtained models is at least as extensive as when done in the frequency domain. This research is performed in order to make IBS a worthy alternative to FBS. The focus of this research is twofold.

First, methods on how to obtain a structure's dynamics using its Impulse Response Functions (IRFs) are discussed. It is derived how structural dynamics can be obtained by the convolution product between the IRF and force loading history. It is discussed how this convolution product can be discretised and it is shown that an algorithm exists which assumes piecewise linear behaviour for both the IRF and the force loading history. This results in only a third order error in the obtained response compared to the response obtained by the original convolution.
Obtaining these IRFs is a challenge on its own. IRFs can be obtained either numerically, analytically or experimentally. It is shown how the IRFs of a multiple Degree of Freedom system is derived using Modal Superposition and how this relates to obtaining the system of IRFs numerically using two Newmark time integration methods. The errors made when obtaining IRFs experimentally are discussed and it is shown what effect they have on the simulated dynamics of the structure for varying load cases.
Since solving the convolution product for lengthy load cases becomes computational extensive, techniques to enhance computational performance are discussed. Among those a matrix recurrence procedure for modal contributions is proposed.

Secondly, the research focusses on the coupling procedure itself. It is explained how the convolution product is expanded to satisfy equilibrium and compatibility between the coupled substructures. It is shown that the main challenge is to accurately determine the forces acting on the interfaces between the substructures such that compatibility is maintained. Three coupling methods are discussed. The first method amounts an analytical procedure using the Laplace domain to obtain the interface forces. Secondly, the classical discrete coupling method is discussed, which satisfies compatibility explicitly to obtain the interface force every time step. Finally an inverse IRF filter approach is proposed. This approach uses the predicted uncoupled behaviour of the system to obtain the required interface forces.

Next, it is discussed how the contribution of the interface forces in the convolution product relates to the contribution of the excitation on the coupled structural dynamics. It is shown how the contributions of the interface forces are constantly compensating the uncoupled structural dynamics induced by solely the excitation, such that their combined contributions show the coupled structural dynamics. This process is very prone to errors in the IRFs. Different effects as a result of these errors cause unstable and incomplete coupling behaviour. These effects are discussed and eventually a summary is given on which criteria an IRF should satisfy in order to guarantee stable and clean substructuring.

Finally, the classical discrete approach and the inverse IRF filter approach have been tested on a case consisting of the coupling of two numerical models of a linear bar. It was seen that the used IRFs are required to be causal in order to result in a stable substructuring procedure. Furthermore it is seen that the inverse IRF filter method seems to underestimate the interface forces resulting in incomplete coupling.

Preface

This thesis is the result of my Master of Science graduation project. I was given the opportunity to fulfil this research at the Engineering Dynamics group, which is part of the department for Precision and Microsystems Engineering at Delft University of Technology.

During this research I have been supervised by Maarten van der Seijs. I highly appreciate his support during this research. Maarten has shared his expertise with great enthusiasm. His advice, feedback and support have been of great help in finding my way in this research. Besides that he has always encouraged me to go the extra mile.

Besides Maarten, I would like to thank Dennis de Klerk for his support on and off the topic off this research. Dennis' enthusiasm for technique has been an inspiration for me. Also I would like to thank Daniel Rixen and Fred van Keulen for their occasional thoughts and feedback on my topic. Both never failed to provide new insights in the discussed matter.

Finally, I would like to thank my girlfriend Ellen, my friends and my family for their love, support and patience before and during this project.

Daniël van den Bosch
May 2014

Table of Contents

Nomenclature

General meaning of often used symbols, unless mentioned otherwise in the context.

Roman symbols:

$\mathbf{B}$	Signed Boolean matrix
C	Courant's number
$\mathbf{C}$	Damping matrix
E	Young's Modulus
H	Toeplitz matrix for IRF
$\mathbf{H}$	Matrix with IRFs
$\mathbf{I}$	Identity matrix
$\mathbf{K}$	Stiffness matrix
$\mathbf{M}$	Mass matrix
$\mathbf{P}$	Projection Matrix
R	Auto-correlation matrix
$\mathbf{R}$	Rotation matrix
T	Time interval
$\mathbf{T}$	Transformation matrix
$\mathbf{V}$	Residual subspace
W	Windowing function
$\mathbf{X}$	Matrix containing eigenmodes
$\mathbf{Y}$	Receptance matrix
c	Damping coefficient or wave propagation speed
f	Force
$\mathbf{f}$	Array of forces
$\mathbf{g}$	Array of interface forces
h	Impulse Response Function
k	Stiffness
l	Length
m	Mass
$\mathbf{p}$	Array of transformed forces
$\mathbf{q}$	Array of transformed displacement responses
$\mathbf{r}$	High frequency residual
s	Laplace parameter
t	Time parameter
u	Displacement response
$\mathbf{u}$	Array of displacement responses
$\mathbf{x}$	Eigenmode
$\mathbf{0}$	Array of zeros
$\mathbf{1}_j$	Array of zeros with 1 on node j

Greek symbols:

Δ	Finite increment
Ω	Excitation frequency
α	Damping constant
β	Newmark time integration parameter or modal damping
γ	Newmark time integration parameter
δ	Dirac function
ζ	Damping ratio
η	Modal amplitude (response)
θ	Angle
κ	Modal stiffness

λ	Interface force
$\boldsymbol{\lambda}$	Array of interface forces
μ	Modal mass
ρ	Density
τ	Time parameter
ϕ	Modal participation factor
$\boldsymbol{\varphi}$	Array of modal participation factors
χ	Convolution parameter
ψ	Convolution parameter
ω	Radial Frequency
ω_d	Damped (eigen)frequency
ω_n	Natural frequency or eigenfrequency

Subscripts and superscripts:

$\star^{\mathrm{A}}$	Pertaining to substructure A
$\star^{\mathrm{HF}}$	Containing high frequency content
$\star^{\mathrm{LF}}$	Containing low frequency content
$\star^{\mathrm{RB}}$	Containing rigid body content
$\star^{inv}$	Inverse filter
$\star_n$	Pertaining to time step n
$\star_r$	Pertaining to mode r

$\star^{\mathrm{vp}}$	Virtual point transformed
$\dot{\star}$	First derivative in time
$\ddot{\star}$	Second derivative in time
$\hat{\star}$	Amplitude
$\tilde{\star}$	Approximation
$\bar{\star}$	Complex conjugate

Abbreviations:

DoF	Degree of Freedom
FBS	Frequency Based Substructuring
FIR	Finite Impulse Response
FRF	Frequency Response Function

IBS	Impulse Based Substructuring
IIR	Infinite Impulse Response
IRF	Impulse Response Function
MSP	Modal Superposition

Chapter 1

Introduction

1-1 Research context

Nowadays, engineers are faced with structures of increasing complexity. Models are getting more detailed, which inevitably leads to an increase of computational costs. Since the early applications of computers in structural analysis, computational capacity and model complexity have been involved in an ongoing struggle. Dynamic Substructuring is a concept that allows us to cope with this increasing model complexity by smart utilisation of computational capacity.

In Dynamic Substructuring, structures are decomposed into parts to be handled as an individual 'substructure.' After solving for the individual substructures, the substructures can be joined again on the interfaces were they were once parted. This decomposition allows the application of parallel computing, making computational structural analysis more efficient. An additional benefit is that assemblies can be built up from both numerically modelled parts and parts obtained from measurements.

Today, frequency domain substructuring techniques are well established in the engineering community. Those techniques are referred to as Frequency Based Substructuring (FBS) and the components dynamics are described using Frequency Response Functions (FRFs). However, when a structure is subjected to impact-like load cases (e.g. shock, blast or impulse loading), the structure is exposed to high frequent excitations. For FBS this means that a large frequency band is required, which makes this method rather inefficient for this particular purpose.

To suit the purpose of impact loading better, the time domain counter variant Impulse Based Substructuring (IBS) has been proposed.[9] In IBS the components dynamics are described using Impulse Response Functions, i.e. the time domain response to a unit impulse ($1\,[Ns]$) applied over an infinitesimally short amount of time, often referred to as "Dirac impulse".

The same substructuring approaches as used in FBS are applicable to IBS.[1] Another benefit over FBS is the fact that IBS is better suited to capture transient effects over small time intervals. The method also allows transient simulation of linear components with non-linear parts in the assembly.[17] For the purpose applying substructuring techniques real-time, IBS also seems the way-to-go since both are inherent to the time domain. Unfortunately the IBS methodology is not as mature as its frequency based counterpart. Performing a stable and clean substructuring operation using an experimentally obtained model is currently at least as extensive as when done in the frequency domain.

In order to make IBS a worthy alternative to FBS, more research needs to done on two topics. The first topic consists of the IRFs used for coupling. Obtaining the 'true' IRF from an impact measurement is ongoing research.[12] The conditions an IRF has to satisfy in order to guarantee stable and clean coupling behaviour are not yet described. Describing those would be useful, especially when one wants to fit the IRFs to these conditions. The second topic is the coupling procedure itself. Currently only one coupling method using several algorithms is described in literature. Unfortunately this method is very sensitive to errors.[8] It is therefore useful to find an alternative method and formulate what criteria need to be satisfied in order to perform successful substructuring.

1-2 Research goals

The previous section depicts plenty of opportunity for research. The first subject required to investigate is the simulation of structural dynamics using IRFs and the quality of these simulated results when using discretised functions. If the results of structural dynamics simulation without any coupling are already poor, then using this time domain methodology to couple is directly rendered useless. Numerical and experimental examples are required to validate this.

The second goal of this thesis is to identify the conditions that IRFs and the coupling procedure have to satisfy in order to guarantee stable and clean coupling behaviour. With the conditions for the IRF identified, the goal is to formulate a method allowing measured IRFs to be modified, without changing its fundamental behaviour, such that these conditions are satisfied. If successful, this should allow stable and accurate Impulse Based Substructuring using experimentally obtained models.

With the above fundaments established, the next challenge lies in improving accuracy by using smaller time steps and performance by enhancing computational efficiency. One interesting research goal is to see up to what accuracy structural dynamics can be simulated real-time. If structural dynamics can be simulated real-time, then the transition to real-time substructuring is foreseeable. Maintaining accuracy using computational efficient substructuring algorithms is a challenge on its own.

---

[1] e.g. the admittance representation and the dual assembly formulation[2]

1-3 Project outline

Before starting with the topics mentioned in the section above, a brief introduction to Dynamic Substructuring is given in chapter 2. This section briefly demonstrates the concepts using a frequency based approach.

Next, in the first part of this thesis, simulating structural dynamics using IRFs is the first subject to be discussed. The equations of motion and time-discretisation schemes are discussed in chapter 3. Next, in chapter 4 we zoom in on the IRFs themselves. It is discussed how to obtain IRFs numerically, analytically and experimentally. After this chapter, in chapter 5 a sidestep is made to the enhancement of computational performance, which is typically useful when applied in a real-time environment. Afterwards the discussed theory is applied to a test case in chapter 6. Finally this part is concluded in chapter 7.

The second part of this thesis is focussed on coupling. First it is discussed how to obtain coupled structural responses in chapter 8. This chapter will discuss several substructuring methods. Next, coupling phenomena are discussed in chapter 9. It is discussed what phenomena lead to incomplete and/or unstable substructuring and how these phenomena can be prevented. In chapter 10 the coupling methods are tested in various ways on a coupling problem. After that, chapter 11 concludes this part and this thesis.

1-4 Author's contributions

In order to extend the current state of simulations and coupling using IRFs, the following developments are proposed:

- A general notation using convolution parameters for the discretisation of the convolution product. Section 3-2-1.
- An analytical derivation of IRFs. Section 4-2 and appendix B.
- A matrix recurrence procedure for modal contributions. Section 5-3 and appendix C.
- The inverse IRF filter approach to be used for determining interface forces. Section 8-4.

Chapter 2

A brief guide into Dynamic Substructuring

This short chapter serves as a brief introduction to Dynamic Substructuring.[1] Using a short derivation it is shown how a structural response of one substructure is obtained when a coupled structure is excited. After this derivation we zoom out and give a general solution for the full structural response of the coupled system.

For the purpose of clarity of the derivation, it is chosen to use a frequency based approach. The concepts are simple, the formulas clean and the theory is analogue to the time domain approach. This guarantees a transition to the time domain approach without much difficulties later in this thesis.

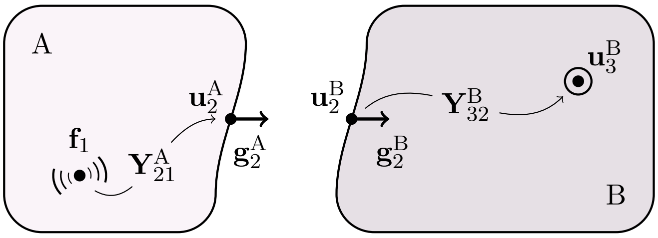

Figure 2-1: Two substructures: substructure A with the unknown excitation at node 1 and substructure B with receiver node 3.

Consider two substructures as shown in figure 2-1. Substructure A denotes a component which is excited by the vector of forces $\mathbf{f}_1$ on internal DoF vector $\mathbf{u}_1^A$. Next, substructure B will be coupled to the substructure A on DoFs $\mathbf{u}_2$. The responses to be predicted on substructure B are denoted with set $\mathbf{u}_3^B$. We assume that both substructures are subjected to an interface forces $\mathbf{g}_2$, due to the coupling. The system of equations of this assembly of

---

[1] This chapter is based on [11].

substructures can be written in block diagonal form as:

$$\begin{bmatrix} \mathbf{u}_1^{\mathrm{A}} \\ \mathbf{u}_2^{\mathrm{A}} \\ \mathbf{u}_2^{\mathrm{B}} \\ \mathbf{u}_3^{\mathrm{B}} \end{bmatrix} = \begin{bmatrix} \mathbf{Y}_{11}^{\mathrm{A}} & \mathbf{Y}_{12}^{\mathrm{A}} & \multicolumn{2}{c}{\mathbf{0}} \\ \mathbf{Y}_{21}^{\mathrm{A}} & \mathbf{Y}_{22}^{\mathrm{A}} & & \\ & & \mathbf{Y}_{22}^{\mathrm{B}} & \mathbf{Y}_{23}^{\mathrm{B}} \\ \multicolumn{2}{c}{\mathbf{0}} & \mathbf{Y}_{32}^{\mathrm{B}} & \mathbf{Y}_{33}^{\mathrm{B}} \end{bmatrix} \begin{bmatrix} \mathbf{f}_1 \\ \mathbf{g}_2^{\mathrm{A}} \\ \mathbf{g}_2^{\mathrm{B}} \\ \mathbf{0} \end{bmatrix} \tag{2-1}$$

Here the upper part contains all Frequency Response Functions[2] (FRFs) of the substructure A, whereas the lower part contains all FRFs of substructure B. In order to couple both substructures, the interface is subjected to a compatibility condition and an equilibrium condition, written respectively as:

$$\text{Compatibility:} \qquad \mathbf{B}\,\mathbf{u} = \begin{bmatrix} \mathbf{0} & -\mathbf{I} & \mathbf{I} & \mathbf{0} \end{bmatrix} \begin{bmatrix} \mathbf{u}_1^{\mathrm{A}} \\ \mathbf{u}_2^{\mathrm{A}} \\ \mathbf{u}_2^{\mathrm{B}} \\ \mathbf{u}_3^{\mathrm{B}} \end{bmatrix} = \mathbf{0} \tag{2-2a}$$

$$\text{Equilibrium:} \qquad \mathbf{g} = -\mathbf{B}^T \boldsymbol{\lambda} \tag{2-2b}$$

Here $\mathbf{B}$ represents a signed boolean matrix[3]. To determine the coupled response of $\mathbf{u}_3^{\mathrm{B}}$ due to excitation $\mathbf{f}_1$, first the equilibrium equation (2-2b) is substituted into (2-1):

$$\begin{bmatrix} \mathbf{u}_1^{\mathrm{A}} \\ \mathbf{u}_2^{\mathrm{A}} \\ \mathbf{u}_2^{\mathrm{B}} \\ \mathbf{u}_3^{\mathrm{B}} \end{bmatrix} = \begin{bmatrix} \mathbf{Y}_{11}^{\mathrm{A}} & \mathbf{Y}_{12}^{\mathrm{A}} & \multicolumn{2}{c}{\mathbf{0}} \\ \mathbf{Y}_{21}^{\mathrm{A}} & \mathbf{Y}_{22}^{\mathrm{A}} & & \\ & & \mathbf{Y}_{22}^{\mathrm{B}} & \mathbf{Y}_{23}^{\mathrm{B}} \\ \multicolumn{2}{c}{\mathbf{0}} & \mathbf{Y}_{32}^{\mathrm{B}} & \mathbf{Y}_{33}^{\mathrm{B}} \end{bmatrix} \begin{bmatrix} \mathbf{f}_1 \\ \boldsymbol{\lambda} \\ -\boldsymbol{\lambda} \\ \mathbf{0} \end{bmatrix} \tag{2-3}$$

Next the interface forces $\boldsymbol{\lambda}$ are determined by substituting (2-3) into (2-2a):

$$\boldsymbol{\lambda} = -(\mathbf{Y}_{22}^{\mathrm{A}} + \mathbf{Y}_{22}^{\mathrm{B}})^{-1}\,\mathbf{Y}_{21}^{\mathrm{A}}\,\mathbf{f}_1 \tag{2-4}$$

Finally, the response of interest is found by substituting (2-4) into the last line of (2-3)[4]:

$$\mathbf{u}_3^{\mathrm{B}} = -\mathbf{Y}_{32}^{\mathrm{B}}\,\boldsymbol{\lambda} = \mathbf{Y}_{32}^{\mathrm{B}}\,(\mathbf{Y}_{22}^{\mathrm{A}} + \mathbf{Y}_{22}^{\mathrm{B}})^{-1}\,\mathbf{Y}_{21}^{\mathrm{A}}\,\mathbf{f}_1 \tag{2-5}$$

Note that (2-5) can also be expressed in the assembled system's receptance, using

$$\mathbf{Y}_{31}^{\mathrm{AB}} = \mathbf{Y}_{32}^{\mathrm{B}}\,(\mathbf{Y}_{22}^{\mathrm{A}} + \mathbf{Y}_{22}^{\mathrm{B}})^{-1}\,\mathbf{Y}_{21}^{\mathrm{A}} \tag{2-6}$$

Where superscript AB, denotes the receptance pertains to coupled structure. In summary, the above derivation shows the response of substructure B coupled to substructure A which is being excited, i.e. $\mathbf{u}_3^{\mathrm{B}} = \mathbf{Y}_{31}^{\mathrm{AB}}\mathbf{f}_1$, based on the FRFs of the subsystems. In a more general sense this method derives the FRFs of the coupled system. Generalising the above approach for any excitation and any desired response shows

$$\mathbf{Y}^{\mathrm{AB}} = \mathbf{Y} - \mathbf{Y}\mathbf{B}^T\left(\mathbf{B}\mathbf{Y}\mathbf{B}^T\right)^{-1}\mathbf{B}\mathbf{Y} \tag{2-7}$$

which is also known as the LM-FBS method.[2]

---

[2] The FRFs in $\mathbf{Y}^{\mathrm{A}}$ and $\mathbf{Y}^{\mathrm{B}}$ are measured on the separate components.

[3] For more information on the expression of the compatibility condition using signed boolean matrices, the reader is referred to [2].

[4] Note that additional excitations on substructure B can formally be included as well by defining $\mathbf{f}_3$ and including it in the force vector in (2-3).

Part I

Structural Dynamics using Impulse Response Functions

Chapter 3

Time domain simulations with given IRFs

This chapter is dedicated to obtaining structural responses from given excitations using the structures' IRFs. First it is explained what an Impulse Response Function is and how this is used to obtain the structural response in section 3-1. Next, it is discussed how these concepts can be put into practice. Computational software often works with data which is discrete in time and space, therefore the previously derived concepts need to be rewritten to allow handling discretised data. The discretisation of the time domain is discussed in section 3-2. As it will turn out, the temporal discretisation is bound to certain limits defined by the systems properties and its spacial discretisation. Section 3-3 concludes this chapter by covering that topic.

3-1 Introduction to the convolution product

Obtaining the structural response of a system, basically boils down to solving its equation of motion for a given excitation. For a single DoF system this is

$$m\,\ddot{u}(t) + c\,\dot{u}(t) + k\,u(t) = f(t) \tag{3-1}$$

In order to solve this differential equation for a system at rest, equation (3-1) can be transformed to the Laplace domain and simplified to:

$$\Big(m\,s^2 + c\,s + k\Big)\,U(s) = F(s) \tag{3-2}$$

If we would now define function $H(s)$ as

$$H(s) \triangleq \frac{1}{m\,s^2 + c\,s + k} \tag{3-3}$$

then (3-2) rewrites to

$$U(s) = H(s)\,F(s) \tag{3-4}$$

From a frequency domain point of view $H(s)$ can be regarded as the frequency response function.[1] Using the inverse Laplace transform, (3-4) transforms to

$$u(t) = \int_0^t h(t-\tau)\, f(\tau)\, \mathrm{d}\tau \tag{3-5}$$

where the multiplication between $H(s)$ and $F(s)$ has become a convolution between $h(t)$ and $f(t)$. This integral is named the convolution product or Duhamel's integral and it shows that the structures displacements can be found by convolving the function $h(t)$ with the the given excitation $f(t)$. This function $h(t)$ represents the Impulse Response Function (IRF) and describes the displacement of the system when the system is subjected to a perfect unit impulse (Dirac function), i.e. the solution to

$$m\,\ddot{u}(t) + c\,\dot{u}(t) + k\,u(t) = \delta(t) \tag{3-6}$$

With the solution to this problem known, the convolution integral (3-5) describes how to obtain the structural response for any given excitation $f(t)$.

Let us give a detailed explanation on the interpretation of the convolution product. In equation (3-5), the IRF $h(t)$, the excitation $f(t)$ and a convolution over time are found. Starting off with the latter two; integrating a force over time yields an impulse, or a change in linear momentum. Multiplying an impulse with an IRF yields a response. However, every contribution of this impulse happens at a different moment in time, meaning their contribution to the response changes as time proceeds. Therefore (3-5) can be interpreted as a summation of the effects of a series infinitesimal impulses at times τ between 0 and t. $f(\tau)\,\mathrm{d}\tau$ represents the infinitesimal impulse at time τ. Multiplied with $h(t-\tau)$ this represents the effect of the infinitesimal impulse (after $t-\tau$ seconds) at time t. A more visual interpretation to the convolution product is given in figure 3-1.

Fortunately the methodology is easily expanded to multiple DoF systems. For a multiple DoF system, (3-5) can be expanded to

$$\mathbf{u}(t) = \int_0^t \mathbf{H}(t-\tau)\, \mathbf{f}(\tau)\, \mathrm{d}\tau \tag{3-7}$$

where $\mathbf{H}(t)$ represents the systems IRFs for every DoF in the system to one-another. $\mathbf{f}(t)$ and $\mathbf{u}(t)$ represent respectively the excitation and displacement vector. The convolution is done as before, but now includes matrix and vector algebra.

3-2 Discretisation of the convolution product

With the relation between structural response and the IRF established, let us now focus on how to implement this. The continuous formulation as derived in the previous section is directly applicable. When a continuous expression is known for both the excitations and

---

[1] A FRF is often denoted using y, rather than H, as was also seen in chapter 2. Here the choice for capital H is adapted since it denotes the Laplace transform of the IRF, usually denoted with $h(t)$.

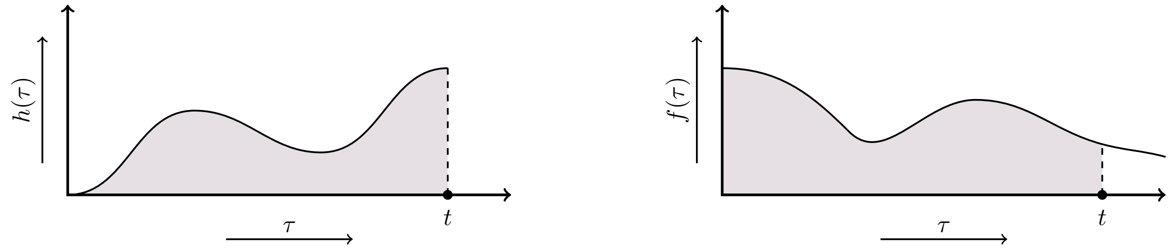

(a) The IRF $h(\tau)$, here a function of τ, visualised on interval $[0 \leq \tau \leq t]$.

(b) The excitation $f(\tau)$, also a function of τ, visualised on interval $[0 \leq \tau \leq t]$.

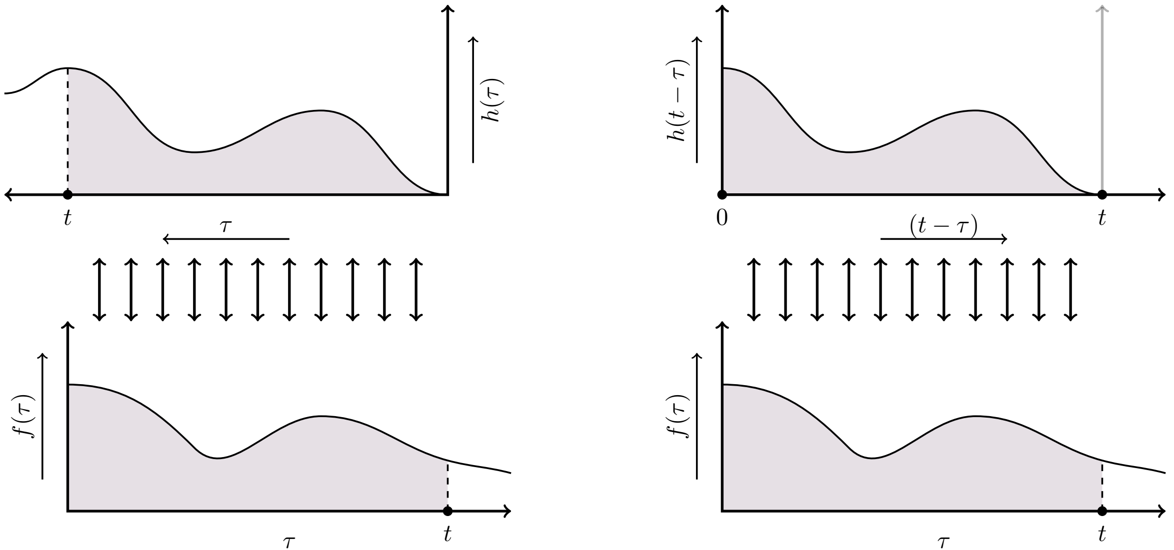

(c) $h(\tau)$ flipped such that its values are directly across of the values of $f(\tau)$ which they are multiplied with.

(d) A different interpretation of the time variable of $h(\tau)$. From point t on to the right, variable $(t-\tau)$ increases.

Figure 3-1: The calculation of the convolution product at time t illustrated. The values of $f(\tau)$ are multiplied with the values from $h(\tau)$ directly across of it and the whole is then integrated over the time interval $[0 \leq \tau \leq t]$.

the IRFs, a continuous expression can be found for the structural response. However, with increasing system size these expressions become too comprehensive. Besides that, when the goal is to apply this to experimentally obtained data a different approach needs to be formulated since experimentally obtained data does not come in analytical continuous expression. Discretising the convolution product would allow working with experimentally obtained data, however an algorithm to do so is required.

At first it was proposed in [9] to use a Cauchy product[2] to approximate the structural response

---

[2] The Cauchy product describes the discrete convolution of two sequences.

for a general applied force $\mathbf{f}(t)$, e.g. [3]

$$\mathbf{u}_n = \sum_{i=0}^{n-1} \mathbf{H}_{n-i}\, \mathbf{f}_i\, \Delta t \tag{3-8}$$

The Cauchy product for a scalar problem is illustrated in figure 3-2a.

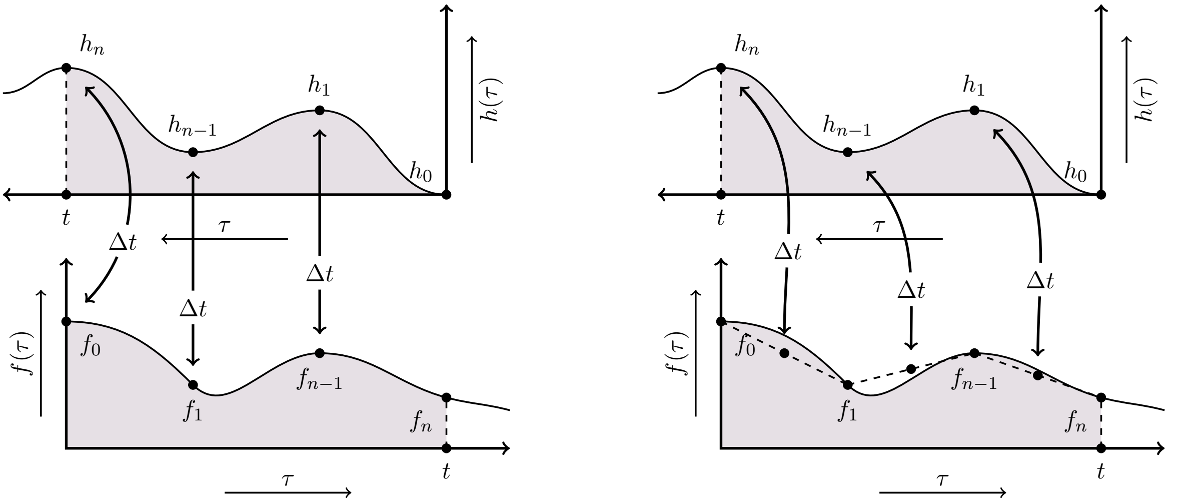

(a) Directly applied Cauchy product

(b) Cauchy product shifted forward in time with half a time step.

Figure 3-2: The Cauchy product illustrated for a scalar problem. The arrows between the $f(\tau)$ and $h(\tau)$ indicate which values are multiplied.

Now one could argue that (3-8) suggests that a response at t_1 is solely determined by an impulse caused by $\mathbf{f}_0$, while in fact if we would assume a piecewise linear forces between time steps, $\mathbf{f}_1$ would also contribute to the response at t_1. Since the impulse between the two time steps is given by

$$I_{t_0,t_1} = \frac{\mathbf{f}_0 + \mathbf{f}_1}{2}\,\Delta t$$

an alternative to (3-8) was proposed by [9] in the form of

$$\mathbf{u}_n = \sum_{i=0}^{n-1} \mathbf{H}_{n-i}\, \frac{\mathbf{f}_i + \mathbf{f}_{i+1}}{2}\,\Delta t \tag{3-9}$$

Examining (3-9), holding the piecewise linear assumption and substitute

$$\frac{\mathbf{f}_i + \mathbf{f}_{i+1}}{2} = \mathbf{f}_{i+\frac{1}{2}}$$

into (3-9) yields

$$\mathbf{u}_n = \sum_{i=0}^{n-1} \mathbf{H}_{n-i}\, \mathbf{f}_{i+\frac{1}{2}}\,\Delta t \tag{3-10}$$

---

[3] Note that $\mathbf{H}_0$ is not included in this series. This is due to the fact that this algorithm was designed for a displacement IRF and displacement remains zero at the instance the impulse is applied, e.g. $\mathbf{H}_0 = \mathbf{0}$. This is also illustrated in the above example figures.

which suggests that the original scheme in (3-8) has been shifted half a time step. This is illustrated in figure 3-2b.

In [8] an alternative is proposed in the form of

$$\mathbf{u}_n = \sum_{i=0}^{n-1} \frac{\mathbf{H}_{n-i}\mathbf{f}_i + \mathbf{H}_{n-i-1}\mathbf{f}_{i+1}}{2}\,\Delta t \tag{3-11}$$

which suggests piecewise linear behaviour of product $\mathbf{H}(t-\tau)\mathbf{f}(\tau)$ between the time steps. For the purpose of clarity and visualisation, the above expression can be rewritten to

$$\mathbf{u}_n = \mathbf{H}_n\,\mathbf{f}_0\,\frac{\Delta t}{2} + \left(\sum_{i=1}^{n-1} \mathbf{H}_{n-i}\,\mathbf{f}_i\,\Delta t\right) + \mathbf{H}_0\,\mathbf{f}_n\,\frac{\Delta t}{2} \tag{3-12}$$

This algorithm is also illustrated in figure 3-3a.

3-2-1 A general notation using convolution parameters

The algorithms for $\mathbf{u}_n$ above all show a summation of terms containing a value from $\mathbf{H}(t)$, a value from $\mathbf{f}(t)$ and (a fraction of) Δt. These terms represent intervals of the convolution product. From a different perspective, it is possible to obtain every interval of the convolution product by using two parameters to shift between possible contributions to this interval. This tends a little towards Newmark parameters,[7] although they are not similar.

Consider functions $\mathbf{H}(t)$ and $\mathbf{f}(t)$ discretised to one single interval, such that only values for $\mathbf{H}_0$, $\mathbf{H}_n$, $\mathbf{f}_0$ and $\mathbf{f}_n$ are known. Implementing these convolution parameters gives

$$\begin{aligned}\mathbf{u}_n &= \int_0^{t_n} \mathbf{H}(t_n-\tau)\,\mathbf{f}(\tau)\,\mathrm{d}\tau \\ &\simeq \frac{1-\chi}{2}\Delta t\,(\mathbf{H}_0\,\mathbf{f}_n + \mathbf{H}_n\,\mathbf{f}_0) + \chi\,\Delta t\,(\psi\,\mathbf{H}_0\,\mathbf{f}_0 + (1-\psi)\,\mathbf{H}_n\,\mathbf{f}_n)\end{aligned} \tag{3-13}$$

The response for $\mathbf{u}_n$ is build using two different types of terms. First, terms that are directly across one another in the convolution product, i.e. $\mathbf{H}_0\,\mathbf{f}_n$ and $\mathbf{H}_n\,\mathbf{f}_0$ and terms that are on different sides of the convolution interval, i.e. $\mathbf{H}_0\,\mathbf{f}_0$ and $\mathbf{H}_n\,\mathbf{f}_n$, which we can denote as cross-terms. Between these cross-terms a distinction can again be made by cross-terms that occur earlier in time, $\mathbf{H}_0\,\mathbf{f}_0$ and cross-terms that occur later in time $\mathbf{H}_n\,\mathbf{f}_n$. For the general algorithm these cross terms are illustrated in figure 3-3b, where the 'early' terms are depicted in blue and the 'late' terms in red. Figure 3-3a for example depict contributions of the terms that are directly across, or direct terms.

In this notation, the χ parameter determines the balance between cross-terms and direct terms. The ψ parameter determines, in case the cross-terms participate, how the balance lies between the 'early' $\mathbf{H}_0\,\mathbf{f}_0$ and the 'late' $\mathbf{H}_n\,\mathbf{f}_n$ -term. If this method is expanded to n time steps, the general convolution algorithm gives

$$
\begin{aligned}
\mathbf{u}_n = {} & \frac{1-\chi}{2}\Delta t(\mathbf{H}_0\,\mathbf{f}_n + \mathbf{H}_n\,\mathbf{f}_0) + \sum_{i=1}^{n-1}(1-\chi)\,\Delta t\,\mathbf{H}_{n-i}\,\mathbf{f}_i \\
& + \sum_{i=1}^{n}\chi\,\Delta t(\psi\,\mathbf{H}_{n-i}\,\mathbf{f}_{i-1} + (1-\psi)\mathbf{H}_{n-i+1}\mathbf{f}_i)
\end{aligned}
\tag{3-14}
$$

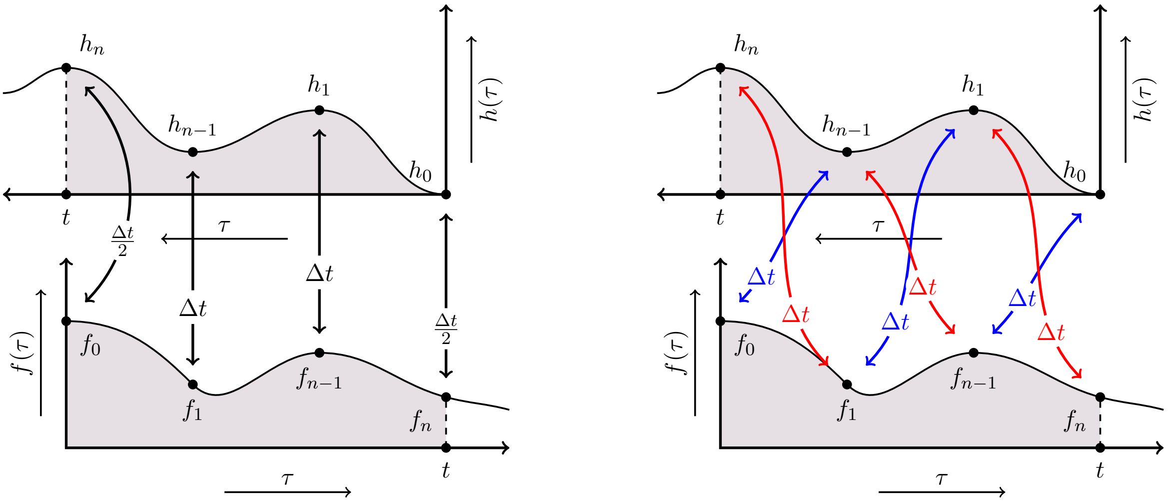

(a) Piecewise linear product of $h(t-\tau)$ and $f(\tau)$, the result of $\chi = 0$

(b) 'Late' (red), $\chi = 1$, $\psi = 0$ and 'Early' (blue), $\chi = 1$, $\psi = 1$

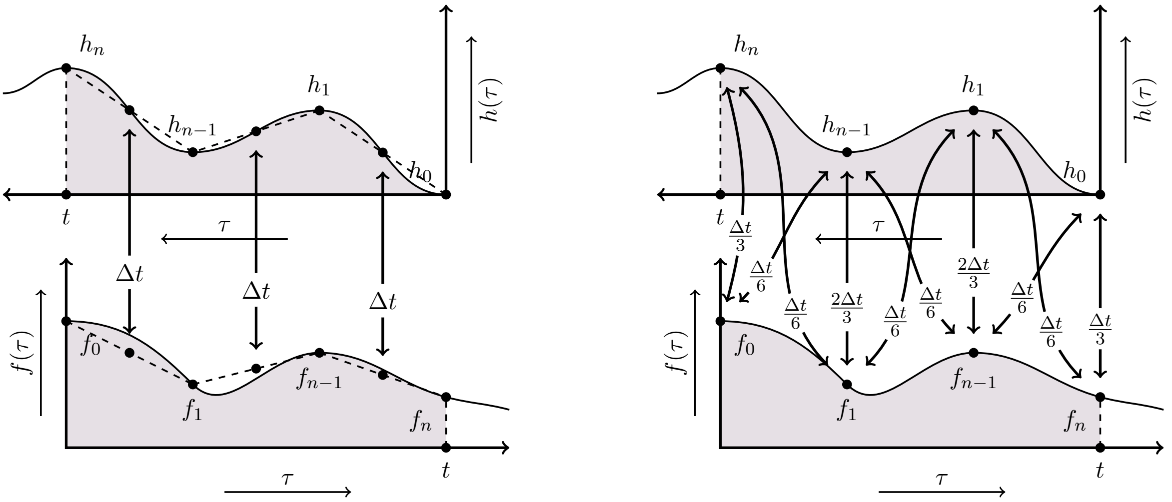

(c) Product of function averages, the result of $\chi = \frac{1}{2}$, $\psi = \frac{1}{2}$

(d) Product of piecewise linear functions, the result of $\chi = \frac{1}{3}$, $\psi = \frac{1}{2}$

Figure 3-3: Several choices for convolution parameters χ and ψ illustrated. The arrows between the $f(\tau)$ and $h(\tau)$ indicate which values are multiplied and with which time fraction.

Remark. Note that this general algorithm involving convolution parameters can only produce algorithms that are commutative for $\mathbf{H}(t)$ and $\mathbf{f}(t)$, unlike for example (3-8) and (3-9).[4]

---

[4] This means that this algorithm allows interchanging the $\mathbf{H}(t)$ and $\mathbf{f}(t)$ contributions (while taking into account matrix multiplication rules) and the result will still be the same.

Some choices of χ and ψ yield algorithms that show resemblance to the Newmark algorithms. Table 3-1 lists these combinations, figure 3-3 illustrates them.

χ	ψ	Description	Figure
0	-	Piecewise linear product	3-3a
1	0	Explicit	3-3b (red)
1	1	Implicit	3-3b (blue)
$\frac{1}{2}$	$\frac{1}{2}$	Product of function averages	3-3c
$\frac{1}{3}$	$\frac{1}{2}$	Product of piecewise linear functions	3-3d

Table 3-1: Choices for χ and ψ that show resemblance with Newmark algorithms and their descriptions.

When writing functions $\mathbf{H}(t)$ and $\mathbf{f}(t)$ as a Taylor series expansion, shows that only the algorithm using the product of piecewise linear functions, i.e. $\chi = \frac{1}{3}$ and $\psi = \frac{1}{2}$ yields a third order error. For this derivation the reader is referred to appendix A.

3-2-2 Example: free floating mass, single time step

In this example a single free floating mass m is considered which has as IRF $h(t) = \frac{t}{m}$[m/Ns], subjected to three different force functions. The first function $f_A(t)$ shows a unit step to 1 [N], i.e. a Heaviside step function. The second function $f_B(t)$ is a ramp function from 0 to 1 [N] in 1 [s]. The third function shows quadratic behaviour between up to 1 [s] and is given by $f_C(t) = \alpha t^2$. The exact answers and approximations are found in table 3-2.

Method (Equation or Parameters)	Calculation	$f_A(t)$	$f_B(t)$	$f_C(t)$
Exact (3-5)	$\int_0^1 h(1-\tau)\, f(\tau)\, \mathrm{d}\tau$	$\frac{1}{2m}\,[m]$	$\frac{1}{6m}\,[m]$	$\frac{\alpha}{12m}\,[m]$
Cauhy product (3-8)	$h_1\, f_0\, \Delta t$	$\frac{1}{m}\,[m]$	$0\,[m]$	$0\,[m]$
Cauhy product shifted (3-9)	$h_1\, \frac{f_0+f_1}{2}\, \Delta t$	$\frac{1}{m}\,[m]$	$\frac{1}{2m}\,[m]$	$\frac{\alpha}{2m}\,[m]$
Piecewise linear product (3-14) $\chi = 0$	$\frac{h_1 f_0 + h_0 f_1}{2} \Delta t$	$\frac{1}{2m}\,[m]$	$0\,[m]$	$0\,[m]$
Product of averages (3-14) $\chi = \frac{1}{2}$, $\psi = \frac{1}{2}$	$\frac{(h_1+h_0)(f_0+f_1)}{4} \Delta t$	$\frac{1}{2m}\,[m]$	$\frac{1}{4m}\,[m]$	$\frac{\alpha}{4m}\,[m]$
Product of piecewise linear (3-14) $\chi = \frac{1}{3}$, $\psi = \frac{1}{2}$	$\left(\frac{h_1 f_0 + h_0 f_1}{3} + \frac{h_0 f_0 + h_1 f_1}{6}\right) \Delta t$	$\frac{1}{2m}\,[m]$	$\frac{1}{6m}\,[m]$	$\frac{\alpha}{6m}\,[m]$

Table 3-2: Results of the different discretisation schemes.

The solutions in the first row, given by (3-5) show the exact solutions. When applying unit step force $f_A(t)$, all algorithms that use convolution parameters yield the correct answers, the two Cauchy product algorithms do not. For the ramp force step $f_B(t)$ only the product of piecewise linear functions algorithm shows the exact answer, which makes sense since both functions are linear. For the quadratic function $f_C(t)$ none of the algorithms is correct, but the the product of piecewise linear functions algorithm provides the best approximation.

3-3 Time discretisation in relation to spatial discretisation

Besides choosing a discretisation algorithm for the convolution product, time discretisaton is also subjected to another choice; the size of the time step. This section explains what conditions time discretisation is subjected to and how Courant's criterion relates this to spatial discretisation. Afterwards, it is shown how choices of different elements relate to the resulting wave propagation speeds.

3-3-1 Introduction to Courant's criterion

This section introduces Courant's criterion. In numerical analysis this criterion is, among other things, used to determine the stability limit of Newmark time integration algorithms. In chapter 9 it is shown how Courant's criterion relates to incomplete coupling of substructures.

Consider the one dimensional wave propagation formula for homogeneous material:

$$\rho\frac{\partial^2 u}{\partial t^2} = E\frac{\partial^2 u}{\partial x^2} \tag{3-15}$$

When choosing $c = \sqrt{\frac{E}{\rho}}$ (3-15) rewrites to the form known as the wave equation.

$$\frac{\partial^2 u}{\partial t^2} = c^2\frac{\partial^2 u}{\partial x^2} \tag{3-16}$$

where c now represents the wave propagation speed (also known as the speed of sound).

Courant's criterion states the following criterion for a one-dimensional problem:[1]

$$C = \frac{c'\,\Delta t}{\Delta x} \leq C_{\max} \tag{3-17}$$

Where c' represents the *wave propagation speed in the discretised system* and C represents Courant's number. The criterion states that the time interval should be chosen equal to or smaller than the time needed for a wave to travel from one spatial coordinate to the next.

Unfortunately and not very surprising, the wave propagation speed in the discretised system does not necessarily equal the wave propagation speed of the continuous system and depends on the discretisation method. The periodicity error of the time integration algorithms is a function of the chosen time step, influencing the resulting wave propagation speed.[6] Therefore the choice for c' is adopted in (3-17), rather than c to indicate this distinction.

To give a meaningful interpretation to Courant's criterion, another wave propagation speed is required, namely *the exact wave propagation speed of the spatially discretised model*, from now on denoted with c''. It is shown in [6] for the largest stable time step the relation between the resulting wave propagation speed of the discretised model and the exact wave propagation speed of the discretised model is as follows:

$$\frac{c'}{c''} = \frac{\pi}{2} \tag{3-18}$$

Next, the relation between the exact wave propagation speed of the discretised model and the highest eigenfrequency present can be established. For a model with evenly distributed elements, the highest eigenfrequency of the model represents half a wave in each element. Using the fact that the element size equals Δx, this relates to the exact wave propagation speed of the discretised model as follows:

$$\frac{c''}{\Delta x} = \frac{\omega_{cr}}{\pi} \tag{3-19}$$

Substituting both relations in (3-17) yields:

$$\boxed{C = \frac{\omega_{cr}\,\Delta t}{2} \leq C_{\max}} \tag{3-20}$$

Adopting the choice of $C_{\max} = 1$ for the Courant's number, this relation rewrites to

$$\omega_{cr}\,\Delta t \leq 2 \tag{3-21}$$

Note that this is consistent with the formulation in [6].

3-3-2 Element distribution in relation to wave propagation speed

As mentioned before, for evenly distributed elements in a model, the highest frequency in the model pertains to half a wave standing in an element. To obtain the relation between the wave propagation speed of the continuous system and the discretised system, the relation betweed the continous wave propagation speed and the elements eigenfrequency can be set up by the governing equation of an element:

$$\frac{EA}{l}[\bar{\mathbf{K}}]\,\mathbf{u} = \omega^2 ml\,[\bar{\mathbf{M}}]\,\mathbf{u} \tag{3-22}$$

Where m denotes the mass per unit length and l the length of an element. $\bar{\mathbf{K}}$ and $\bar{\mathbf{M}}$ can be interpreted as respectively the stiffness- and mass distribution matrices. They do not contain the physical quantities, but only contain information on how these quantities are distributed between the nodes. When choosing $c = \sqrt{\frac{E}{\rho}}$ and $l = \Delta x$, the above relation can be rewritten to

$$\left(\frac{c}{\Delta x}\right)^2 [\bar{\mathbf{K}}]\,\mathbf{u} = \omega^2 [\bar{\mathbf{M}}]\,\mathbf{u} \tag{3-23}$$

Where the relation between the wave propagation speed of the continuous system c and the eigenfrequency of the element ω is found by solving the eigenvalue problem. How wave propagation speed of the continuous system c relates to the wave propagation speed of the discretised system c' is then found by substitution in (3-19) and (3-18).

Matching the discretised wave propagation speed to the continuous wave propagation speed

It can be shown that there exist choice for the mass distribution that yields an wave propagation speed at the critical time step c' equal to the continuous wave propagation speed c.

Consider a single element and choose

$$[\bar{\mathbf{K}}] = \begin{bmatrix} 1 & -1 \\ -1 & 1 \end{bmatrix} \qquad \text{and} \qquad [\bar{\mathbf{M}}] = \frac{1}{2}\begin{bmatrix} 1 & 0 \\ 0 & 1 \end{bmatrix}$$

This represents a lumped mass model of a bar element. When choosing $\left(\frac{c}{\Delta x}\right) = 1$ the eigenfrequency related to the vibration of the element becomes $\omega_{cr} = 2$. Substitution in (3-19) and (3-18) then yields $\left(\frac{c'}{\Delta x}\right) = 1$, i.e. $c' = c$.

Linear bar element

When adapting the most regular choice for the distribution; the linear bar element, it turns out that the continuous wave propagation speed is not easily mimicked. The element matrices pertaining to the linear bar are:

$$[\bar{\mathbf{K}}] = \begin{bmatrix} 1 & -1 \\ -1 & 1 \end{bmatrix} \qquad \text{and} \qquad [\bar{\mathbf{M}}] = \frac{1}{6}\begin{bmatrix} 2 & 1 \\ 1 & 2 \end{bmatrix}$$

When choosing $\left(\frac{c}{\Delta x}\right) = 1$ again, the eigenfrequency related to the vibration of the element becomes $\omega_{cr} = 2\sqrt{3}$. Substitution in (3-19), giving the exact solution for the discrete model gives $\frac{c''}{\Delta x} = \frac{2\sqrt{3}}{\pi}$ and thus $c'' = \frac{2\sqrt{3}}{\pi}\, c \approx 0.91c.$. Substitution in (3-18): $\frac{c'}{\Delta x} = \sqrt{3}$ and thus $c' = \sqrt{3}\, c \approx 1.73c$. This does mean that there exists a time step Δt, such that the continuous wave propagation speed is maintained.

Summarising, it is seen that the chosen shape functions for the elements influence the wave propagation speed of the discretised model. This is due to the fact that the shape functions influence the mass distribution of the element. The highest eigenfrequency in the model, i.e. the eigenfrequency of the element is subjected to the choice of mass distribution and therefore the wave propagation speed of the discretised model is as well.

Chapter 4

Obtaining Impulse Response Functions

In order to apply the convolution products as shown in the previous chapter, the Impulse Response Functions (IRFs) of the involved structures are required. In general there are three methods to obtain an IRF; numerically, analytically or experimentally. This chapter covers all three possibilities.

Section 4-1 discusses obtaining IRFs numerically using time integration algorithms. As will turn out this method is subjected to a choice of initial conditions. To avoid the difficulties encountered with time stepping algorithms, a different approach can be taken. Section 4-2 shows how a system of IRFs can be obtained analytically using Modal Superposition (MSP).[1] A different analytical approach would be to use travelling wave equations. This approach is beyond the scope of this work, but is included in the discussion at the end of this chapter in section 4-4. Section 4-3 briefly discusses the process of obtaining IRFs experimentally.

Note that this chapter shows how to obtain IRFs for displacements $h(t)$, velocities $\dot{h}(t)$ and accelerations $\ddot{h}(t)$. As it will turn out however, not all three are evenly suited to obtain structural responses. Therefore acceleration IRFs are discussed a little more in-depth in section 4-4.

4-1 IRFs by time integration algorithms

In an early work on Impulse Based Substructuring,[9] it is shown how to use Newmark time integration algorithms[7] to obtain IRFs. The method works based on the linear(ised) equation of motion which has to be satisfied for any time t_n:

$$\mathbf{M}\,\ddot{\mathbf{u}}_n + \mathbf{C}\,\dot{\mathbf{u}}_n + \mathbf{K}\,\mathbf{u}_n = \mathbf{f}_n \tag{4-1}$$

---

[1] Under the condition that the system is proportionally damped and consequently the modes are fully uncoupled.

The time integration algorithm uses previous state and current acceleration information to calculate the current state:

$$\mathbf{u}_n = \mathbf{u}_{n-1} + \Delta t\, \dot{\mathbf{u}}_{n-1} + (0.5-\beta)\Delta t^2 \ddot{\mathbf{u}}_{n-1} + \beta\Delta t^2 \ddot{\mathbf{u}}_n \tag{4-2a}$$

$$\dot{\mathbf{u}}_n = \dot{\mathbf{u}}_{n-1} + (1-\gamma)\Delta t \ddot{\mathbf{u}}_{n-1} + \gamma\Delta t \ddot{\mathbf{u}}_n \tag{4-2b}$$

The accelerations of the current time step are obtained by solving:

$$(\mathbf{M} + \gamma\Delta t\mathbf{C} + \beta\Delta t^2\mathbf{K})\ddot{\mathbf{u}}_n = \mathbf{f}_n - \mathbf{K}\tilde{\mathbf{u}}_n - \mathbf{C}\tilde{\dot{\mathbf{u}}}_n \tag{4-3}$$

where $\tilde{\mathbf{u}}_n$ and $\tilde{\dot{\mathbf{u}}}_n$ are predictors

$$\tilde{\mathbf{u}}_n = \mathbf{u}_{n-1} + \Delta t\dot{\mathbf{u}}_{n-1} + (0.5-\beta)\Delta t^2\ddot{\mathbf{u}}_{n-1}$$
$$\tilde{\dot{\mathbf{u}}}_n = \dot{\mathbf{u}}_{n-1} + (1-\gamma)\Delta t\ddot{\mathbf{u}}_{n-1}$$

Since every next step depends on the previous step, initial conditions need to be chosen. In [9] three possible choices are discussed.

- **Initial velocity step:**

  $$\mathbf{u}_0 = \mathbf{0} \qquad \dot{\mathbf{u}}_0 = \mathbf{M}^{-1}\mathbf{1}_j \qquad \ddot{\mathbf{u}}_0 = \mathbf{M}^{-1}(-\mathbf{C}\dot{\mathbf{u}}_0) \tag{4-4}$$

  This choice is based on the impulse equation for the system of equations which states

  $$\mathbf{M}\,\Delta\dot{\mathbf{u}}(0) = \int_0^{t+} \mathbf{f}(t)\,\mathrm{dt} \tag{4-5}$$

  Where $\mathbf{f}(t)$ describes a perfect Dirac impulse on node j, such that

  $$\int_0^{t+} \mathbf{f}(t)\,\mathrm{dt} = \mathbf{1}_j \tag{4-6}$$

  For this choice the initial velocity vector is set accordingly and the applied force $\mathbf{f}(t)$ is set to zero.

- **Initial applied force:**

  $$\mathbf{u}_0 = \mathbf{0} \qquad \dot{\mathbf{u}}_0 = \mathbf{0} \qquad \mathbf{f}_0 = \mathbf{1}_j\frac{2}{\Delta t} \quad \text{hence} \quad \ddot{\mathbf{u}}_0 = \mathbf{M}^{-1}\mathbf{1}_j\frac{2}{\Delta t} \tag{4-7}$$

  This choice is based on describing the impulse as a force on the initial time step which eventually has to result in the system responding when applying the time integration algorithm. The unity force is multiplied by $\frac{2}{\Delta t}$ because the resulting force vector represents a unit force at time $t = 0$ decreasing linearly to 0 at time $t = \Delta t$ representing an impulse of $\frac{\Delta t}{2}$.

- **Applied force at the second time step:**

  $$\mathbf{u}_0 = \mathbf{0} \qquad \dot{\mathbf{u}}_0 = \mathbf{0} \qquad \ddot{\mathbf{u}}_0 = \mathbf{0} \qquad \mathbf{f}_1 = \mathbf{1}_j\frac{1}{\Delta t} \tag{4-8}$$

  This choice offers an alternative to the initial applied force choice, when factorising the mass matrix is significant in cost. This choice prevents that. Note that a unit force at time $t = t_1$, represents a linear increasing force between t_0 and t_1 and linear decreasing force between t_1 and t_2 and therefore needs to be divided by Δt to represent a unit impulse.

Starting at the initial conditions, the IRF is obtained using the Newmark time integration algorithm. As discussed in section 3-3-1, the time step Δt has to satisfy Courant's criterion. For different Newmark parameters, different maximum Courant numbers C_{max} apply[6] in order to guarantee stability in the time integration algorithm. Popular choices range from 1 to 1.73 (central difference, Fox & Goodwin and linear acceleration), while others are unconditionally stable, e.g. average constant acceleration.

4-1-1 Discussion on initial conditions and Courant's number

It can be discussed which of the initial conditions is preferred. However, as it will turn out, there is no best choice for every scenario. Apparently the choice of time step (which relates directly to the Courant's number) influences the performance of the different situations. In this discussion the applied force at the second time step choice is not considered.

To illustrate the effects of choosing for an initial velocity or initial force condition, a numerical model of an unconstrained bar is used. The model of the bar uses has a length of $l = 1.026\,[m]$ divided in 50 elements of equal length. Furthermore the bar has Young's modulus $E = 3.1\,[GPa]$, density $\rho = 1330\,[kg/m^3]$ and diameter of $D = 0.04\,[m]$. The driving point IRF of the most left node is considered. As a reference solution, an IRF by Modal Superposition (MSP) is considered. As will be shown in section 4-2, the MSP solution provides the exact solution for the numerical model. The Newmark solutions use the averaged constant acceleration algorithm, i.e. $\beta = \frac{1}{4}$, $\gamma = \frac{1}{2}$, which has the property to be unconditionally stable.

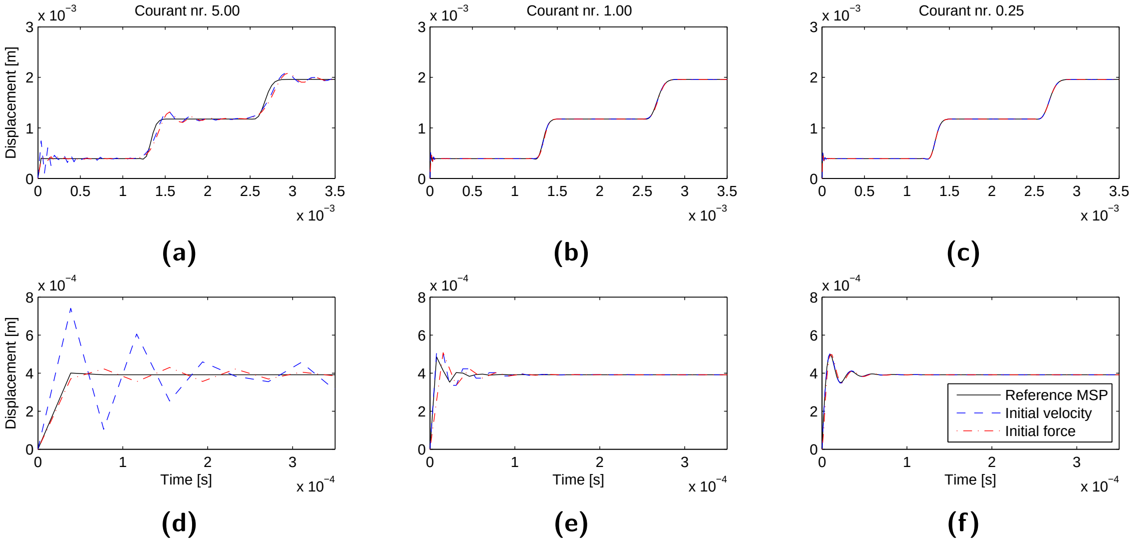

Figure 4-1: Driving point IRF for Courant numbers 5, 1 and 0.25 using the initial velocity condition, the initial force condition and a reference solution.

Figure 4-1 shows the considered driving point IRF for the first $3.5\,[ms]$ for various Courant numbers in figures 4-1a to 4-1c and zoomed in to the first $0.35\,[ms]$ in figures 4-1d to 4-1f. For Courant's number 0.25 it is seen that both initial conditions make a very decent approximation to the reference solution. For Courant's number 1, figure 4-1e it appears that the initial force condition is one time step delayed compared to the initial velocity condition. Finally for Courant's number 5, another effect emerges. Both method show some overshoot compared to the reference solution, although the overshoot of the initial velocity condition is more severe than the overshoot of the initial force condition. Besides that, the peaks of the initial force condition again appear to be one time step delayed compared to the initial velocity condition.

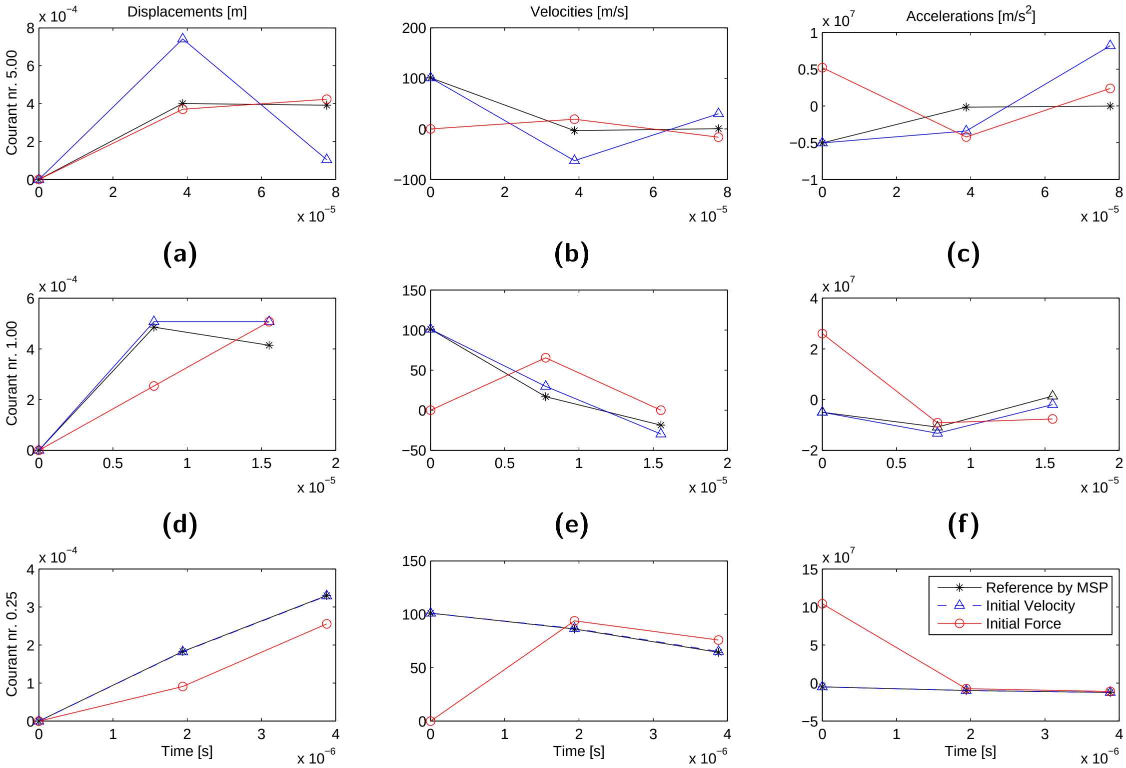

(a) (b) (c)

(d) (e) (f)

(g) (h) (i)

Figure 4-2: Times t_0, t_1 and t_2 for displacement, velocity and acceleration IRFs using Courant numbers 5, 1 and 0.25, obtained using the initial velocity choice, the initial force choice and a reference solution.

Figure 4-2 together with equation (4-2) provides the insights to explain these effects. Figure 4-2 shows the first two time steps after $t = 0$ for the same conditions and Courant numbers in terms of displacements, velocities and accelerations. The delay the initial force condition shows can be assigned to the fact that the velocity jump caused by the impulse now occurs effectively half a time step later, as is best illustrated in 4-2h. The initial velocity condition gives an exact match on every quantity at $t = 0$, so solely based on that, it seems the to be the better choice. However, for Courant numbers $C > 1$ the overshoot of the initial velocity condition is quite severe, best illustrated in figure 4-2a. This can be assigned to the fact that the contribution of the initial velocity due to the large time step has now become dominant for the displacement, which again has a significant influence on the accelerations for the next time step. Since for the displacement IRF, the velocities have become dominant over the accelerations, the effect is not so severe for the initial force condition which has no initial velocity.

Another visible effect is the increase of acceleration at time $t = 0$ for a decrease in time step when the initial force condition is used. The acceleration at this time describes the acceleration required to obtain the velocity the system has at the next time step as a result of the impulse. As Δt decreases, the required acceleration increases. This does make the obtained acceleration IRF valid on $t = 0$. The initial velocity IRF however, lacks to show what acceleration results in this high velocity at the initial time step. Therefore the obtained acceleration IRF using the initial velocity condition is not valid on $t = 0$.

4-2 Analytical derivation of IRFs

The previous section showed that the accuracy of IRFs obtained by Newmark time integration algorithms are subjected to choice of initial conditions and time step size. Instead of using a Newmark time integration algorithm, it is possible to obtain the IRF analytically, without being dependent on the time step sizing. This section covers the basics for single DoF systems covering conservative and non-conservative harmonic oscillation, complemented by the basics for rigid body motion. These system are built using a mass, spring and/or damper. These IRFs form the basis for the IRFs of the modes of a multiple DoF system. Next it is shown how the IRFs of a multiple DoF system are obtained using MSP of these modes. The extended derivations of this section are found in appendix B.

Unless denoted otherwise, all analytical expressions given for IRFs apply for $t \geq 0$. The expressions for acceleration IRFs apply for $t > 0$.

4-2-1 Vibrational motion single DoF system

First the systems containing a spring, resulting in vibrational motion are discussed. First some basics of the derivation of IRFs are covered while obtaining the IRF of the conservative system. Next, this derivation is expanded to a general form which covers non-conservative motion.

Conservative system

A mass spring system, as seen in figure 4-3a, excited by a perfect Dirac impulse is subjected to the following equation of motion:

$$m\,\ddot{u}(t) + k\,u(t) = \delta(t) \tag{4-9}$$

The homogeneous part, representing free motion can be solved by defining eigenfrequency $\omega_n \triangleq \sqrt{\frac{k}{m}}$ and solving:

$$\ddot{u}(t) - \omega_n^2\,u(t) = 0 \tag{4-10}$$

Two complex exponential functions satisfy this differential equation, $u(t) = \alpha_1\,e^{i\,\omega_n\,t}$ and it's complex conjugate $u(t) = \alpha_2\,e^{-i\,\omega_n\,t}$. Together they are able to combine either $u(t) = \alpha_3\,\cos(\omega_n\,t)$, $u(t) = \alpha_4\,\sin(\omega_n\,t)$ or a combination of both which are able to give a more physical interpretation to the motion.

Now in search of the particular solution, when applying the Dirac impulse the system has to satisfy impulse equation

$$m\,\Delta\dot{u} = \int_0^{t+} \delta(t)\,\mathrm{dt} = 1 \tag{4-11}$$

which states that a jump in velocity occurs as a result of applying the Dirac impulse. Assuming the system is initially at rest, the velocity as a result of the impulse is given by

$$\hat{\dot{u}} \triangleq \Delta\dot{u} = \frac{1}{m} \tag{4-12}$$

where $\hat{\dot{u}}$ now represents the initial velocity of the mass $\dot{u}(0)$. The initial displacement is assumed to equal 0, i.e. $u(0) = 0$.

The full equation of motion, assuming the system is initially at rest and that the applied Dirac impulse leads to a jump in velocity at $t = 0$ is then solved by filling in the cosine function for $\dot{u}(t)$. Hence,

$$\dot{u}(t) = \hat{\dot{u}}\,\cos\omega_n t \tag{4-13}$$

The primitive function of (4-13) then gives the following IRF for the displacements:

$$u(t) = \frac{\hat{\dot{u}}}{\omega_n}\,\sin\omega_n t = h(t) \tag{4-14}$$

And a solution for the acceleration IRF can be found by taking the derivative of (4-13):

$$\ddot{u}(t) = -\omega_n\,\hat{\dot{u}}\,\sin\omega_n t \tag{4-15}$$

These IRFs can now be used to determine the systems response to an arbitrary excitation using the convolution product (3-5).

Non-conservative system

When damping is added to the system, as seen in figure 4-3b, a non-conservative system is obtained. Unfortunately the derivation of its IRF is not as straight forward as above. When this single DoF system is excited by a perfect Dirac impulse, the system is subjected to the following equation of motion:

$$m\,\ddot{u}(t) + c\,\dot{u}(t) + k\,u(t) = \delta(t) \tag{4-16}$$

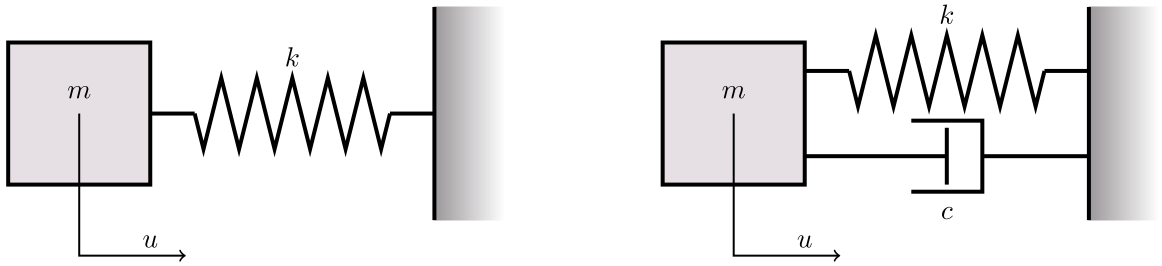

(a) Mass-spring system as example for the conservative harmonic motion IRF.

(b) Mass-spring-damper system as example for the non-conservative harmonic motion IRF.

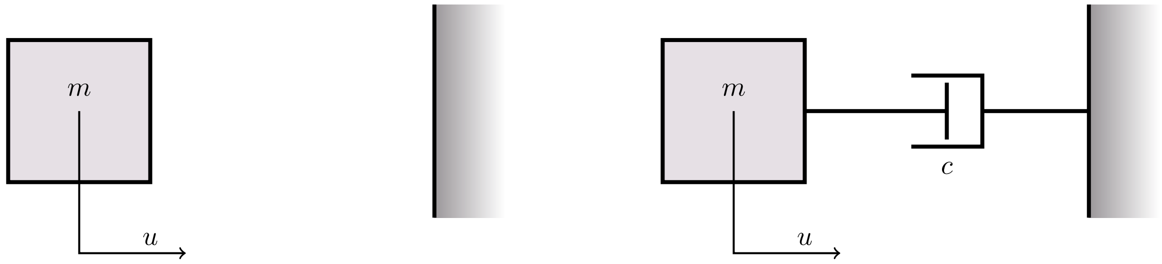

(c) Free floating mass as example for the undamped Rigid Body motion.

(d) Mass-damper system as example for the damped Rigid Body motion

Figure 4-3: Four different systems subjected to a Dirac impulse. For all systems the IRF is derived in this section.

It may be useful to define some parameters related to this problem on forehand of solving it:

$$
\begin{aligned}
\omega_n &\triangleq \sqrt{\frac{k}{m}} \\
\zeta &\triangleq \frac{c}{2\sqrt{m\,k}} = \frac{c}{2\,m\,\omega_n} \\
\omega_d &\triangleq \omega_n\sqrt{1-\zeta^2} = \sqrt{\omega_n^2 - \zeta^2\,\omega_n^2} \\
\theta &\triangleq \tan^{-1}\frac{\zeta\,\omega_n}{\omega_d}
\end{aligned}
$$

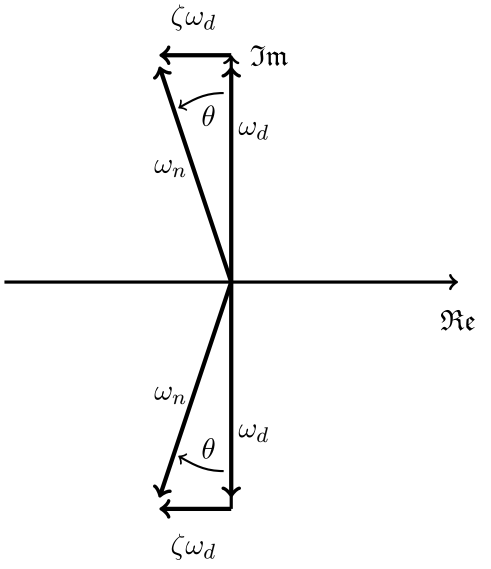

Figure 4-4: Relation between frequencies, damping ratio and angle visualised.

Here ω_n denotes the eigenfrequency of the undamped system. Since the system is damped, the damping ratio is specified, denoted with ζ. As will be shown, this has its influence on the eigenfrequency of the damped system, denoted with ω_d. Parameter θ represents a fictive angle between the frequencies, which will show to be useful later on. The relations between

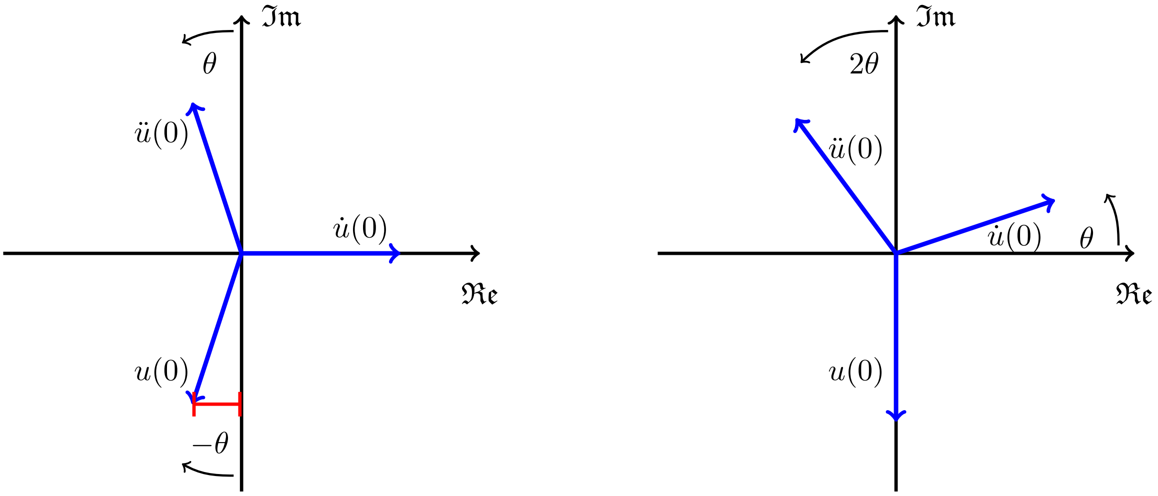

(a) The first suggested decaying cosine function for $\dot{u}(t)$.

(b) The suggested decaying cosine for $\dot{u}(t)$ shifted with angle θ.

Figure 4-5: Phase angle representation of displacement $u(t)$, velocity $\dot{u}(t)$ and acceleration $\ddot{u}(t)$. Note that the amplitudes of these quantities are not representative.

these parameters are shown in figure 4-4.

Solving (4-16), its homogeneous part has solutions $u(t) = \alpha_1\, e^{(-\zeta\,\omega_n + i\,\omega_d)\,t}$ or its complex conjugate $u(t) = \alpha_2\, e^{(-\zeta\,\omega_n - i\,\omega_d)\,t}$ whom can together combine to either a decaying cosine function $u(t) = \alpha_3 \cos(\omega_d\, t)\, e^{-\zeta\,\omega_n\,t}$, a decaying sine function $u(t) = \alpha_4 \sin(\omega_d\, t)\, e^{-\zeta\,\omega_n\,t}$ or a combination of both. In the case of critical damping the solution is found in the decaying exponential function.

Similar as for the conservative system, satisfying the impulse equation (4-11), the decaying cosine $\dot{u}(t)$, $\hat{u}$ is a solution for the system.

$$\dot{u}(t) = \hat{u}\,\frac{e^{(-\zeta\,\omega_n + i\,\omega_d)\,t} + e^{(-\zeta\,\omega_n - i\,\omega_d)\,t}}{2} = \hat{u}\,\cos(\omega_d\, t)\, e^{-\zeta\,\omega_n\,t}$$

In order to obtain the IRF for displacements, the primitive function needs to be found:

$$\begin{aligned} u(t) &= \hat{u}\,\frac{\omega_d \sin(\omega_d\, t) - \zeta\,\omega_n \cos(\omega_d\, t)}{\omega_d^2 + \zeta^2\,\omega_n^2}\, e^{-\zeta\,\omega_n\,t} \\ &= \hat{u}\,\frac{\sin(\omega_d\, t - \theta)}{\sqrt{\omega_d^2 + \zeta^2\,\omega_n^2}}\, e^{-\zeta\,\omega_n\,t} = \hat{u}\,\frac{\sin(\omega_d\, t - \theta)}{\omega_n}\, e^{-\zeta\,\omega_n\,t} \end{aligned}$$

The phase angle of the obtained IRFs are also visualised in figure 4-5a. Obviously for this solution $u(0) \neq 0$ for $\zeta \neq 0$. In fact, the phase shift θ caused by $\zeta > 0$ causes $u(0) < 0$, which is non-causal for a positive impact.

A solution would be to assume that the cosine in $\dot{u}(t)$ is shifted with θ such that:

$$\dot{u}(t) = \hat{u}^{\star} \cos(\omega_d t + \theta) e^{-\zeta \omega_n t} \tag{4-17a}$$

$$u(t) = \hat{u}^{\star} \frac{\sin(\omega_d t)}{\omega_n} e^{-\zeta \omega_n t} \tag{4-17b}$$

Now $\hat{u}^{\star}$ has to be chosen such that impulse equation (4-11) is again satisfied. Substitution of (4-17a) in (4-11) yields

$$\hat{u}^{\star} = \frac{\hat{u}}{\cos\theta} = \hat{u} \frac{\omega_n}{\omega_d} \tag{4-18}$$

After substitution the yielded expressions for displacement, velocity and acceleration as a result of a perfect Dirac impulse are

$$u(t) = \frac{\sin(\omega_d t)}{m \omega_d} e^{-\zeta \omega_n t} \tag{4-19a}$$

$$\dot{u}(t) = \frac{\omega_n}{m \omega_d} \cos(\omega_d t + \theta) e^{-\zeta \omega_n t} \tag{4-19b}$$

$$\ddot{u}(t) = -\frac{\omega_n^2}{\omega_d m} \sin(\omega_d t + 2\theta) e^{-\zeta \omega_n t} \tag{4-19c}$$

The phase angles of these IRFs are visualised in figure 4-5b. It can be seen that, when damping is reduced towards zero, the IRFs in (4-19) reduce to the conservative version. When $c \to 0$, $\zeta \to 0$ and thus $\omega_d \to \omega_n$ and $\theta \to 0$.

Obviously this does not prove that these IRFs provide the exact answer to equation (4-16). It was proven mathematically using the Laplace domain that this is in fact the case. For the full derivation the reader is referred to appendix B.

4-2-2 Rigid Body Motion single DoF system

Next the IRFs for systems undergoing Rigid Body Motion (RBM) are derived. First the undamped situation is discussed. Afterwards the influence of damping on the RBM is discussed.

Undamped rigid body motion

A rigid body, assumed to undergo undamped motion, as seen in figure 4-3c is subjected to the following equation of motion

$$m \ddot{u}(t) = \delta(t) \tag{4-20}$$

After applying the Dirac impulse the body is expected to travel at a constant velocity. Satisfying impulse equation (4-11) the IRFs for the undamped rigid body motion yield:

$$u(t) = \frac{t}{m} \tag{4-21a}$$

$$\dot{u}(t) = \frac{1}{m} \tag{4-21b}$$

$$\ddot{u}(t) = 0 \tag{4-21c}$$

Damped rigid body motion

A rigid body, assumed to undergo damped motion, as seen in figure 4-3d, is subjected to the following equation of motion

$$m\,\ddot{u}(t) + c\,\dot{u}(t) = \delta(t) \tag{4-22}$$

After applying the Dirac impulse the body is expected to start traveling at a velocity equal to as is in the undamped case. The velocity is then expected to decrease exponential as time passes.

The differential equation to be solved for the homogeneous solution then is

$$\ddot{u}(t) + \frac{c}{m}\,\dot{u}(t) = 0 \tag{4-23}$$

Combined with satisfying the impulse equation, the solution for the IRFs is:

$$u(t) = \frac{1}{c}\left(1 - e^{-\frac{c}{m}\,t}\right) \tag{4-24a}$$

$$\dot{u}(t) = \frac{1}{m}\,e^{-\frac{c}{m}\,t} \tag{4-24b}$$

$$\ddot{u}(t) = -\frac{c}{m^2}\,e^{-\frac{c}{m}\,t} \tag{4-24c}$$

The derivation for (4-24a) is a bit more lengthy than is depicted here. For the full derivation the reader is referred to appendix B. It can be seen that all solutions converge to (4-21) when $c \to 0$.[2]

4-2-3 IRFs for multiple DoF system using Modal Superposition

Considering a n-DoF system, often it is possible to obtain the IRFs of the system using Modal Super Position (MSP). This section briefly covers the concept of MSP and discusses how to obtain the IRFs of the system using MSP.

The n-DoF system, excited by a Dirac impulse on DoF j, is subjected to the following equation of motion:

$$\mathbf{M}\,\ddot{\mathbf{u}}(t) + \mathbf{C}\dot{\mathbf{u}}(t) + \mathbf{K}\,\mathbf{u}(t) = \boldsymbol{\delta}_j(t) \tag{4-25}$$

Here, $\boldsymbol{\delta}_j(t)$ indicates a vector with a perfect Dirac impulse on DoF j and zeros for the other DoFs.

The idea behind MSP is that the systems response can be built by a sum of deformation shapes (or mode shaped) $\mathbf{x}_r$ and the amplitudes of these shapes (modal amplitudes) η_r.

$$\mathbf{u}(t) = \sum^{r} \mathbf{x}_r\,\eta_r(t) \tag{4-26}$$

These eigenmodes are the eigenvectors of the eigenvalue problem of the system of equations that follows from the differential equation for the homogeneous solution of the conservative system:

$$\left(\mathbf{M} - \omega_n^2\,\mathbf{K}\right) = \mathbf{0} \tag{4-27}$$

---

[2] Note that the limit $c \to 0$ for (4-24a) is solved using a standard limit in calculus.

The eigenvalues ω_n pertaining to these eigenvectors are the eigenfrequencies pertaining to the eigenmodes. If the modes are fully uncoupled, which is the case when the system is proportionally damped.[3] it is possible to obtain the IRFs using Modal Super Position. Analogue to the single DoF system, the result of the Dirac impulse on the modes can be obtained.

The modal equations are set up using modal parameters, existing for every mode r:

$$\mu_r \triangleq \mathbf{x}_r^T \, \mathbf{M} \, \mathbf{x}_r \tag{4-28a}$$

$$\beta_r \triangleq \mathbf{x}_r^T \, \mathbf{C} \, \mathbf{x}_r \tag{4-28b}$$

$$\gamma_r \triangleq \mathbf{x}_r^T \, \mathbf{K} \, \mathbf{x}_r \tag{4-28c}$$

The decoupled normal equation for modes then yields:

$$\mu_r \, \ddot{\eta}_r(t) + \beta_r \, \dot{\eta}_r(t) + \gamma_r \, \eta(t) = \mathbf{x}_r^T \, \boldsymbol{\delta}_j(t) \tag{4-29}$$

Analogue to (4-11) the impulse equation for the mode is satisfied by

$$\dot{\eta}_r(0) = \int_0^{t+} \frac{\mathbf{x}_r^T \boldsymbol{\delta}_j(t)}{\mu_r} \, \mathrm{dt} = \frac{\mathbf{x}_r^T \mathbf{1}_j}{\mu_r} \tag{4-30}$$

Here $\mathbf{1}_j$ denotes a vector with value 1 on DoF j and 0 for the other DoFs. Scalar quantity $\dot{\eta}_r(0)$ can be interpreted as the modal velocity at time $t = 0$. Typically $\mathbf{x}_r^T \boldsymbol{\delta}_j(t)$ can be denoted as $\phi_{r,j}$ indicating the modal participation factor of load r, for an impulse on node j. In a similar manner $\mathbf{x}_r^T \mathbf{1}_j$ represents the modal participation factor in terms of impulse, which can be defined as

$$\Phi_{r,j} \triangleq \mathbf{x}_r^T \mathbf{1}_j \tag{4-31}$$

Which is used in the derivation below.

Analogue tot the single DoF system, some frequency- and damping parameters can be defined:

$$\omega_{n,r} \triangleq \sqrt{\frac{\gamma_r}{\mu_r}} \tag{4-32a}$$

$$\zeta_r \triangleq \frac{\beta_r}{2\sqrt{\mu_r \, \gamma_r}} = \frac{\beta_r}{2 \, \mu_r \, \omega_{n,r}} \tag{4-32b}$$

$$\omega_{d,r} \triangleq \omega_{n,r} \sqrt{1 - \zeta_r^2} = \sqrt{\omega_{n,r}^2 - \zeta_r^2 \, \omega_{n,r}^2} \tag{4-32c}$$

$$\theta_r \triangleq \tan^{-1} \frac{\zeta_r \, \omega_{n,r}}{\omega_{d,r}} \tag{4-32d}$$

Solving for $\eta_r(t)$, analogue to the single DoF system, yields

$$\eta_r(t) = \hat{\dot{\eta}}_r \, \frac{\sin\left(\omega_{d,r} \, t\right)}{\omega_{n,r}} \, e^{-\zeta_r \, \omega_{n,r} \, t} \tag{4-33}$$

---

[3] The eigenmodes of a system are mass- and stiffness-orthogonal. With the system being proportionally damped, the eigenmodes are also damping-orthogonal, i.e. $\beta_{rs} = \mathbf{x}_r^T \, \mathbf{C} \, \mathbf{x}_s = 0$ for $r \neq s$. This results in fully uncoupled modal equations.

Using substitution in the impulse equation(4-30), $\hat{\dot{\eta}}_r$ can be obtained such that the impulse equation is satisfied:

$$\hat{\dot{\eta}}_r = \frac{\Phi_{r,j}}{\mu_r \, \cos\theta_r} = \frac{\omega_{n,r}\,\Phi_{r,j}}{\omega_{d,r}\,\mu_r} \tag{4-34}$$

Substitution and derivation yields, analogue to (4-19), the solution to $\eta_r(t)$ and its derivatives:

$$\boxed{\begin{aligned}
\eta_r(t) &= \frac{\Phi_{r,j}}{\omega_{d,r}\,\mu_r}\,\sin\left(\omega_{d,r}\,t\right) e^{-\zeta_r\,\omega_{n,r}\,t} && \text{(4-35a)}\\
\dot{\eta}_r(t) &= \frac{\omega_{n,r}\,\Phi_{r,j}}{\omega_{d,r}\,\mu_r}\,\cos\left(\omega_{d,r}\,t+\theta\right) e^{-\zeta_r\,\omega_{n,r}\,t} && \text{(4-35b)}\\
\ddot{\eta}_r(t) &= -\frac{\omega_{n,r}^2\,\Phi_{r,j}}{\omega_{d,r}\,\mu_r}\,\sin\left(\omega_{d,r}\,t+2\,\theta\right) e^{-\zeta_r\,\omega_{n,r}\,t} && \text{(4-35c)}
\end{aligned}}$$

When the modal amplitudes $\eta_r(t)$ are known, the solution for the IRFs is obtained by modal superposition:

$$\mathbf{u}(t) = \sum^{r} \mathbf{x}_r\,\eta_r(t) \tag{4-36}$$

If existent, rigid body modes can also be taken into account in the modal superposition analogue to (4-21) or (4-24). Repeating the above process for Dirac impulses on every DoF j in the system allows to set up matrix $\mathbf{H}(t)$ containing the IRFs of the entire system.

4-3 Measuring IRFs

Keeping in mind the research goals, experimentally obtaining IRFs definitely requires to be covered in this chapter. The goal is to perform substructuring with experimentally obtained IRFs but literature has shown that this is not as straight forward as it seems.[8,12]

Let us first discuss the rather obvious subject involved in obtaining IRFs experimentally:

- **Nyquist frequency.** The Nyquist frequency equals half the sample frequency and describes the highest frequency content that can be given by the discrete signal without aliasing.[4] The sample frequency should be chosen such that the frequency band one is interested in is lower than the Nyquist frequency.
- **Measurement noise.** Almost inevitably, every measurement setup has to cope with measurement noise. On thing towards obtaining measurements with an acceptable signal-to-noise ratio is to pick measurement equipment in the correct range.
- **Measurement errors.** Besides measurement noise, the measurement will also be subjected to errors induced otherwise. An example one could think of is placing measurement equipment or exciting a structure 'in the proximity' of the location it should be measuring or be excited at. One can imagine exciting a structure in-plane on a flat surface offers quite the challenge.

---

[4] With aliasing a frequency higher than the Nyquist frequency is identified as the frequency the same amount lower as the Nyquist frequency.

Besides the above subjects which apply to measurements in general, some additional subjects that apply directly to IRF measurement should be taken into account.

4-3-1 IRFs by Imperfect Impulse

When applying an impact measurement, the structure's dynamics can be described using the convlution product as was seen in (3-5), which can be rewritten for this purpose to

$$\tilde{h}(t) = \int_0^t h(t-\tau)\,\tilde{\delta}(\tau)\,\mathrm{d}\tau \tag{4-37}$$

In this equation $h(t)$ represents the 'true' IRF of the structure, $\tilde{\delta}(t)$ represents the given impact and $\tilde{h}(t)$ represents the measured signal. If the excitation would be a perfect Dirac, the measured IRF would show the true IRF. Unfortunately, this is in practice never the case.

In [8] it is discussed that the actual impacts show resemblance with a single period of a cosine function, i.e.

$$\tilde{\delta}(t) = \frac{1}{T_{imp}}\left(1-\cos\left(2\pi\frac{t}{T_{imp}}\right)\right) \quad \text{for} \quad 0 \le t \le T_{imp} \tag{4-38}$$

which ensures a unit Impulse is given. Using the measured IRF $\tilde{h}(t)$ yields different responses $u(t)$ than would be obtained using the true IRF $h(t)$, which is discussed below.

For the purpose of illustration, the bar example from section 3-3-1 is used.[5] The impact time is assumed to have been $T_{imp} = 0.9\,[ms]$. Figure 4-6a shows the applied impulse. The effect is visible in figure 4-6b, which compares the 'true' IRF to the obtained IRF.

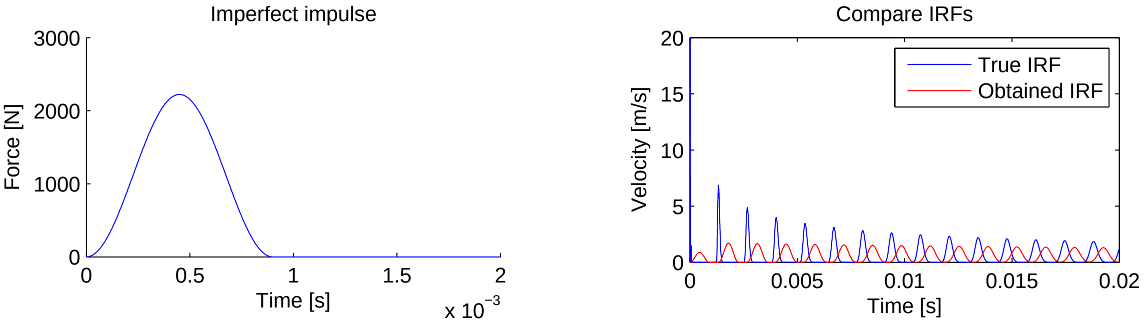

(a) Imperfect impulse according to (4-38), using $T_{imp} = 0.9\,[ms]$.

(b) Comparison of the 'true' IRF and the obtained IRF. Note that the graph has been cropped on the velocity axis and does not completely show the first peak of $101\,[m/s]$ for the true IRF.

Figure 4-6

Figure 4-6b shows three fundamental differences in the obtained IRF compared to the 'true' IRF:

---

[5] A bar of length $l = 1.026\,[m]$ numerically modelled using 50 elements of equal length. Young's modulus $E = 3.1\,[GPa]$, density $\rho = 1330\,[kg/m^3]$ and diameter $D = 0.04\,[m]$.

- The true IRF shows sharp high peaks while the obtained IRF shows broader flattened peaks. The sharp peaks are due to the fact the true IRF initially also has energy stored in the higher frequent modes, which damps out rather fast, see figure 4-7b. The imperfect impulse is not able to store energy in the higher frequent modes and thus ends up with only energy stored in the lower frequent modes which damps out slower, as shown in figure 4-7b.

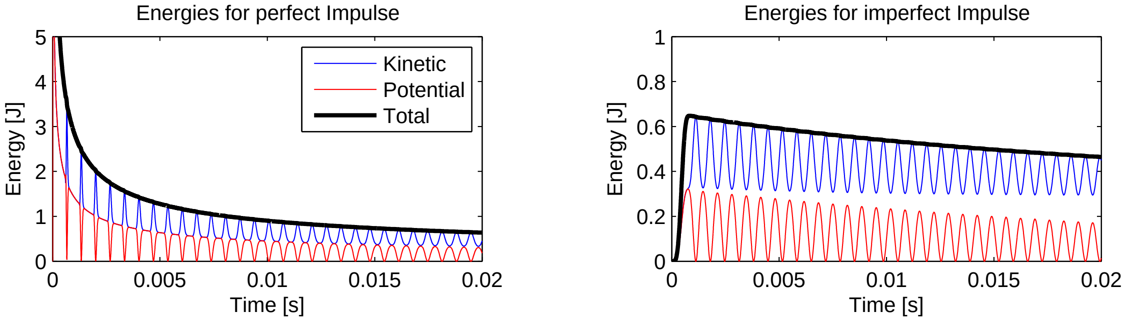

(a) Energies for the perfect impulse. Note that the graph has been cropped on the energy axis and does not completely show the first peak of $50\,[J]$ for the total energy.

(b) Energies for the imperfect impulse.

Figure 4-7: Amount of energy in the system for excitation by perfect and imperfect impulse. Note the difference in scaling on the energy axis.

- The applied impact peaks at $t = 0.45\,[ms]$ rather than $t = 0\,[ms]$, which has induced the delay depicted in the graph.

- Another interesting effect is that the amplitude of the first peak of the obtained IRF at $0.45\,[ms]$ is approximately half the size of the second peak at $18\,[ms]$, $0.89\,[m/s]$ compared to $1.70\,[m/s]$. This effect was also encountered in a recent study,[12] which induced difficulties using the IRFs for the purpose of substructuring. This effect seems very counter intuitive, but is explained after the discussion on the various excitations below.

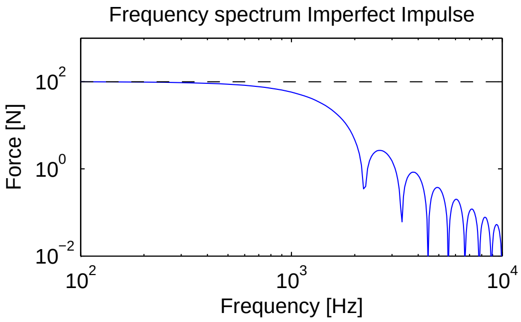

Figure 4-8: Frequency spectrum of applied impulse.

In order to examine the effects of using the imperfect IRF, the bar is subjected to four different periodic excitations, as seen in figure 4-9. Figure 4-9b shows the result of an excitation of low frequency in comparison with the systems dynamics[6]. The only visible effect is the delay equal to the delay in the IRF. In the response for a 250 $[Hz]$ excitation, the response obtained with the true IRF starts to show some of the first system dynamics (769 $[Hz]$). However in the response obtained by using the imperfect IRF, these system dynamics don't show that explicit. This can be explained by the bandwidth of the excitation which lays roughly around 800 to 900 $[Hz]$, as seen in figure 4-8. This is also illustrated in figure 4-9c, where it is shown that the amplitude (and phase) of the response is clearly affected when exciting with this frequency. Finally, exciting above this bandwith frequency shows that the results are no longer reliable, as shown in figure 4-9d.

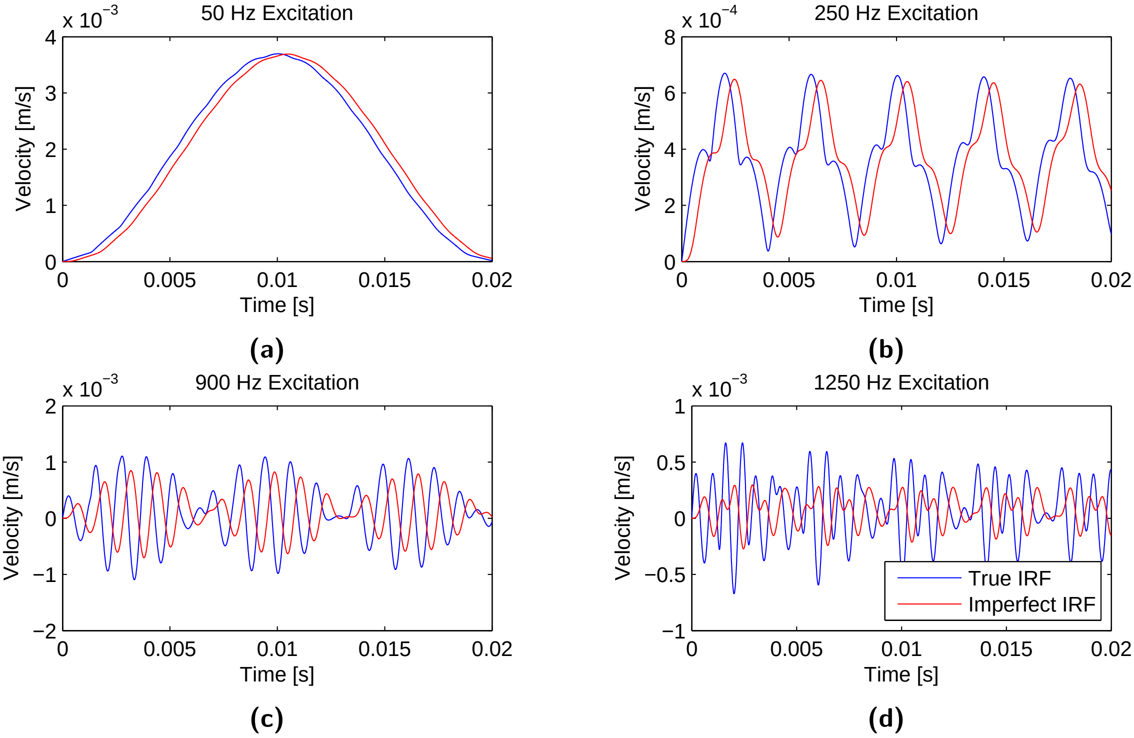

(a) **(b)** **(c)** **(d)**

Figure 4-9: Comparison of the system using the true IRF and the imperfect IRF subjected to four different periodic excitations.

---

[6] The first eigenmode has an eigenfrequency of 769 $[Hz]$.

The first driving point IRF peak explained

Consider for the purpose of illustration an velocity IRF $\dot{h}(t) = \frac{1}{2} + \frac{1}{2}\cos\left(2\pi\frac{1}{T}\right)$, which would typically pertain to a mass-spring-mass system, since it contains one rigid body mode and one vibration mode. For $T = 1\,[ms]$ the IRF is given in figure 4-10a. Now an impulse according to (4-38) using $T_{imp} = T = 1\,[ms]$ is used, as seen in figure 4-10b.

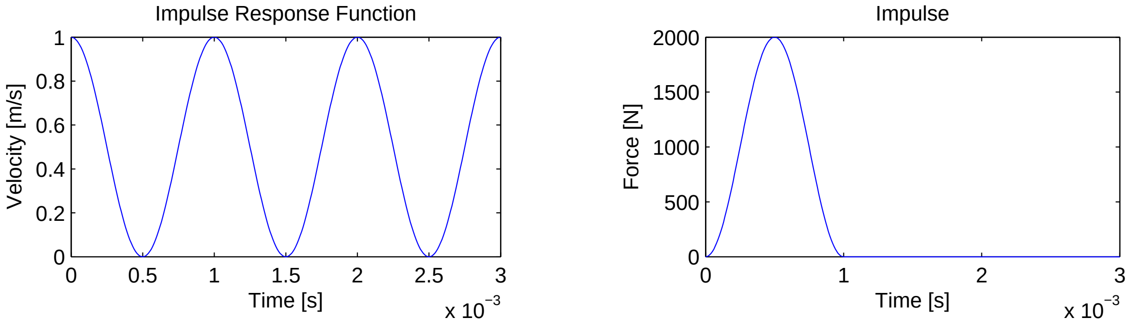

(a) Sample IRF with $T = 1\,[ms]$.

(b) Sample impulse using $T_{imp} = 1\,[ms]$

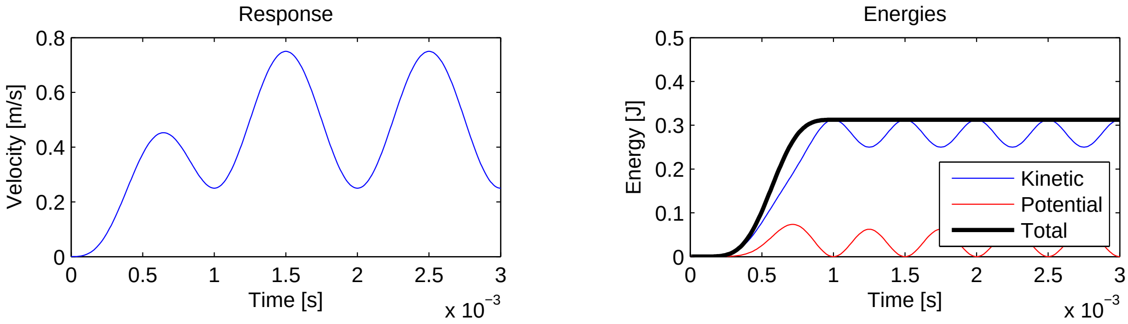

(c) Obtained velocity by convolving the impulse and IRF.

(d) Amount of energy in the system.

Figure 4-10

Now one can imagine that the convolution product gives the highest response when the peak of the impulse is aligned with the peak in the IRF *and* all the energy is put into the system. The first time this situation occurs is at $t = 1.5\,[ms]$. This is also shown in figure 4-10c. So what happens at $t = 0.67\,[ms]$? The part of the impulse that has already been applied aligns reasonably with the first IRF peak, although not all energy is put in the system yet, as seen in figure 4-10d.

Now we can distinguish three extremes:

- The situation illustrated above where T and T_{imp} have the same order of magnitude, i.e. $T_{imp} \sim T$. In this case the first shown peak shows a decreased amplitude as discussed above.

- The situation where T_{imp} approximates a Dirac function, i.e. $T_{imp} \ll T$. In this case the above effect does not occur.

- The situation where the high frequent dynamics of the system are not excited, i.e. $T_{imp} \gg T$. In this case the high frequency content of the system does not show in the response.

Back to the IRF shown in figure 4-6b. Consider the perspective of the IRF buildt by MSP.[7] The low frequent modes dominate the combined amplitudes on the DoFs. Now in this particular case, the frequency of the first vibrational eigenmode of the system has a period almost equal to the excitation period, $1.3\,[ms]$, compared to $0.9\,[ms]$. Therefore the effect of the decreased amplitude as discussed above appears, on the mode most dominant for the combined amplitude. Hence, the decreased amplitude for the first peak in the obtained IRF.

4-3-2 Rotational DoFs

In order to obtain a complete 6-DoF description for the motion and loads[8] for certain points on the structure, the Virtual Point Transformation can be used. The method is shortly summarised in this section. For more details background on the method, the reader is referred to.[3,13,15]

A key benefit of the method is that the resulting generalised motion and loads are collocated in a single point, the so-called *virtual point.* As such compatibility is automatically ensured with FE models[9]. Additionally the method suppresses uncorrelated measurement noise due to the least-square nature of the transformation.

Let us consider an interface point surrounded by N translational DoFs $\mathbf{u}$. This set of measured DoFs can be reduced to M generalised DoFs $\mathbf{q}$ by means of a mapping matrix $\mathbf{R}_u$. Since the number of generalised DoFs is smaller than the amount of measured DoFs ($M < N$), a vector of residual displacements $\boldsymbol{\mu}$ is added:

$$\mathbf{u} = \mathbf{R}_u \mathbf{q} + \boldsymbol{\mu} \tag{4-39}$$

When one chooses $\mathbf{q}$ to describe three translations and three rotations for each virtual point, the columns of $\mathbf{R}_u$ represent the so-called rigid Interface Displacement Modes (IDMs). It can be shown that $\mathbf{q}$ can be written as a function of $\mathbf{u}$ by making a least-squares projection:

$$\mathbf{q} = \mathbf{T}_u \mathbf{u} \qquad \text{with} \qquad \mathbf{T}_u \triangleq (\mathbf{R}_u^T \mathbf{R}_u)^{-1} \mathbf{R}_u^T \tag{4-40a}$$

To determine virtual point loads, the same technique applies. By choosing $\mathbf{R}_f$ for mapping applied forces $\mathbf{f}$ to virtual point loads $\mathbf{p}$, one can write:

$$\mathbf{f} = \mathbf{T}_f^T \mathbf{p} \qquad \text{with} \qquad \mathbf{T}_f \triangleq (\mathbf{R}_f^T \mathbf{R}_f)^{-1} \mathbf{R}_f^T \tag{4-40b}$$

---

[7] Recall section 4-2.

[8] The terms motion and loads are used when referred to the 6-DoF set of respectively displacements/rotations and forces/moments.

[9] This only applies to FE models containing 6-DoF nodes. A major part of the finite elements consist of 3-DoF nodes.

Using the above expressions the IRFs of measured excitations to displacements can be rewritten to the virtual point description by substitution of (4-40a) and (4-40b) into $\mathbf{u}(t) = \int_0^t \mathbf{H}(t-\tau)\,\mathbf{f}(\tau)\,\mathrm{d}\tau$:

$$\mathbf{q}(t) = \int_0^t \mathbf{T}_u\,\mathbf{H}(t-\tau)\,\mathbf{T}_f^T\,\mathbf{p}(\tau)\,\mathrm{d}\tau = \int_0^t \mathbf{H}^{\mathrm{vp}}(t-\tau)\,\mathbf{p}(\tau)\,\mathrm{d}\tau \tag{4-41}$$

where $\mathbf{H}^{\mathrm{vp}} \triangleq \mathbf{T}_u\mathbf{H}\mathbf{T}_f^T$ denotes the collocated virtual point receptance. It is seen here that the virtual point transformation is not time dependant, but is purely a spacial transformation. Now $\mathbf{H}^{\mathrm{vp}}$ can be used for substructuring with other components, either derived from experimental or from numerical models, provided that the description of the virtual points is chosen such that it corresponds to the 6 degrees of freedom of a node.

4-4 Discussion

Concluding this chapter, two topics require some additional discussion. The discussion on what physical quantities to use for convolution is discussed first. Next the choice for methodology on obtaining IRFs is discussed.

4-4-1 Displacement, velocity or acceleration IRF?

Now that the IRFs for displacements, velocities and accelerations are known, one can argue whether they can actually be used in the intended context; the convolution product. First recall equation (4-11):

$$m\,\Delta\dot{u} = \int_0^{t+} \delta(t)\,\mathrm{dt} = 1$$

It is obvious that applying a Dirac impulse leads to a discontinuity (jump) for the velocity function. Therefore the expression for the velocity $\dot{u}(t)$ is expected to start from fictive time t_+; which is in theory at time $t = 0$, after the impulse has been applied. Fortunately, when integrating over this discontinuity yields a continuous function, i.e. the velocity IRF can be used in the convolution integral. Besides that, this means that the displacement IRF is continuous from $t = 0$ and can consequently be used as well.

For the accelerations, this is a different story. Due to change in velocity at time $t = 0$, its derivative, acceleration does not exist at $t = 0$.[10] This means that information is lacking from the acceleration IRF, since it has to start at time t_+ as well. This lack of information makes it impossible to use 'true' acceleration IRF within the convolution integral, i.e. the acceleration IRF is not qualified for the purpose of convolving to an acceleration response.

Do note that it is possible to use time-discretised acceleration IRFs that approximate the 'true' acceleration IRFs, e.g. measured IRFs or IRFs obtained by Newmark time integration using initial applied force conditions. These IRFs do describe the required acceleration to obtain the jump in velocity, which is the requirement to use them.

---

[10] Although one could argue that the acceleration should equal ∞ at time $t = 0$, which is consistent with the behaviour of the Dirac impulse.

4-4-2 Standing waves vs. travelling waves

One can argue what method is preferred to obtain IRFs from a numerical model. It was shown that the Newmark time integration algorithms are able to give an accurate approximation using the initial velocity conditions when the Courant's number is chosen relatively small. Obtaining IRFs using the analytical approach combined with MSP appears to be exact for a numerical model regardless of the choice of Courant's number. So when it comes to accuracy, the analytical approach is preferred.

The downside of the MSP method is that it describes a travelling wave as a superposition of standing waves, which intuitively does not seem to be very efficient. The method shows poor spacial convergence, i.e. one would need a significant amount of modes to obtain a 'smooth' travelling wave. From another perspective one could try to obtain IRFs using wave equations. Those equations, as for instance described in [6], are designed to describe travelling waves, rather than standing waves which could prove to be a more efficient method to obatain IRFs. This is however, beyond the scope of this thesis.

Chapter 5

Enhancing computational performance

In the process of obtaining structural responses by convolution, another challenge arises as convolution time proceeds. Considering a discretised convolution integral, for every Δt time proceeds an additional calculation step in the convolution is added. See for instance (3-14). The summations grow one step as time step n proceeds to a next step. This means that the total computational effort grows quadratically as the total time to compute increases linearly. Now considering the goal of real-time solutions, this might mean that after a certain amount of time, the time required to calculate the new system's state exceeds the amount of time available (Δt). This would mean that real-time solutions are limited to a certain amount of convolution time.

In order to overcome these limitations, research has been done on truncating the IRF after it has been sufficiently damped out.[10] This technique is discussed in section 5-1. In [10] it is also discussed that Rigid Body Motion needs to be filtered out, since it does not show converging behaviour in displacement and velocity IRFs. This idea got extended in [14]. This work discusses the fact that the low frequent content of the IRF damps out relatively slowly compared to the high frequent content. Therefore it is proposed to use a time integration algorithm on the rigid body modes and low frequent modes and use the convolution integral on the remaining high frequency content. This technique is discussed in section 5-2. Finally 5-3 proposes a recursive algorithm, other than the Newmark time integration method to efficiently solve the contribution of the rigid body and low frequent modes.

5-1 Truncating the IRF

The idea of truncating the IRF can be explained by splitting the convolution product in two parts:

$$u(t) = \int_0^t h(t-\tau)\, f(\tau)\, \mathrm{d}\tau = \int_0^{t-t_c} h(t-\tau)\, f(\tau)\, \mathrm{d}\tau + \int_{t-t_c}^{t} h(t-\tau)\, f(\tau)\, \mathrm{d}\tau \tag{5-1}$$

Now the truncation is based on the assumption that after time t_c the IRF has decayed so it can assumed to be zero, i.e.

$$h(t-\tau) \simeq 0 \qquad \text{for} \qquad \tau < t - t_c$$

Obviously this is only the case for converging IRFs. Displacement IRFs including rigid body modes would obviously not qualify. So assuming the IRF converges to zero, the convolution product can be rewritten to

$$u(t) \simeq \int_{\max(0, t-t_c)}^{t} h(t-\tau)\, f(\tau)\, \mathrm{d}\tau \tag{5-2}$$

This approximation can significantly reduce the computational cost of the integral. It corresponds to cutting off (truncating) the IRF at time t_c. From another perspective this can also be seen as windowing the IRF using a rectangular window with width t_c. Formally such a windows can be written as

$$W_{rect}(t) = \begin{cases} 1 & \text{if } t < t_c \\ 0 & \text{if } t > t_c \end{cases} \tag{5-3}$$

This effect of this window is illustrated in figure 5-1a. The work [10] discusses that, when using truncated IRFs for coupling, it is desirable to use a smoother window in order to improve accuracy and stability of the coupled response. Therefore a cosine shaped window was proposed and evaluated, defined as

$$W_{cos}(t) = \begin{cases} \cos\left(\frac{\pi t}{2 t_c}\right) & \text{if } t < t_c \\ 0 & \text{if } t > t_c \end{cases} \tag{5-4}$$

The effect of this window is illustrated in figure 5-1b.

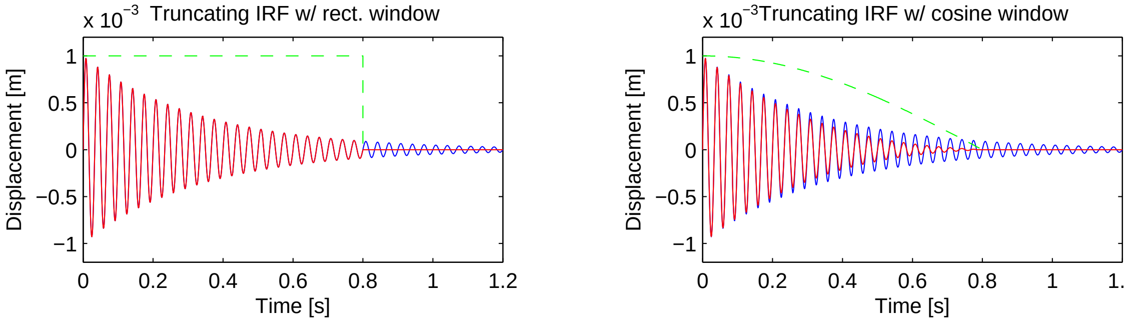

(a) Truncating using the rectangular window.

(b) Truncation using the cosine window.

Figure 5-1: Truncating using two different windows. The blue graph shows the original IRF. The red graph shows the truncated IRF. The green dashed line indicates the shape of the window.

To obtain a value for t_c a threshold for the amplitude can be used. The IRF can be truncating as soon as it remains under this threshold. [10] demonstrates values ranging from 10^{-1} to 10^{-3} the maximum amplitude, with accurate results depending on the chosen window.

Remarks

The proposed cosine shaped window has a first order discontinuity at t_c compared to the zeroth order discontinuity of the rectangular window. A first order discontinuity though can not be interpreted as something physical on a displacement level, while a second order discontinuity can. Another physically interpretable decay that can be though of is exponential decay. Chapter 9 will show that exponential decay is also required for successful coupling.

Another remark is that truncation does not work for non converging IRFs. However, this limitation can be overcome by separating the non-converging and/or slowly converging content from the rest, as is discussed next.

5-2 Structural responses using MSP

Recall section 4-2 where it is discussed that IRFs can also be obtained using Modal Superposition (MSP). This section using the principle of MSP to obtain the structural responses of a system subjected to an excitation. Consider the following equation of motion:

$$\mathbf{M}\,\ddot{\mathbf{u}}(t) + \mathbf{C}\dot{\mathbf{u}}(t) + \mathbf{K}\,\mathbf{u}(t) = \mathbf{f}(t) \tag{5-5}$$

The system is assumed to be proportionally damped, such that it can be characterised by its eigenmodes. Now the modal space is split up in three parts:

$$\mathbf{x}_r \in \begin{cases} \mathbf{X}^{\mathrm{RB}} & \text{for} \quad \omega_r = 0 \\ \mathbf{X}^{\mathrm{LF}} & \text{for} \quad 0 < \omega_r < \omega_c \\ \mathbf{V} & \text{for} \quad \omega_c \leq \omega_r \end{cases} \tag{5-6}$$

Here ω_c acts as a threshold frequency determining whether the mode pertains to the low frequent or high frequent content. In practice, when using experimentally obtained IRFs for example, ω_c can be the frequency from where modal fit is no longer possible. That would mean that all identified modes end up in $\mathbf{X}^{\mathrm{LF}}$, while the higher frequent unidentified modes would pertain to $\mathbf{V}$. Using this split in modal content, the solution for $\mathbf{u}(t)$ can be expressed in an analogue way:

$$\mathbf{u}(t) = \mathbf{X}^{\mathrm{RB}}\,\boldsymbol{\eta}^{\mathrm{RB}}(t) + \mathbf{X}^{\mathrm{LF}}\,\boldsymbol{\eta}^{\mathrm{LF}}(t) + \mathbf{r}(t) \tag{5-7}$$

Vectors $\boldsymbol{\eta}^{\mathrm{RB}}(t)$ and $\boldsymbol{\eta}^{\mathrm{LF}}(t)$ respectively denote the modal amplitudes of the rigid body modes and the low frequent modes. Vector $\mathbf{r}$ is a solution for all the high-frequency content and mathematically speaking does not exist in subspaces $\mathbf{X}^{\mathrm{RB}}$ and $\mathbf{X}^{\mathrm{LF}}$. Therefore vector $\mathbf{r}$ does exist in subspace $\mathbf{V}$ which is on its turn orthogonal to the other two subspaces. Combined $[\mathbf{X}^{\mathrm{RB}}\ \mathbf{X}^{\mathrm{LF}}\ \mathbf{V}]$ yields the $\mathbf{M}$- and $\mathbf{K}$-orthogonal modal space that spans the entire space for the solution of $\mathbf{u}$.[14]

It is proposed in [14] to solve the rigid body- and low frequent content using the equations of motions, projecting them on the associated subspace and solve using a Newmark time integration algorithm. This work proposes an alternative method, which is discussed in the next section.

So for now we focus on the high frequency content, to which the solution is found differently. Although $\mathbf{r}(t)$ exist in subspace $\mathbf{V}$, it is desired to avoid specifying this space, as it contains all additional information on the system not described by $\mathbf{X}^{\mathrm{RB}}$ and $\mathbf{X}^{\mathrm{LF}}$, which we don't want to compute. It is proposed to define operator $\mathbf{P}$ that projects the solution $\mathbf{M}$-orthogonal to subspace $[\mathbf{X}^{\mathrm{RB}}\ \mathbf{X}^{\mathrm{LF}}]$.[1]

$$\mathbf{P} = \mathbf{I} - \mathbf{X}^{\mathrm{RB}} \left(\mathbf{X}^{\mathrm{RB}}\right)^T \mathbf{M} - \mathbf{X}^{\mathrm{LF}} \left(\mathbf{X}^{\mathrm{LF}}\right)^T \mathbf{M} \tag{5-8}$$

This allows us to solve for $\mathbf{r}(t)$ using the original systems IRFs $\mathbf{H}(t)$. Explicitly, the original IRF is filtered by pre-multiplication with matrix $\mathbf{P}$, filtering out all rigid body and low frequent content.[2] Implicitly this resembles a projection on subspace $\mathbf{V}$, where high frequency residual $\mathbf{r}(t)$ lives.

$$\mathbf{r}(t) = \int_0^t \left(\mathbf{P}\,\mathbf{H}(t-\tau)\right)\,\mathbf{f}(\tau)\,\mathrm{d}\tau = \int_0^t \mathbf{H}^{\mathrm{HF}}(t-\tau)\,\mathbf{f}(\tau)\,\mathrm{d}\tau \tag{5-9}$$

The obtained $\mathbf{H}^{\mathrm{HF}}$ now only contains the high frequency content above ω_c which is expected to decay rapidly. Applying a truncation technique as discussed in section 5-1 would thus allow a relatively short truncation time t_c, reducing computational cost significantly. A proof of concept was shown in [14].

5-3 Matrix recurrence procedure for modal contributions

Now that the high frequency content is taken care of, the rigid body $\boldsymbol{\eta}^{\mathrm{RB}}(t)$ and low frequency content $\boldsymbol{\eta}^{\mathrm{LF}}(t)$ still need to be calculated. This section derives an alternative to the Newmark time integration schemes. The full detailed derivations are found in appendix C.

Since this derivation concerns modal amplitudes, excitation $\mathbf{f}(t)$ also requires projection on the concerned mode. This is done using modal participation factors, defined as

$$\phi_r(t) \triangleq \mathbf{x}_r^T\,\mathbf{f}(t) \tag{5-10}$$

Where $\mathbf{x}$ now denotes the concerning mass-normalised mode. This derivation uses the assumption that the force loading is piecewise linear, such that the modal participation factor can be written as:

$$\phi_r(\tau) \simeq \phi_r(t_n)\frac{t_{n+1}-\tau}{\Delta t} + \phi_r(t_{n+1})\frac{\tau - t_n}{\Delta t} \tag{5-11}$$

When this is actually the case, the derivation is exact, otherwise it remains an approximation.[3]

In general, deriving the matrix recurrence procedure for modal contributions can be divided into four steps:

---

[1] Note that the modes are normalised to unity modal mass.

[2] Matrix $\mathbf{P}$ has a rank deficiency determined by the amount of modes in $[\mathbf{X}^{\mathrm{RB}}\ \mathbf{X}^{\mathrm{LF}}]$.

[3] Note that the Newmark time integration scheme also has this possibility, or less accurate ones.

1. Derive an expression for the modal amplitude from the modal Equation of Motion.
2. Assume piecewise linear excitation (5-11) and solve the convolution integral in the obtained expression.
3. Derive an expression for the modal velocity by taking the derivate of the of the expression for modal amplitude with respect to time.
4. Substitute the expressions for modal amplitude and velocity in the recursive algorithm.

The recursive algorithm will eventually contain the *IRF of a structure's mode*, denoted with $h(t)$, its first and second derivative in time, for which respectively the notation $h^{(1)}(t)$ and $h^{(2)}(t)$ is adopted and finally the first and second primitive function of the IRF. For the first and second primitive function of the IRF the respective notations $h^{(-1)}(t)$ and $h^{(-2)}(t)$ will be used in this chapter.

First the methodology will be extensively demonstrated for the case of vibration modes in section 5-3-1. Afterwards the methodology will be briefly extended to two types of Rigid Body Modes in section 5-3-2. During these derivations all superscripts RB and LF and subscript r are omitted for the purpose of clarity. Besides that all modes are assumed to be mass-normalised. Note that these derivations are a generalisation of the matrix recurrence algorithm for undamped vibrational modes proposed in [6].

5-3-1 Vibration Mode

The derivation of the recursive algorithm starts with the modal equation of motion:

$$\ddot{\eta}(t) + 2\,\zeta\,\omega_n\,\dot{\eta}(t) + \omega_n^2\eta(t) = \phi(t) \tag{5-12}$$

Solving the differential equation trough the Laplace domain in a manner analogue to the manner used in section 4-2 yields:

$$\eta(t) = \eta(0)\,h^{(1)}(t) + (\dot{\eta}(0) + 2\,\zeta\,\omega_n\eta(0))\,h(t) + \int_0^t \phi(\tau)\,h(t-\tau)\,\mathrm{d}\tau \tag{5-13}$$

The IRF $h(t)$ denotes the IRF for the mode as if the *mode* is excited with a perfect Dirac impulse.[4] Note the difference with the IRF for the mode for exciting a *node* with a perfect Dirac impulse as was done in section 4-2-3, which required projection on the mode using the $\frac{\mathbf{x}^T\mathbf{1}_j}{\mu}$ term.[5] The following IRF corresponds to the vibration mode:

$$h(t) = \frac{\sin(\omega_d t)}{\omega_d}\,e^{-\zeta\omega_n t} \tag{5-14a}$$

Recall from chapter 4 the definition of the various parameters, equation (4-32). The derivation will eventually comprise the derivative functions of $h(t)$ and even its primitive functions.

---

[4] This can be interpreted as modal loading also known from appropriate testing from aircraft wings.

[5] The term *node* in this sentence refers to a single DoF pertaining to a location on the structure.

Therefore its associated derivative and primitive functions are given:

$$h^{(1)}(t) = \frac{\omega_n}{\omega_d}\,\cos(\omega_d t + \theta)\,e^{-\zeta\omega_n t} \tag{5-14b}$$

$$h^{(2)}(t) = -\frac{\omega_n^2}{\omega_d}\,\sin(\omega_d t + 2\theta)\,e^{-\zeta\omega_n t} \tag{5-14c}$$

$$h^{(-1)}(t) = -\frac{\cos(\omega_d t - \theta)}{\omega_d\omega_n}\,e^{-\zeta\omega_n t} \tag{5-14d}$$

$$h^{(-2)}(t) = -\frac{\sin(\omega_d t - 2\theta)}{\omega_d\omega_n^2}\,e^{-\zeta\omega_n t} \tag{5-14e}$$

Back to (5-13), the terms containing the initial conditions are still preserved, therefore this expression is valid for any initial situation. Now substituting interval $[0;t]$ with $[t_n;t_{n+1}]$ gives a recurrent expression, allowing to obtain state information at time t_{n+1} using only state information from the state at time t_n, rather than the full time history as would have been the case with convolving the IRF:

$$\begin{aligned}\eta_{n+1} &= \eta_n\,h^{(1)}(\Delta t) + \big(\dot{\eta}_{n+1} + 2\,\zeta\,\omega_n\eta_n\big)\,h(\Delta t)\\ &\quad + \int_{t_n}^{t_{n+1}} \phi(\tau)\,h(t_{n+1}-\tau)\,\mathrm{d}\tau\end{aligned} \tag{5-15}$$

Note that the substitution for $h(t)$ and $\dot{h}(t)$ returns $h(\Delta t)$ and $\dot{h}(\Delta t)$ because the function values to be evaluated remain the same regardless of where in time t_n is chosen. Now substituting the piecewise linear behaviour expression (5-11) for excitation $\phi(t)$, substituting the expressions for $h(t)$ and $h^{(1)}(t)$ using (5-14) and solving the convolution integral yields:

$$\begin{aligned}\eta_{n+1} = \eta_n\,&\frac{\omega_n}{\omega_d}\,\cos(\omega_d\Delta t + \theta)\,e^{-\zeta\omega_n\Delta t}\\ &+ \big(\dot{\eta}_n + 2\,\zeta\,\omega_n\eta_n\big)\,\frac{\sin(\omega_d\Delta t)}{\omega_d}\,e^{-\zeta\omega_n\Delta t}\\ &+ \frac{\phi_n}{\omega_d\omega_n}\left(-\cos(\omega_d\Delta t - \theta)\,e^{-\zeta\omega_n\Delta t} + \frac{\sin(\omega_d\Delta t - 2\theta)\,e^{-\zeta\omega_n\Delta t} + \sin(2\theta)}{\omega_n\Delta t}\right)\\ &+ \frac{\phi_{n+1}}{\omega_d\omega_n}\left(\cos(\theta) - \frac{\sin(\omega_d\Delta t - 2\theta)\,e^{-\zeta\omega_n\Delta t} + \sin(2\theta)}{\omega_n\Delta t}\right)\end{aligned} \tag{5-16}$$

The modal amplitude at time t_{n+1} requires, among other things, the modal velocity at time t_n. Therefore an expression for the modal velocity is required before the recursive algorithm can be used. The modal velocity is determined by taking the derivative of η_{n+1} with respect to t_{n+1}, which eventually yields the following expression.

$$\begin{aligned}\dot{\eta}_{n+1} = -\eta_n&\frac{\omega_n^2}{\omega_d}\sin(\omega_d\Delta t + 2\theta)\,e^{-\zeta\omega_n\Delta t}\\ &+ \big(\dot{\eta}_n + 2\,\zeta\,\omega_n\eta_n\big)\,\frac{\omega_n}{\omega_d}\,\cos(\omega_d\Delta t + \theta)\,e^{-\zeta\omega_n\Delta t}\\ &+ \frac{\phi_n}{\omega_d\omega_n}\left(\frac{\cos(\omega_d\Delta t - \theta)\,e^{-\zeta\omega_n\Delta t}}{\Delta t} + \omega_n\,\sin(\omega_d\Delta t)\,e^{-\zeta\omega_n\Delta t} - \frac{\cos(\theta)}{\Delta t}\right)\\ &+ \frac{\phi_{n+1}}{\omega_d\omega_n}\left(-\frac{\cos(\omega_d\Delta t - \theta)\,e^{-\zeta\omega_n\Delta t}}{\Delta t} + \frac{\cos(\theta)}{\Delta t}\right)\end{aligned} \tag{5-17}$$

With the expressions for the modal amplitude η_{n+1} and velocity $\dot{\eta}_{n+1}$, we have everything that is required for the recursive algorithm. For the purpose of compact notation and efficient programming, the algorithm can be set up as a matrix operation. First it is required to define constants:

$$c_1 \triangleq \frac{\cos\theta}{\omega_d \omega_n} \quad \text{and} \quad c_2 \triangleq \frac{\sin 2\theta}{\omega_d \omega_n^2} \tag{5-18}$$

Now recalling (5-14), the recursive scheme is given rewriting (5-16) and (5-17) to:[6]

$$\begin{aligned}\begin{bmatrix} \eta_{n+1} \\ \Delta t\, \dot{\eta}_{n+1} \end{bmatrix} &= \begin{bmatrix} h^{(1)}(\Delta t) + 2\zeta\omega_n\, h^{(0)}(\Delta t) & \frac{h^{(0)}(\Delta t)}{\Delta t} \\ \Delta t\, h^{(2)}(\Delta t) + 2\zeta\omega_n \Delta t\, h^{(1)}(\Delta t) & h^{(1)}(\Delta t) \end{bmatrix} \begin{bmatrix} \eta_n \\ \Delta t\, \dot{\eta}_n \end{bmatrix} \\ &+ \begin{bmatrix} h^{(-1)}(\Delta t) - \frac{h^{(-2)}(\Delta t)}{\Delta t} + \frac{c_2}{\Delta t} & c_1 + \frac{h^{(-2)}(\Delta t)}{\Delta t} - \frac{c_2}{\Delta t} \\ -h^{(-1)}(\Delta t) + \Delta t\, h^{(0)}(\Delta t) - c_1 & h^{(-1)}(\Delta t) + c_1 \end{bmatrix} \begin{bmatrix} \phi_n \\ \phi_{n+1} \end{bmatrix}\end{aligned} \tag{5-19}$$

Which gives one pre-computable for the homogeneous solution and one pre-computable matrix for the particular solution. Also note the resemblance with state space notation.[5]

This matrix operation can now be performed for every low frequent mode $\boldsymbol{\eta}^{\mathrm{LF}}(t)$ and be substituted in (5-7). The next section discusses the same procedure for the rigid body modes $\boldsymbol{\eta}^{\mathrm{RB}}(t)$.

5-3-2 Rigid Body Mode

A similar derivation can be done for the rigid body modes $\boldsymbol{\eta}^{\mathrm{RB}}(t)$. Unlike with the vibration mode the derivation for the undamped case is slightly different than for the undamped case. First the undamped RBM is briefly discussed. Next, the undamped case is discussed in a similar way as the vibration mode.

Undamped RBM

The derivation of the recursive algorithm, again, starts with the modal equation of motion. Since the system has no damping, no stiffness and the modal mass equals unity, the equation comes in the simple form of

$$\ddot{\eta}(t) = \phi(t) \tag{5-20}$$

Solving this equation trough the Laplace domain yields

$$\eta(t) = \eta(0) + \dot{\eta}(0)\, t + \int_0^t \phi(\tau)(t-\tau)\, \mathrm{d}\tau \tag{5-21}$$

Now substituting (5-11) for the piecewise linear force assumption, substituting the time interval $[0; t]$ with $[t_n; t_{n+1}]$ and solving the integral gives:

$$\eta_{n+1} = \eta_n + \dot{\eta}_n\, \Delta t + \phi_n \frac{\Delta t^2}{3} + \phi_{n+1} \frac{\Delta t^2}{6} \tag{5-22}$$

---

[6] It is chosen here to substitute $h(t)$ and its derivative and primitive functions back into the matrix expression for the purpose of compact notation.

Now that modal amplitude is known, the modal velocity is given by taking its derivative with respect to t_{n+1}:

$$\dot{\eta}_{n+1} = \dot{\eta}_n + \frac{\phi_n + \phi_{n+1}}{2}\Delta t \tag{5-23}$$

which is the result to be expected. Analogue to what was shown in the previous section, (5-22) and (5-23) can be rewritten to

$$\begin{bmatrix} \eta_{n+1} \\ \Delta t\,\dot{\eta}_{n+1} \end{bmatrix} = \begin{bmatrix} 1 & 1 \\ 0 & 1 \end{bmatrix} \begin{bmatrix} \eta_n \\ \Delta t\,\dot{\eta}_n \end{bmatrix} + \frac{\Delta t^2}{6} \begin{bmatrix} 2 & 1 \\ 3 & 3 \end{bmatrix} \begin{bmatrix} \phi_n \\ \phi_{n+1} \end{bmatrix} \tag{5-24}$$

which concludes the matrix recurrence procedure for undamped rigid body modes. Note the resemblance between the expression for η_{n+1} using the piecewise linear modal participation factor $\phi(t)$ and the expression for the product of piecewise linear functions for the discretised convolution product as was shown in section 3-2.

Damped RBM

The derivation of the recursive algorithm for the damped RBM, starts with its equation of motion:

$$\ddot{\eta}(t) + \alpha\,\dot{\eta}(t) = \phi(t) \tag{5-25}$$

Since the modal mass is assumed to equal unity, damping coefficient α denotes the modal damping.[7] Solving the differential equation trough the Laplace domain yields:

$$\eta(t) = \eta(0)\,\dot{h}(t) + \left(\dot{\eta}(0) + \alpha\,\eta(0)\right) h(t) + \int_0^t \phi(\tau)\,h(t-\tau)\,\mathrm{d}\tau \tag{5-26}$$

The IRF $h(t)$ again denotes the IRF for the mode as if the mode was excited with a perfect Dirac impulse. The following IRF pertains to the damped Rigid Body Mode:

$$h(t) = \frac{1 - e^{-\alpha t}}{\alpha} \tag{5-27a}$$

Similar as with the derivation for the vibration modes, the associated derivative and primitive functions are required. Those are given by:

$$h^{(1)}(t) = e^{-\alpha t} \tag{5-27b}$$

$$h^{(2)}(t) = -\alpha\,e^{-\alpha t} \tag{5-27c}$$

$$h^{(-1)}(t) = \frac{t}{\alpha} + \frac{e^{-\alpha t}}{\alpha^2} \tag{5-27d}$$

$$h^{(-2)}(t) = \frac{t^2}{2\alpha} - \frac{e^{-\alpha t}}{\alpha^3} \tag{5-27e}$$

Back to (5-26), again the equation allows converting to a recursive procedure by substituting interval $[0; t]$ with $[t_n; t_{n+1}]$.

$$\begin{aligned} \eta_{n+1} =& \eta_n\,\dot{h}(\Delta t) + \left(\dot{\eta}_{n+1} + \alpha\,\eta_n\right) h(\Delta t) \\ &+ \int_{t_n}^{t_{n+1}} \phi(\tau)\,h(t_{n+1}-\tau)\,\mathrm{d}\tau \end{aligned} \tag{5-28}$$

---

[7] In the case where the modal mass does not equal unity, i.e. $\mu \neq 1$, damping coefficient α denotes the modal damping divided by the modal mass, i.e. $\alpha = \frac{\beta}{\mu}$.

Next by substituting the expression for piecewise linear behaviour of the force (5-11), substituting expressions from (5-27) and solving the convolution integral, the following expression is obtained:

$$\begin{aligned}\eta_{n+1} =& \eta_n \, e^{-\alpha \, \Delta t} + \left(\dot{\eta}_{n+1} + \alpha \, \eta_n\right) \frac{1 - e^{-\alpha \, \Delta t}}{\alpha} \\ &+ \phi_n \left(\frac{\Delta t}{\alpha} + \frac{e^{-\alpha \, \Delta t}}{\alpha^2} - \frac{1}{\alpha^3 \, \Delta t} - \frac{\Delta t}{2 \, \alpha} + \frac{e^{-\alpha \, \Delta t}}{\alpha^3 \, \Delta t} \right) \\ &+ \phi_{n+1} \left(-\frac{1}{\alpha^2} + \frac{1}{\alpha^3 \, \Delta t} + \frac{\Delta t}{2 \, \alpha} - \frac{e^{-\alpha \, \Delta t}}{\alpha^3 \, \Delta t} \right)\end{aligned} \tag{5-29}$$

Similar as before, the modal velocity is required, which is obtained by taking the derivative of the modal amplitude η_{n+1} with respect to t_{n+1}. Eventually this yields this expression:

$$\begin{aligned}\dot{\eta}_{n+1} =& -\alpha \, \eta_n \, e^{-\alpha \, \Delta t} + \left(\dot{\eta}_{n+1} + \alpha \, \eta_n\right) e^{-\alpha \, \Delta t} \\ &+ \phi_n \left(\frac{1}{\alpha} - \frac{e^{-\alpha \, \Delta t}}{\alpha} - \frac{1}{\alpha} - \frac{e^{-\alpha \, \Delta t}}{\alpha^2 \, \Delta t} + \frac{1}{\alpha^2} \right) \\ &+ \phi_{n+1} \left(-\frac{1}{\alpha^2 \, \Delta t} + \frac{1}{\alpha} + \frac{e^{-\alpha \, \Delta t}}{\alpha^2 \, \Delta t} \right)\end{aligned} \tag{5-30}$$

Again, with the expressions for the modal amplitude η_{n+1} and velocity $\dot{\eta}_{n+1}$, we have everything that is required for the recursive algorithm. For the purpose of compact notation and efficient programming, the same matrix recurrence expression as for the vibration modes (5-19) can be used:

$$\begin{aligned}\begin{bmatrix} \eta_{n+1} \\ \Delta t \, \dot{\eta}_{n+1} \end{bmatrix} =& \begin{bmatrix} h^{(1)}(\Delta t) + 2\zeta\omega_n \, h^{(0)}(\Delta t) & \frac{h^{(0)}(\Delta t)}{\Delta t} \\ \Delta t \, h^{(2)}(\Delta t) + 2\zeta\omega_n \Delta t \, h^{(1)}(\Delta t) & h^{(1)}(\Delta t) \end{bmatrix} \begin{bmatrix} \eta_n \\ \Delta t \, \dot{\eta}_n \end{bmatrix} \\ &+ \begin{bmatrix} h^{(-1)}(\Delta t) - \frac{h^{(-2)}(\Delta t)}{\Delta t} + \frac{c_2}{\Delta t} & c_1 + \frac{h^{(-2)}(\Delta t)}{\Delta t} - \frac{c_2}{\Delta t} \\ -h^{(-1)}(\Delta t) + \Delta t \, h^{(0)}(\Delta t) - c_1 & h^{(-1)}(\Delta t) + c_1 \end{bmatrix} \begin{bmatrix} \phi_n \\ \phi_{n+1} \end{bmatrix}\end{aligned}$$

This time the required constants are defined as:

$$c_1 \triangleq -\frac{1}{\alpha^2} \qquad \text{and} \qquad c_2 \triangleq -\frac{1}{\alpha^3} \tag{5-31}$$

The matrix recurrence operation can now be performed for damped and undamped Rigid Body Mode $\boldsymbol{\eta}^{\mathrm{RB}}(t)$ and be substituted in (5-7).

5-3-3 Performance

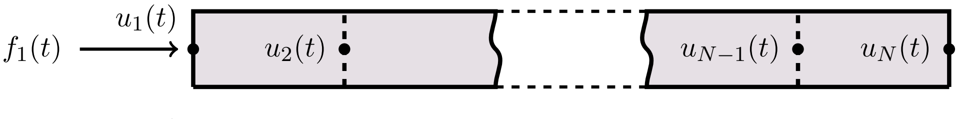

Figure 5-2: Model of a linear bar consisting of N elements of equal length.

In order to see how the matrix recurrence procedure performs compared to a Newmark time integration algorithm, both are tested on a structure made out of N sequentially placed linear bar elements, as seen in figure 5-2. Every time node 1 was excited with a harmonic load of 500 $[Hz]$ and a total of 12887 time steps of 0.67 $[ms]$ were calculated.[8] The required computational time has been measured on a MSc student computer of the department PME[9] and can be found in table 5-1. Figure 5-3 illustrates the found results.

	Newmark Time Stepping		Matrix Recurrence Algorithm	
# DoFs	time stepping	total	time stepping	total
3	1.48	1.56	0.16	0.16
10	1.51	1.61	0.16	0.17
32	1.59	1.66	0.17	0.29
100	1.63	1.71	0.22	0.40
316	2.32	2.41	0.37	1.40
1000	3.44	3.62	0.84	18.1
3162	8.65	9.55	2.33	310

Table 5-1: Required computational time for different values of N.

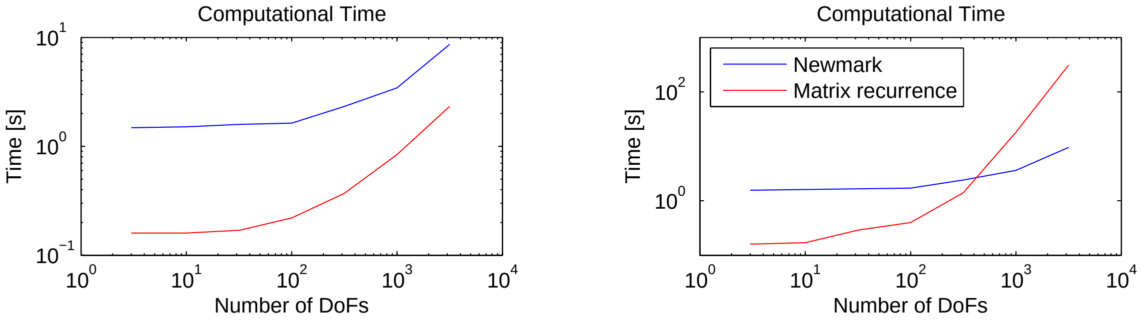

(a) Time stepping time only

(b) Total time

Figure 5-3: Required computational time for different values of N.

In both the table and the figure a distinction is made between the time required for the time stepping itself and the total required time. the total time required also includes pre-allocating memory, in the case of Newmark factorisation and in the case of the matrix recurrence algorithm solving the eigenproblem and building the recurrence matrices.

It can be seen that, for purely the time stepping computational time, the matrix recurrence procedure performs significantly better. For the higher amounts of nodes the algorithm outperforms Newmark by roughly a factor four.

For the total computational time Newmark starts outperforming the recurrence procedure significantly for the higher amounts of nodes. Here memory allocation starts taking more time and also solving the eigenvalue problem starts taking significant amounts of time. All those things only need to be done once, so they do not depend on the amount of time steps, while the time stepping itself does. One can argue up to what degree these results are

---

[8] Making a total of 10 $[ms]$.

[9] Intel Core 2 Duo, 4GB RAM.

reliable since both factorisation in the Newmark algorithm, as computational time for solving the eigenvalue problem in the matrix recurrence procedure is highly subjected to the choice of solver.[10] For models containing towards millions of DoFs or more, incomplete iterative methods for the eigensolutions of the first set of modes can be used significantly reducing computational time compared to calculating the complete set.

For the purpose of validation of the algorithm, displacement and velocity for the first and last node while running the $N = 100$ bar where compared. Those are depicted in figure 5-4. It can be seen that all solutions for the different algorithms are equal.

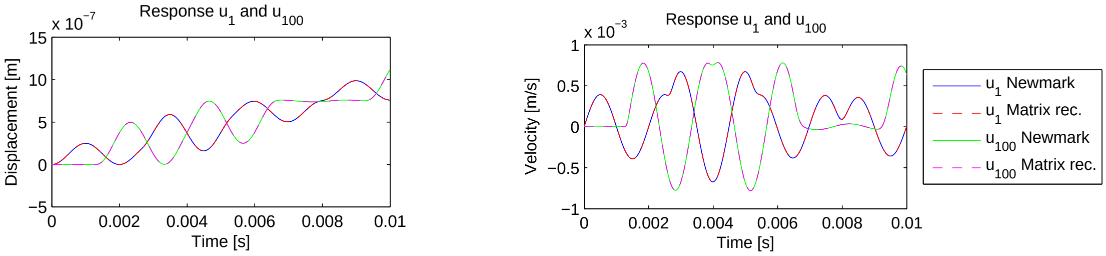

(a) Displacements **(b)** Velocities

Figure 5-4: Comparison of displacement and velocities on node 1 and 100 for the Newmark time integration algorithm and the matrix recurrence procedure.

Remark

One final remark can be made in terms of matrix sparsity. Both algorithms were ran with sparse matrices. The Newmark time integration algorithm benefits from the sequential structure of the DoFs, making the **M**-, **C**- and **K**-matrix very sparse. As structures become more complex, this benefit disappears. The recurrence matrices however, keep the sparsity benefit.

---

[10] In this example a Cholesky factorisation for the Newmark time integration, was used. For the matrix recurrence procedure MATLAB's `eig()`-command was used, which is known to be not very efficient compared to for example a Lanczos solver.

Chapter 6

Practical study

This case study concerns a model of linear bar of length $l = 1.026\,[m]$ divided in 50 elements of equal length. The material is chosen such that its is Young's modulus is $E = 3.1\,[GPa]$ and its density is $\rho = 1330\,[kg/m^3]$. The diameter of the bar is $D = 0.04\,[m]$. These properties are used to build mass- and stiffness matrix $\mathbf{M}$ and $\mathbf{K}$. Next proportional damping is assumed by choosing $\mathbf{C} = 1.5\,10^{-6}\,\mathbf{K}$. The bar is visualised in figure 6-1.

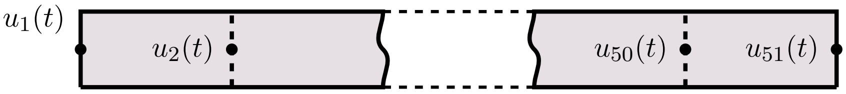

Figure 6-1: Model of a linear bar consisting of 50 elements of equal length. Note that 50 elements require a total of 51 nodes.

First the bar's IRFs will be built using MSP. The influence of a non-perfect Impulse will be investigated. The bars structural response to an excitation is investigated and finally an attempt is made to enhance the calculations for the structural response by means of the techniques from chapter 5.

6-1 IRFs by MSP

First the IRFs of the structure are built using MSP, as discussed in section 4-2. The highest frequency present is $2.58\,10^{-5}\,[rad/s]$. Choosing a Courant's number of 0.5, this yields time steps of $\Delta t = 3.88\,10^{-6}\,[s]$. In total a time of $10\,[ms]$ is taken into account. All 51 modes are taken into account which means that for the discretised model, the IRFs are exact. For the first, middle and last node, respectively nodes 1, 26 and 51 the IRFs for an impulse on node 1 are depicted in figure 6-2.

Figure 6-2a depicts the displacement of the nodes. The figure shows that the nodes are travelling with steps, indicating a wave travelling trough the bar. To gain more insight in

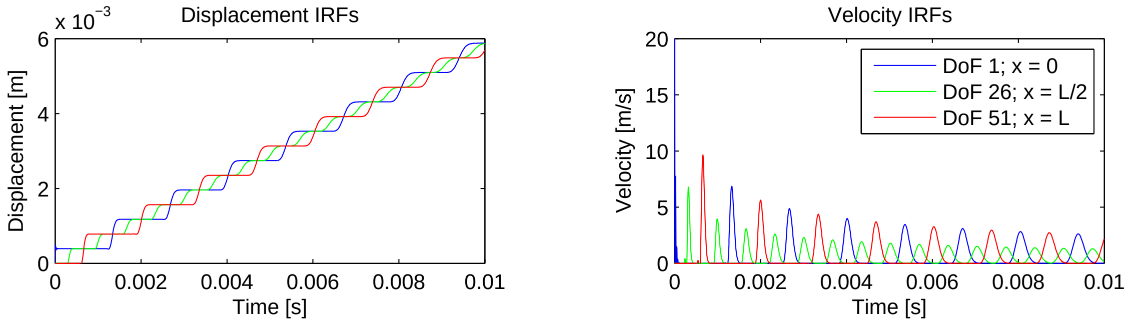

(a) Displacements IRFs.

(b) Velocity IRFs. Note that the graph has been cropped on the velocity axis and does not completely show the first peak of $101\,[m/s]$ for DoF 1.

Figure 6-2: IRFs for nodes 1, 26 and 51 of the 50 element linear bar for an excitation on node 1.

this travelling wave, the velocities of the nodes are shown in figure 6-2b, which clearly shows a velocity wave travelling back and forth trough the bar. Note that the figure is cropped and doesn't show the full firts peak for $\dot{u}_1$. The velocity peaks tend to lower and broaden as time proceeds which can be assigned to the fact that the higher frequency modes damp out faster than the lower frequency modes. The broadening of the peaks temporal, also the means the peaks broaden spatial, which is seen in figure 6-3.

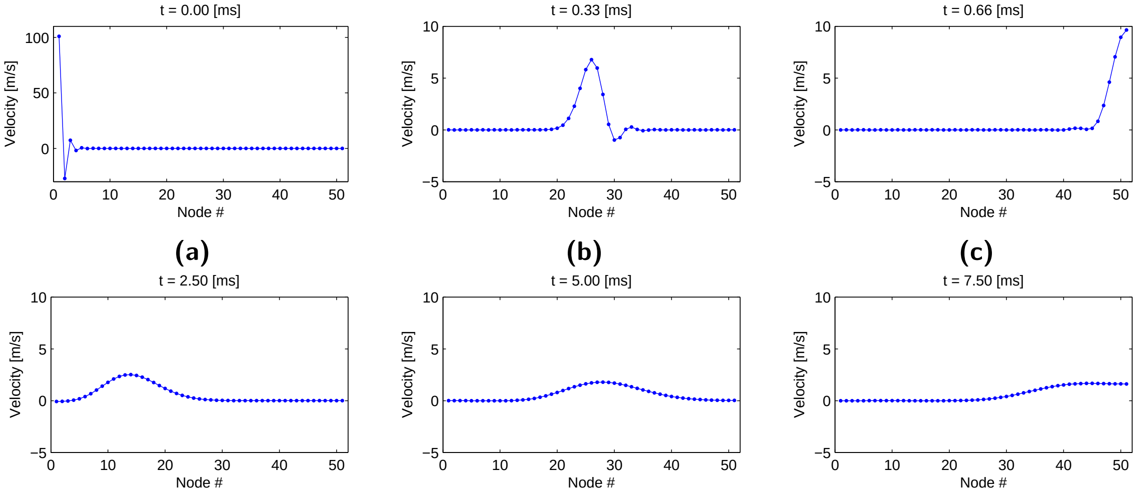

(d) **(e)** **(f)**

Figure 6-3: The travelling velocity wave visualised. Note that y-scale of figure 6-3a differs from the others.

Figure 6-3a shows the velocity distribution at the moment of impact. Node 1 shows the highest velocity, but nodes 2, 3 and 4 also shows some velocity. This is caused by the fact that MSP is used and has a poor spatial convergence as discussed in section 4-4. After a short amount of time this behaviour is no longer visible due to the induced damping.

From a modal perspective, the modal amplitudes over time can be visualised, see figure 6-4.

It is seen, as expected that the higher modes damp out relatively fast, while the lower modes keep contributing to the response.

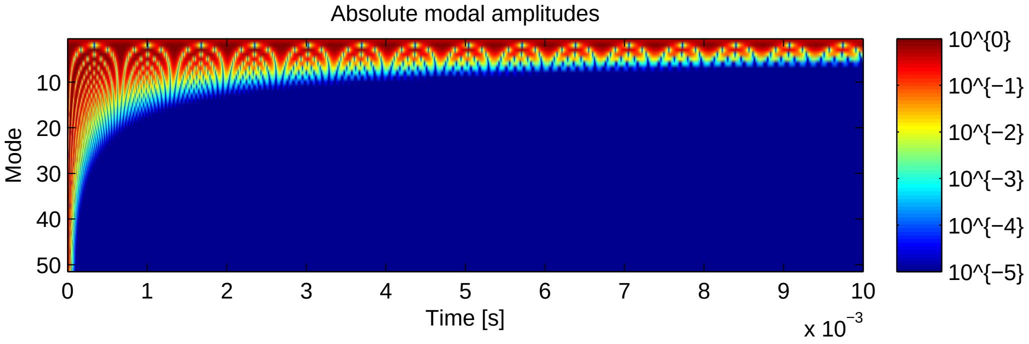

Figure 6-4: The modal amplitudes over time.

6-2 Structural response: Imperfect impulse

Now consider an imperfect impulse as discussed in section 4-3, given by (4-38). Convolving the obtained IRFs with this excitation, gives an approximation of what would have been measured using an impulse like this. Considering the same nodes as above this gives the IRFs shown in figure 6-5.

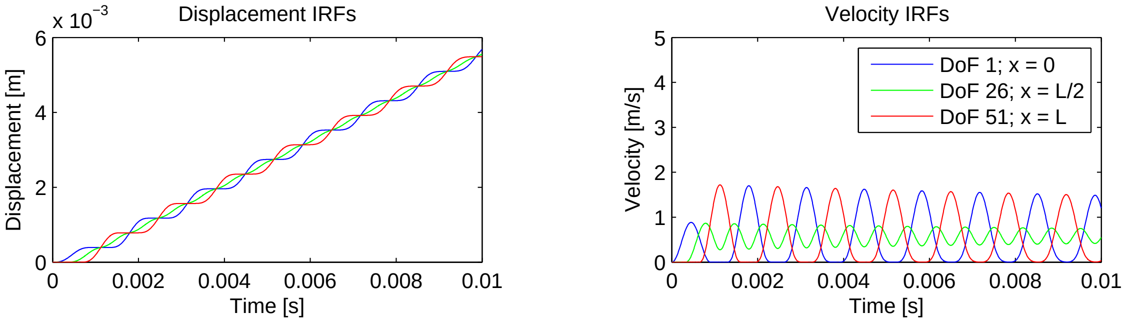

(a) Displacements IRFs

(b) Velocity IRFs

Figure 6-5: Imperfect IRFs for nodes 1, 26 and 51 of the 50 element linear bar for an excitation on node 1.

The velocity IRFs an figure 6-5b give a nice indication on how the travelling wave behaves. It is seen that that the velocity peaks are a lot broader than is the case with the true IRFs. Besides that the center node appears to continuously have velocity. The first peak of node 1 shows roughly half the amplitude compared to the rest. This behaviour was explained in section 4-3.

The spatial velocity distribution is shown in figure 6-6 and contains the same moments in time as figures 6-3a to 6-3c. At $t = 0.00\,[ms]$ nothing has happened yet, since no force is applied yet. Figures 6-6c show that the increase in velocity at the beginning of the impulse has already reached the end of the bar before the full impulse is applied.

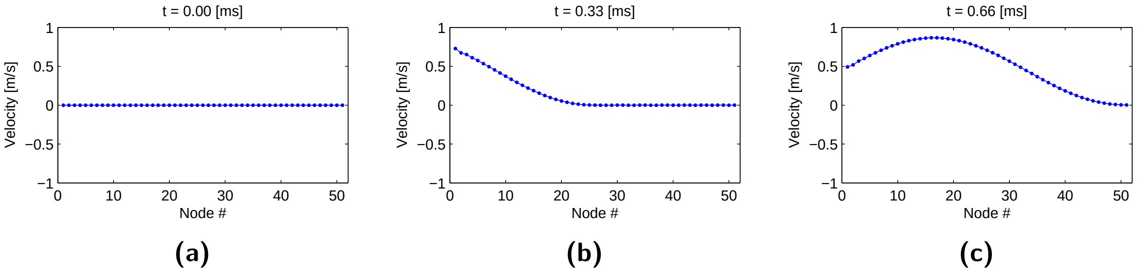

Figure 6-6: The travelling velocity wave visualised.

Also for this IRF the modal amplitudes can be obtained, see figure 6-7. Here it is seen that only some of the lower modes participate. This can be assigned to the fact that only lower modes where excited as explained in section 4-3.[1]

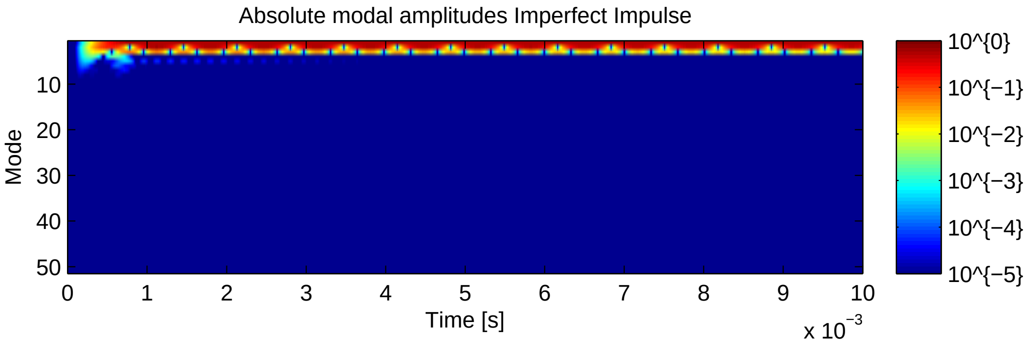

Figure 6-7: The modal amplitudes over time for the imperfect impulse.

6-3 Enhanced structural response: Alternating loads

Next the structures response to some alternating loads is examined. While doing this, the enhancement methods discussed in chapter 5 are evaluated. First the application of those methods is discussed. Afterwards the obtained structural response is discussed and compared to the the response obtained by pure convolution.

6-3-1 Enhancement techniques applied

As discussed in section 5-2, the modal content of the structures IRFs need to be splitten into rigid body, low frequency and high frequency content. The bar contains one RBM pertaining to $\mathbf{X}^{\mathrm{RB}}$. In this is example it is chosen to use $w_c = 5\,10^4\,[rad/s]$. This results in the first 10 modes pertaining to $\mathbf{X}^{\mathrm{LF}}$ and the other 40 modes to $\mathbf{V}$.

With the modal content split, the IRF for the high frequency content can be build by means of projection and can then be truncated as discussed in section 5-1. Consider the high frequency

---

[1] See for instance the frequency spectrum depicted in figure 4-8.

driving point velocity IRF ($\dot{\mathbf{H}}^{\mathrm{HF}}$) for the first node in figure 6-8a. Its maximum amplitude is $88.5\,[m/s]$ at the initial time step. Using a threshold of a factor 1%, this requires the amplitude of the IRF to remain under $8.85\,10^{-1}\,[m/s]$. Figure 6-8b zooms in on the IRF and shows this threshold. The figure depicts that after $0.174[ms]$ the IRF remains within the threshold and can thus be truncated from there. A cosine window, as discussed in section 5-1, is applied. The result is found in figure 6-8c. The windowed IRF now allows to convolve to a solution for the high frequency content.

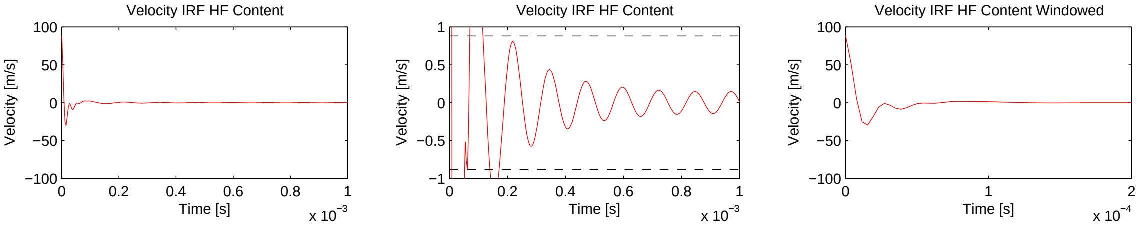

(a) Full IRF. **(b)** Zoomed in on threshold. **(c)** Windowed IRF.

Figure 6-8: High frequency driving point velocity IRF of the first node

6-3-2 Response to excitation

With all preparations for the enhanced response done, a load case can be chosen and applied. A load will chosen and be applied to the first node. The chosen load excites three of the structures eigenfrequency. Initially 5 sinusoidal periods using the bar's fourth eigenfrequency, i.e. $1.40\,10^{4}\,[rad/s]$, with unit amplitude are applied. Next, after $5\,[ms]$, 5 sinusoidal periods using the bar's eighteenth eigenfrequency, i.e. $8.33\,10^{4}\,[rad/s]$, with unit amplitude are applied. And finally after $8\,[ms]$, 5 sinusoidal periods using the bar's 45^{th} eigenfrequency, i.e. $2.45\,10^{5}\,[rad/s]$, with unit amplitude are applied. The load is visualised in figure 6-9. Note that this load contains low frequency content, of which the dynamics are captured in $\mathbf{X}^{\mathrm{LF}}$ and two frequencies pertaining to the lower and higher part of the high frequency content of which the dynamics are captured in $\dot{\mathbf{H}}^{\mathrm{HF}}$.

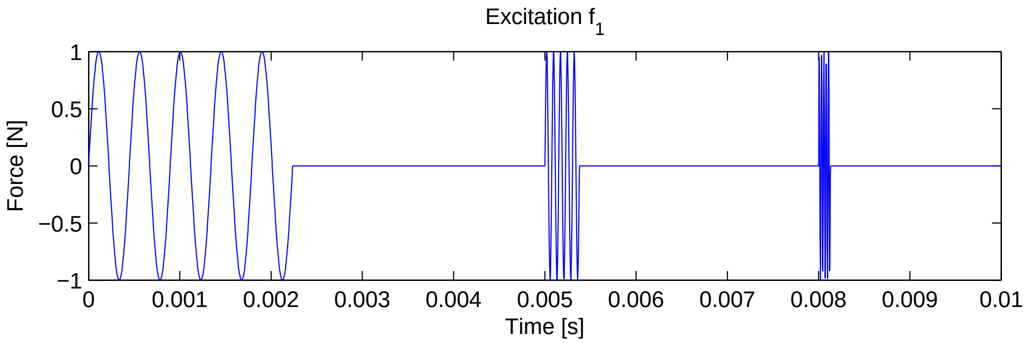

Figure 6-9: The applied load $f_1(t)$.

The response for this load is examined on the first (driving point) node. This is done since high frequency content damps out relatively fast and is thus best shown at the driving point.

The response to the excitation is calculated by convolution over the full time domain for validation purposes and then compared to the solution obtained by the enhanced techniques. For the lower frequency content the matrix recurrence procedure as discussed in section 5-3 is used. The responses for the full time domain is given in figure 6-10a.

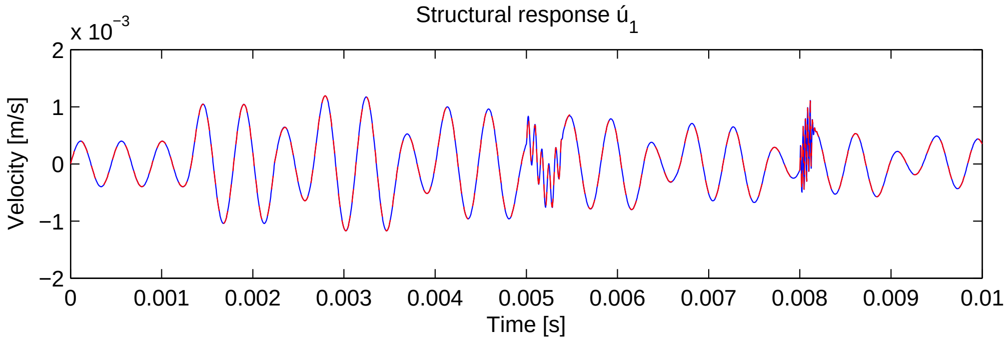

(a) The full time interval $[0; 0.01]$ $[s]$.

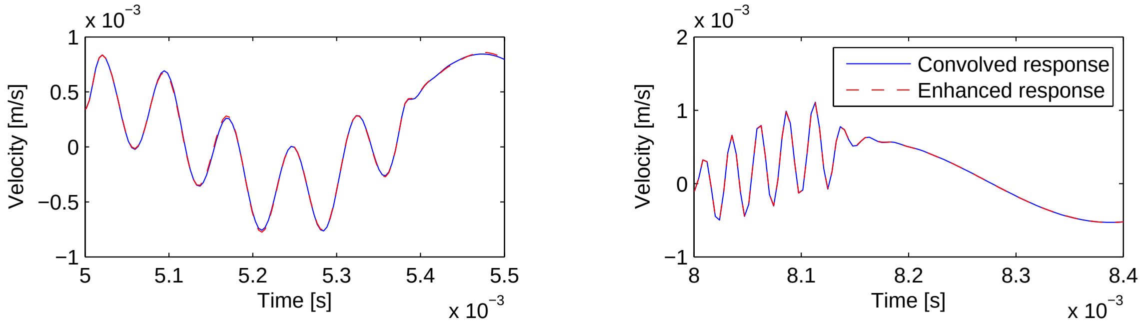

(b) Time interval $[5; 5.5]$ $[ms]$.

(c) Time interval $[8; 8.4]$ $[ms]$.

Figure 6-10: Response of node 1 to the excitation given in figure 6-9 calculated by convolution over the full time domain and using enhancement techniques.

The response obtained by the enhanced techniques appears to match the response obtained by convolution over the full time domain. However, the graph does not clearly depict the responses to the high frequency excitations. Therefore figures 6-10b and 6-10c zoom in to these regions. It can be seen that the response to the high frequency excitations also results in a match in results. This validates the enhancement techniques. It is noticeable that the solution obtained by convolution over the full time domain required 46.1 $[s]$ to compute, while the solution obtained by the enhanced methods required only 1.60 $[s]$ to compute.[2]

---

[2] On the author's personal computer. Intel Core 2 Quad, 2GB RAM.

Chapter 7

Conclusions and recommendations

This chapter concludes part I. First the last few chapters are concluded in section 7-1. Next, recommendations are made in section 7-2.

7-1 Conclusions

This part has shown that it is possible to obtain a solution for a systems structural dynamics in the time domain using Impulse Response Functions. Chapter 3 has shown that an IRF is the structure's response to a unit impulse applied over a infinitesimal time, i.e. a Dirac force and that the structural dynamics as a result of an excitation are found by convolving the IRF with the load over time.

In order to apply this convolution to discrete numerical or measured data, several algorithms have been evaluated. It was shown that it is possible to comprise most algorithms in a more general form using convolution parameters which allows shifting between contributions of various timesteps in the discretised convolution product. This method allows approximation of both the IRF and force loading piecewise linearly which has shown to result in a third order error of the time step for the structural response.

It was found that the temporal discretisation is bound to a maximum time step in relation to the spatial discretisation by Courant's criterion. Courant's criterion describes how a time step should not be chosen larger than the time required for information, e.g. a wave, to travel from one node of the model to the next. When the criterion is not satisfied, not all information that passes by becomes visible in the IRF and in the response. Also it was shown that discretising a continuous model influences the wave propagation speed trough the model and is dependent on the mass distribution of the chosen element.

With the convolution procedure established, obtaining the IRFs themselves has been evaluated in chapter 4. Three different methods of obtaining IRFs have been discussed, namely numerically, analytically and experimentally. It is possible to obtain (a system of) IRFs numerically by for instance Newmark time integration. When doing so, one is subjected to the choice of applying an initial velocity to the system or an initial force (and consequently acceleration). When choosing the initial force condition, the obtained IRFs are delayed by half a time step, but the obtained acceleration IRF does include the initial acceleration of the system required to obtain the initial velocity as a result of the impulse.

It has been proposed in section 4-2 to derive the (system of) IRFs analytically through a Laplace domain approach and applying modal superposition. The Newmark time integrated IRFs using the initial velocity condition resemble the analytically obtained IRFs, although they are sensitive to variations in time stepping whereas the analytically obtained IRFs are not.

Unfortunately the analytical IRFs for acceleration do not describe the initial acceleration required to obtain the initial velocity which is the result of the impulse. This makes it impossible to use these IRFs for convolution. The numerically obtained IRFs by Newmark time integration using the initial force condition does describe this initial acceleration which renders them suited for convolution in order to obtain structural accelerations.[1]

When obtaining a structures IRF experimentally, an imperfect impulse is applied, resulting in IRFs that are slightly delayed and are unable to describe the full frequency spectrum of the systems dynamics. However, this does not disqualify them to convolve to structural responses. The frequency spectrum covered with the impulse directly transfers to how well the structural dynamics as a result of force loading are described. The dynamics that were poorly included in the impulse will be hardly visible when exciting the system accordingly. An experimentally obtained acceleration IRF does describe the initial acceleration as a result of the impulse. This renders also the experimentally obtained acceleration IRF suited for convolution.

Since convolving to structural dynamics for force loadings of increasing length gets computationally extensive, chapter 5 covers three techniques to enhance the computational performance.

It is possible to split the modal content of an IRF into three parts, namely rigid body modes, low frequent modes and high frequent modes. For the rigid body and low frequent modes of which all modal parameters are known it is possible to calculate their contribution by the proposed matrix recurrence procedure, proposed in section 5-3.

The high frequency residual is assumed to decay relatively fast. Its contribution is still solved by convolution, but the rapid decay allows the convolution product to be truncated which enhances computational performance.

The contributions of the rigid body and low frequent modes obtained using the matrix recurrence procedure combined with the contribution of the high frequency content obtained by truncated convolution has shown to yield accurate results significantly reducing computational effort, as was also shown in the case study in chapter 6.

7-2 Recommendations

The IRF truncation procedure discussed above uses windowing to truncate the IRF. The discussed windows are zeroth order or first order discontinuous which does not represent any

---

[1] Although it would be possible to use the analytically obtained acceleration IRFs when it is supplemented with the acceleration which results in the given initial velocity at $t = 0$.

physical effect, like for instance exponential decay, but is rather something mathematical. When regarding coupled responses, it might pay off to have second order discontinous window that does represent something physical in order to prevent unstable coupling behaviour. This behaviour is later discussed in chapter 9 on coupling phenomena.

Furthermore it was seen that when describing the IRFs analytically using MSP, an attempt is made to describe travelling waves using standing waves which has poor spatial convergence, i.e. one requires a significant amount of modes to describe a smooth travelling wave. When IRFs can be described using travelling wave equations this may prove to be more efficient.

Finally, although computational enhancement techniques were covered in this thesis, obtaining responses real-time while using these techniques was not. How accurate and with what sample frequency real-time substructuring can be done is still open for investigation.

Part II

Coupling Structural Dynamics using Impulse Response Functions

Chapter 8

Theory

In chapter 3 the theory on calculating a systems response using its Impulse Response Functions was discussed. When it is desired to couple multiple structures in the time domain using their IRFs, the theory from this chapter needs to be expanded.

This chapter discusses the expanded theory for coupling using IRFs or Impulse Based Substructuring in section 8-1. It will be shown in this chapter that one of the challenges of this method is the computation of the coupling forces. Next an analytical approach to solve the substructuring problem is given in 8-2. Since more often discrete IRFs are available rather than analytical, the substructuring problem requires a discrete method. Literature shows a method applicable only to a discrete problem, in this work referred to as the classical discrete time domain approach. This approach is shown in section 8-3. In section 8-4 an alternative to this method is proposed.

8-1 Introduction to Coupling

Chapter 2 gave a brief introduction into the concepts of substructuring and the two conditions coupling is subjected to; compatibility and equilibrium (2-2). It was shown using the uncoupled system of equations (2-1) and the equilibrium condition (2-2b) that the force vector $\mathbf{f}(t)$ can be supplemented with the interface force vector $\mathbf{g}(t) = -\mathbf{B}^T \boldsymbol{\lambda}(t)$ which is the result of coupling, as shown in equation (2-3).

In chapter 3 it was shown that structural responses in the time domain are obtained by applying the convolution integral as found in (3-7). Following the analogy of chapter 2, this can be expanded with the compatibility condition, as shown in (2-2a) and by supplementing the force vector with the interface forces. Literature often depicts the problem in a partitioned form as shown in equation (8-1).

$$\begin{cases} \mathbf{u}^{(s)}(t) = \displaystyle\int_0^t \mathbf{H}^{(s)}(t-\tau)\,\Big(\mathbf{f}^{(s)}(\tau) - \mathbf{B}^{(s)^T}\boldsymbol{\lambda}(\tau)\Big)\,\mathrm{d}\tau \\ \displaystyle\sum_{s=1}^{N_s} \mathbf{B}^{(s)}\,\mathbf{u}^{(s)}(t) = \mathbf{0} \end{cases} \tag{8-1}$$

The problem has been decomposed into N_s substructures. The response of each substructure is obtained using the convolution product. For the ease of notation and further derivations, a more convenient notation is shown in equation (8-2).

$$\boxed{\begin{cases} \mathbf{u}(t) = \displaystyle\int_0^t \mathbf{H}(t-\tau)\,\Big(\mathbf{f}(\tau) - \mathbf{B}^T\boldsymbol{\lambda}(\tau)\Big)\,\mathrm{d}\tau \\ \mathbf{B}\,\mathbf{u}(t) = \mathbf{0} \end{cases}} \tag{8-2}$$

Here $\mathbf{H}$ is a block-diagonal matrix containing the IRFs of all substructures. The displacement vector $\mathbf{u}$ and force vector $\mathbf{f}$ now contain the information on all subsystems DoFs and $\mathbf{B}$ is set up such that it applies to the full set of displacements $\mathbf{u}$. Note that this notation is also consistent with the notation used in chapter 2.

One challenge to identify is the unknown Lagrange multipler $\boldsymbol{\lambda}(t)$, representing the interface forces, which is situated within the convolution integral. In other words, the interface forces are influenced by the history of the system. One possibility is to time discretise the system and try to solve $\boldsymbol{\lambda}(t)$ for every time step. But first an attempt is made to solve $\boldsymbol{\lambda}(t)$ analytically.

8-2 The Analytical Laplace Domain Approach

When an analytic expression is known for the system of IRFs $\mathbf{H}(t)$ and the applied load $\mathbf{f}(t)$, an analytical expression for the substructured system can be found by using a Laplace domain approach. It will be seen that the approach in the Laplace domain is similar to the approach in the frequency domain as was shown in [2]. The first challenge lies in obtaining an analytical expression for the interface forces $\boldsymbol{\lambda}(t)$. From there on the found expressions can be substituted in the convolution product.

To obtain the Lagrange multiplier $\boldsymbol{\lambda}(t)$, (8-2) is first transformed to the Laplace domain:

$$\mathcal{L}\left\{\begin{matrix} \mathbf{u}(t) = \displaystyle\int_0^t \mathbf{H}(t-\tau)\,\Big(\mathbf{f}(\tau) - \mathbf{B}^T\boldsymbol{\lambda}(\tau)\Big)\,\mathrm{d}\tau \\ \mathbf{B}\,\mathbf{u}(t) = \mathbf{0} \end{matrix}\right\} = \begin{cases} \mathbf{u}(s) = \mathbf{H}(s)\,\Big(\mathbf{f}(s) - \mathbf{B}^T\boldsymbol{\lambda}(s)\Big) \\ \mathbf{B}\,\mathbf{u}(s) = \mathbf{0} \end{cases} \tag{8-3}$$

The convolution product conveniently transforms to a multiplication in the Laplace domain. Pre-multiplication of the top equation of (8-3) with $\mathbf{B}$ and rearranging yields:

$$\mathbf{B}\,\mathbf{H}(s)\,\mathbf{B}^T\,\boldsymbol{\lambda}(s) = \mathbf{B}\,\mathbf{H}(s)\,\mathbf{f}(s) \tag{8-4}$$

Note that in the time domain this notation represents a convolution operation on both sides of the equation. This means that isolating $\boldsymbol{\lambda}(s)$ would represent a deconvolution procedure in the time domain:

$$\boldsymbol{\lambda}(s) = \left(\mathbf{B}\,\mathbf{H}(s)\,\mathbf{B}^T\right)^{-1}\,\mathbf{B}\,\mathbf{H}(s)\,\mathbf{f}(s) \tag{8-5}$$

In practice, this requires $\left(\mathbf{B}\,\mathbf{H}(s)\,\mathbf{B}^T\right)$ to be non-singular for all $s \in \mathbb{C}$. Finally the solution for $\boldsymbol{\lambda}(t)$ is found by the inverse Laplace transformation:

$$\boldsymbol{\lambda}(t) = \mathcal{L}^{-1}\left\{\left(\mathbf{B}\,\mathbf{H}(s)\,\mathbf{B}^T\right)^{-1}\,\mathbf{B}\,\mathbf{H}(s)\,\mathbf{f}(s)\right\} \tag{8-6}$$

Note that in the time domain, this expression does not equal a double convolution operation due to the inverse operation.[1] Substituting (8-5) into the first line of(8-3) finally gives the expression for the response:

$$\mathbf{u}(s) = \left(\mathbf{H}(s) - \mathbf{B}^T\,\left(\mathbf{B}\,\mathbf{H}(s)\,\mathbf{B}^T\right)^{-1}\,\mathbf{B}\,\mathbf{H}(s)\right)\,\mathbf{f}(s) \tag{8-7}$$

As said, it is seen that this method is similar to the LM-FBS method in the frequency domain,[2] which was also shown in chapter 2.

8-2-1 Example: Two DoF System Constrained

This example discusses a two DoF mass-spring-mass system, as seen in 8-1a. This system will be constrained using signed boolean matrix $\mathbf{B}$, such that a single DoF mass-spring system is obtained, as shown in figure 8-1b. For the sake of simplicity a constraining problem is chosen rather than a coupling problem. Note that although this is not a coupling procedure between two substructures, one can argue that constraining is a coupling procedure between one subsystem and the rigid world. Nevertheless, all substructuring theory applies. The effects of this procedure will be demonstrated while the system is excited by an harmonic excitation. Since the characteristics of both systems are fairly simple, the obtained result can easily be verified.

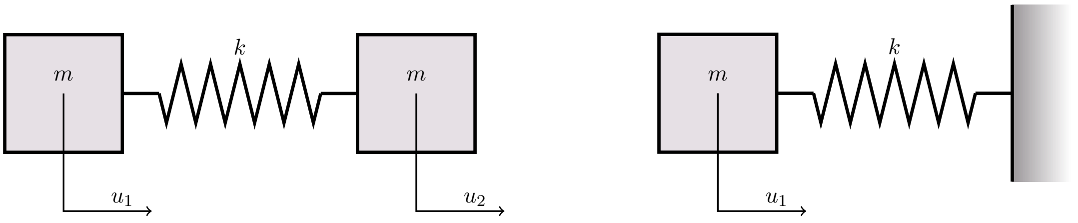

(a) Two DoF mass-spring-mass system.

(b) Single DoF mass-spring system.

Figure 8-1: The two DoF system constrained on the second DoF u_2, such that the single DoF system is obtained.

---

[1] In the Laplace domain multiplication transforms to convolution in the time domain, e.g. $\mathcal{L}^{-1}\{A(s)\,B(s)\} = \int_0^t A(t-\tau)\,B(\tau)\,\mathrm{d}\tau$. However, a multiplication of the inverse of something does not transform to a convolution with that same inverse, e.g. $\mathcal{L}^{-1}\left\{A(s)^{-1}\,B(s)\right\} \neq \int_0^t A^{-1}(t-\tau)\,B(\tau)\,\mathrm{d}\tau$.

For now, we define the mass of both masses to be m and the stiffness of the connecting spring to be k. This yields the following mass- and stiffness matrix:

$$M \triangleq \begin{bmatrix} m & 0 \\ 0 & m \end{bmatrix} \qquad\qquad K \triangleq \begin{bmatrix} k & -k \\ -k & k \end{bmatrix}$$

When decomposing the system into its two modes, it is found that the system has one rigid body mode and one vibration mode with natural frequency:

$$\omega_n = \sqrt{\frac{2k}{m}} \tag{8-8}$$

When setting up the IRF matrix for the system, according to the MSP method described in section 4-2-3, it is found, due to its symmetry, that the IRF is composed of only a driving point IRF h_{dr} and a cross point IRF h_{cr}:

$$\mathbf{H} \triangleq \begin{bmatrix} h_{dr} & h_{cr} \\ h_{cr} & h_{dr} \end{bmatrix} \qquad\qquad \begin{cases} h_{dr}(t) = \frac{1}{2}\,t + \frac{1}{2\omega_n}\,\sin\omega_n\,t \\ h_{cr}(t) = \frac{1}{2}\,t - \frac{1}{2\omega_n}\,\sin\omega_n\,t \end{cases} \tag{8-9}$$

When transforming both IRFs to the Laplace domain, the following expressions are obtained:

$$h_{dr}(s) = \frac{1}{2s^2} + \frac{1}{2(s^2+\omega_n^2)} \tag{8-10a}$$

$$h_{cr}(s) = \frac{1}{2s^2} - \frac{1}{2(s^2+\omega_n^2)} \tag{8-10b}$$

To constrain the second DoF u_2, such that a mass-spring system is obtained, the signed boolean matrix is set up as follows:

$$\mathbf{B}\,\mathbf{u} \triangleq \begin{bmatrix} 0 & 1 \end{bmatrix} \begin{bmatrix} u_1 \\ u_2 \end{bmatrix} = 0 \tag{8-11}$$

It is assumed that the system is excited on the first DoF u_1 with an harmonic load:

$$\mathbf{f}(t) = \begin{bmatrix} f_1(t) \\ 0 \end{bmatrix} \qquad\qquad f_1(t) = \sin\Omega\,t \tag{8-12}$$

In order to obtain a expression for the Lagrange multiplier, expression (8-6) is used. Working out the boolean matrix $\mathbf{B}$, and filling in the required expressions this gives:

$$\begin{aligned} \lambda(s) &= h_{dr}(s)^{-1}\,h_{cr}(s)\,f_1(s) \\ &= \left(\frac{1}{2s^2} + \frac{1}{2(s^2+\omega_n^2)}\right)^{-1} \left(\frac{1}{2s^2} - \frac{1}{2(s^2+\omega_n^2)}\right) \left(\frac{\Omega}{s^2+\Omega^2}\right) \\ &= \frac{\Omega\,\omega_n^2}{(2s^2+\omega_n^2)(s^2+\Omega^2)} \end{aligned} \tag{8-13}$$

It can immediately be seen that the interface force λ has a pole pair in $s = \pm i\frac{\omega_n}{\sqrt{2}}$ which illustrates the change in eigenfrequency of the system. In the time domain this yields

$$\lambda(t) = \frac{\omega_n\left(\sqrt{2}\,\Omega\sin\frac{\omega_n}{\sqrt{2}}\,t - \omega_n\sin\Omega\,t\right)}{2\,\Omega^2 - \omega_n^2} \tag{8-14}$$

for the interface force. Substitution in (8-7) then finally yields

$$\mathbf{u}(s) = \begin{bmatrix} \frac{2\,\Omega}{(2s^2+\omega_n^2)(s^2+\Omega^2)} \\ 0 \end{bmatrix} \tag{8-15}$$

whoms time domain counterpart looks like:

$$\mathbf{u}(t) = \begin{bmatrix} \frac{2\left(\sqrt{2}\,\Omega \sin\frac{\omega_n}{\sqrt{2}}\,t - \omega_n \sin\Omega\, t\right)}{\omega_n(2\,\Omega^2-\omega_n^2)} \\ 0 \end{bmatrix} \tag{8-16}$$

To verify the obtained result, in terms of frequency; it is seen that the obtained response for u_1 goes to ∞ for $\Omega = \omega_n^\star = \frac{\omega_n}{\sqrt{2}}$. Substituting (8-8) yields

$$\omega_n^\star = \sqrt{\frac{k}{m}} \tag{8-17}$$

which is obviously the correct eigenfrequency for the single DoF mass-spring system.

8-3 The Classical Discrete Time Domain Approach

Literature shows how to solve the coupling problem for discrete problems. It was already seen in chapter 3, how the convolution integral gets discretised. Recall (3-12):

$$\mathbf{u}_n = \mathbf{H}_n\,\mathbf{f}_0\,\frac{\Delta t}{2} + \left(\sum_{i=1}^{n-1}\mathbf{H}_{n-i}\,\mathbf{f}_i\,\Delta t\right) + \mathbf{H}_0\,\mathbf{f}_n\,\frac{\Delta t}{2}$$

Supplementing the interface forces into this discretised convolution integral, such that a discrete formulation of (8-2) is obtained, including the compatibility condition, yields:

$$\begin{cases} \mathbf{u}_n = \mathbf{H}_n\left(\mathbf{f}_0 - \mathbf{B}^T\boldsymbol{\lambda}_0\right)\frac{\Delta t}{2} + \left(\sum_{i=1}^{n-1}\mathbf{H}_{n-i}\left(\mathbf{f}_i - \mathbf{B}^T\boldsymbol{\lambda}_i\right)\Delta t\right) + \mathbf{H}_0\left(\mathbf{f}_n - \mathbf{B}^T\boldsymbol{\lambda}_n\right)\frac{\Delta t}{2} \\ \mathbf{B}\,\mathbf{u}_n = \mathbf{0} \end{cases} \tag{8-18}$$

Assuming that the systems state, including interface forces $\boldsymbol{\lambda}$ up to and including time $n-1$ are known, the equation for $\mathbf{u}_n$ is left with only one unknown; the interface forces at the current time step $\boldsymbol{\lambda}_n$. This can be solved in a way which shows some similarities with implicit Newmark time stepping schemes; by computing a predictor, which is later corrected.[7] This predictor can be defined as:

$$\tilde{\mathbf{u}}_n \triangleq \mathbf{H}_n\left(\mathbf{f}_0 - \mathbf{B}^T\boldsymbol{\lambda}_0\right)\frac{\Delta t}{2} + \left(\sum_{i=1}^{n-1}\mathbf{H}_{n-i}\left(\mathbf{f}_i - \mathbf{B}^T\boldsymbol{\lambda}_i\right)\Delta t\right) + \mathbf{H}_0\,\mathbf{f}_n\,\frac{\Delta t}{2} \tag{8-19}$$

This allows us to rewrite the problem to

$$\begin{cases} \mathbf{u}_n = \tilde{\mathbf{u}}_n - \mathbf{H}_0\,\mathbf{B}^T\boldsymbol{\lambda}_n\,\frac{\Delta t}{2} \\ \mathbf{B}\,\mathbf{u}_n = \mathbf{0} \end{cases} \tag{8-20}$$

which allows us to combine both expressions to:

$$\mathbf{B}\,\mathbf{H}_0\,\mathbf{B}^T\boldsymbol{\lambda}_n\,\frac{\Delta t}{2} = \mathbf{B}\,\tilde{\mathbf{u}}_n \tag{8-21}$$

Finally, this allows us to solve the Lagrange multiplier by

$$\boldsymbol{\lambda}_n = \frac{2\left(\mathbf{B}\,\mathbf{H}_0\,\mathbf{B}^T\right)^{-1}\,\mathbf{B}\,\tilde{\mathbf{u}}_n}{\Delta t} \tag{8-22}$$

which concludes the required equations for this algorithm. For every time step, obtaining the response starts with calculating the predictor $\tilde{\mathbf{u}}_n$ using (8-19). Next, the Lagrange multiplier $\boldsymbol{\lambda}_n$ is obtained using (8-22). And finally, the response $\mathbf{u}_n$ is obtained by correcting the predictor using the top equation in (8-20).

Note that (8-22) can only be used when $\left(\mathbf{B}\,\mathbf{H}_0\,\mathbf{B}^T\right)$ is non-singular. This is often the case when using displacement IRFs whoms initial values $\mathbf{H}_0$ equal $\mathbf{0}$. Then $\mathbf{H}_0\,\left(\mathbf{f}_n - \mathbf{B}^T\boldsymbol{\lambda}_n\right)$ does no longer contribute to (8-18), i.e.

$$\begin{cases} \mathbf{u}_n = \mathbf{H}_n\,\left(\mathbf{f}_0 - \mathbf{B}^T\boldsymbol{\lambda}_0\right)\,\dfrac{\Delta t}{2} + \left(\displaystyle\sum_{i=1}^{n-1}\mathbf{H}_{n-i}\,\left(\mathbf{f}_i - \mathbf{B}^T\boldsymbol{\lambda}_i\right)\,\Delta t\right) \\ \mathbf{B}\,\mathbf{u}_n = \mathbf{0} \end{cases} \tag{8-23}$$

As a result, the interface forces at time n, $\boldsymbol{\lambda}_n$ can no longer be calculated, so an alternative method is required. A solution is found in delaying the algorithm in obtaining the Lagrange multiplier $\boldsymbol{\lambda}$ one time step. This results in the algorithm obtaining Lagrange multiplier $\boldsymbol{\lambda}_{n-1}$ using $\mathbf{H}_1$ at time step n.

8-3-1 Modal Interaction

Section 4-2-3 has shown that IRFs can be build using Modal superposition. The fact that responses can be build using MSP was further exploited in section 5-2 and 5-3. One thing that was shown that the response of a structure can build up by calculating the contribution of each mode and summing them up. The next question to investigate is: *'Are the substructure's modes still independent when substructuring techniques are applied?'*

First consider the following definitions for MSP:

$$\mathbf{u}(t) \triangleq \mathbf{X}\,\boldsymbol{\eta}(t) \qquad \text{and} \qquad \boldsymbol{\varphi}(t) \triangleq \mathbf{X}^T\left(\mathbf{f}(t) - \mathbf{B}^T\,\boldsymbol{\lambda}(t)\right)$$

Here $\mathbf{X}$ denotes the matrix containing all eigenmodes, $\boldsymbol{\eta}(t)$ the vector containing all amplitudes, and $\boldsymbol{\varphi}(t)$, the vector with modal contribution factors of the excitation and the interface forces. Also, it is assumed that the modes are mass-normalised, i.e.

$$\mathbf{X}^T\,\mathbf{M}\,\mathbf{X} = \mathbf{M}\,\mathbf{X}\,\mathbf{X}^T = \mathbf{X}\,\mathbf{X}^T\,\mathbf{M} = \mathbf{I} \tag{8-24}$$

Examining equation (8-19), the calculation of the predictor, it is found that it can be rewritten to represent modal content:[2]

$$\begin{aligned}
\tilde{\mathbf{u}}_n &= \mathbf{H}_n \left(\mathbf{f}_0 - \mathbf{B}^T \boldsymbol{\lambda}_0\right) \frac{\Delta t}{2} + \left(\sum_{i=1}^{n-1} \mathbf{H}_{n-i} \left(\mathbf{f}_i - \mathbf{B}^T \boldsymbol{\lambda}_i\right) \Delta t\right) + \mathbf{H}_0 \, \mathbf{f}_n \frac{\Delta t}{2} \\
\tilde{\mathbf{u}}_n &= \mathbf{H}_n \, \mathbf{M} \, \mathbf{X} \, \boldsymbol{\varphi}_0 \frac{\Delta t}{2} + \left(\sum_{i=1}^{n-1} \mathbf{H}_{n-i} \, \mathbf{M} \, \mathbf{X} \, \boldsymbol{\varphi}_i \, \Delta t\right) + \mathbf{H}_0 \, \mathbf{M} \, \mathbf{X} \, \boldsymbol{\varphi}_n^\dagger \frac{\Delta t}{2} \\
\mathbf{X} \, \tilde{\boldsymbol{\eta}}_n &= \mathbf{H}_n \, \mathbf{M} \, \mathbf{X} \, \boldsymbol{\varphi}_0 \frac{\Delta t}{2} + \left(\sum_{i=1}^{n-1} \mathbf{H}_{n-i} \, \mathbf{M} \, \mathbf{X} \, \boldsymbol{\varphi}_i \, \Delta t\right) + \mathbf{H}_0 \, \mathbf{M} \, \mathbf{X} \, \boldsymbol{\varphi}_n^\dagger \frac{\Delta t}{2} \\
\tilde{\boldsymbol{\eta}}_n &= \mathbf{X}^T \, \mathbf{M} \, \mathbf{H}_n \, \mathbf{M} \, \mathbf{X} \, \boldsymbol{\varphi}_0 \frac{\Delta t}{2} + \left(\sum_{i=1}^{n-1} \mathbf{X}^T \, \mathbf{M} \, \mathbf{H}_{n-i} \, \mathbf{M} \, \mathbf{X} \, \boldsymbol{\varphi}_i \, \Delta t\right) + \mathbf{X}^T \, \mathbf{M} \, \mathbf{H}_0 \, \mathbf{M} \, \mathbf{X} \, \boldsymbol{\varphi}_n^\dagger \frac{\Delta t}{2}
\end{aligned}$$

Now it is seen that as long as $\mathbf{X}^T \, \mathbf{M} \, \mathbf{H}(t) \, \mathbf{M} \, \mathbf{X}$ results in a diagonal matrix, the modal equations are fully uncoupled for the calculation of the predictor from the given loads. This is obviously the case since when the IRF is build using MSP, which can only be the case when the modal content was fully uncoupled in the first place.

Next consider equation (8-22), used to determine the interface forces. This equation can also be rewritten to represent modal content:[3]

$$\begin{aligned}
\boldsymbol{\lambda}_n &= \frac{2 \left(\mathbf{B} \, \mathbf{H}_0 \, \mathbf{B}^T\right)^{-1} \mathbf{B} \, \tilde{\mathbf{u}}_n}{\Delta t} \\
\boldsymbol{\lambda}_n &= \frac{2 \left(\mathbf{B} \, \mathbf{H}_0 \, \mathbf{B}^T\right)^{-1} \mathbf{B} \, \mathbf{X} \, \tilde{\boldsymbol{\eta}}_n}{\Delta t} \\
\mathbf{X}^T \, \mathbf{B}^T \, \boldsymbol{\lambda}_n &= \frac{2 \, \mathbf{X}^T \, \mathbf{B}^T \left(\mathbf{B} \, \mathbf{H}_0 \, \mathbf{B}^T\right)^{-1} \mathbf{B} \, \mathbf{X} \, \tilde{\boldsymbol{\eta}}_n}{\Delta t} \\
\boldsymbol{\varphi}_n^\ddagger &= \frac{2 \, \mathbf{X}^T \, \mathbf{B}^T \left(\mathbf{B} \, \mathbf{H}_0 \, \mathbf{B}^T\right)^{-1} \mathbf{B} \, \mathbf{X} \, \tilde{\boldsymbol{\eta}}_n}{\Delta t}
\end{aligned}$$

Now in a similar way it can be argued that as long as $\mathbf{X}^T \, \mathbf{B}^T \left(\mathbf{B} \, \mathbf{H}_0 \, \mathbf{B}^T\right)^{-1} \mathbf{B} \, \mathbf{X}$ results in a diagonal matrix, the modal equations are fully uncoupled when calculating interface forces. This is however no longer the case due to the usage of boolean matrices $\mathbf{B}$. This means that interaction between the modes takes place due to coupling. From a different perspective one can say that various combinations of the original modes result in the modes of the coupled structure.

---

[2] Note that in the derivation below $\boldsymbol{\varphi}_n^\dagger$ represent the modal participation factors of the excitation without the interface forces at time step n.

[3] Note that in the derivation below $\boldsymbol{\varphi}_n^\ddagger$ represents the modal participation factors of the interface forces, such that $\boldsymbol{\varphi}_n^\dagger - \boldsymbol{\varphi}_n^\ddagger = \boldsymbol{\varphi}_n$.

8-4 The Inverse IRF Filter Approach

Besides the previously discussed methods, an alternative method can be thought of to solve the system of equations given in (8-2). In the section 8-2 it was mentioned that isolating the Lagrange multiplier $\boldsymbol{\lambda}(t)$ involved an operation that represents a deconvolution operation in the time domain. In case an explicit deconvolution operation exists for this problem in the time domain, this offers an alternative method.

8-4-1 Introduction to inverse filter approach

It was shown previously in [12,16] that it is possible to obtain a structures IRF using its excitation and response, both in the time domain. This method is named the inverse force filter approach. In practice, the method resembles the deconvolution of equation (3-5):

$$u(t) = \int_0^t h(t-\tau)\, f(\tau)\, \mathrm{d}\tau$$

When a function $f^{inv}(t)$ exists which convolves with the excitation force $f(t)$ to a perfect dirac function, the IRF of the structure $h(t)$ can be isolated by

$$h(t) = \int_0^t f^{inv}(t-\tau)\, u(\tau)\, \mathrm{d}\tau \tag{8-25}$$

In summary, the method shows how a convolution integral can be unraveled to obtain one of the functions inside when the other function is known and its inverse function can be obtained.

8-4-2 The Inverse IRF Filter

Similar to the inverse force filter mentioned above, a inverse IRF filter is desired which commences the property to convolve with the IRF to a perfect Dirac function;

$$h(t) * h^{inv}(t) = \delta(t) \tag{8-26}$$

Note that the asterisk symbol represent the convolution operation. This notation will be used more often trough this section for the convenience of notation. Now equation (8-26) can be rewritten using a Toeplitz matrix notation[4] for the convolution. The time dimension is now discretised to vector entries, yielding:

$$H\, h^{inv} = \delta \tag{8-27}$$

---

[4] During this derivation it is chosen not to use the bold font as has been done with other vectors and matrices. This has been done to prevent confusion with 'spatial' vectors and matrices where entries of the vectors and matrices represent information for varying DoFs, where the entries of the vectors and matrices used in this derivation represent only another moment in time.

with

$$H \triangleq \underbrace{\begin{bmatrix} h_1 & 0 & \cdots & 0 \\ \vdots & h_1 & & \vdots \\ h_N & \vdots & \ddots & 0 \\ 0 & h_N & & h_1 \\ \vdots & & \ddots & \vdots \\ 0 & \cdots & 0 & h_N \end{bmatrix}}_{\text{M by Q=M-N+1}}, \quad h^{inv} \triangleq \underbrace{\begin{bmatrix} h_1^{inv} \\ h_2^{inv} \\ \vdots \\ h_Q^{inv} \end{bmatrix}}_{\text{Q by 1}} \quad \text{and} \quad \delta \triangleq \underbrace{\begin{bmatrix} \delta_1 \\ \delta_2 \\ \vdots \\ \delta_M \end{bmatrix}}_{\text{M by 1}} \tag{8-28}$$

One is subjected to the choice of how to describe the Dirac function discrete. This is elaborated on in section 8-4-4. Pre-multiplication of the equation with H^T then yields

$$H^T \, H \, h^{inv} = H^T \, \delta \tag{8-29}$$

Where $(H^T \, H)$ represents linear auto-correlation matrix R. $H^T \, H = R$ of which the columns are filled with linear auto-correlation function $r = h \star h$. The above equation can thus be rewritten to

$$R \, h^{inv} = H^T \, \delta \tag{8-30}$$

Finally it is possible to isolate the inverse IRF filter by

$$h^{inv} = R^{-1} \, H^T \, \delta \tag{8-31}$$

Now the length and quality of the inverse IRF filter are influenced by the choice for the Dirac vector. First of all the length of the Dirac vector M can be varied. Typically a length of 3 to 5 times the length of the IRF N is used. A longer Dirac vector basically forces the inverse IRF filter $h^{inv}(t)$ to yield a dirac function $\delta(t)$ after convolution with the IRF $h(t)$ for a longer period of time.

The second choice to be made is where in the Dirac vector the impulse is placed. Choosing a position other then δ_1 resembles a delayed Dirac. At the same time, the position of the impulse determines what column of the auto-correlation matrix is used to obtain the inverse IRF filter. Since the middle column contains the most information about the IRF, this is often a safe choice. For the resulting inverse IRF filter, this means that the outcome can contain information that applies to a time earlier than the starting point of the IRF, i.e. $t < 0$.

8-4-3 Properties of the inverse IRF Filter

In practice there is a lot more to it when calculating an inverse IRF filter, than applying the formulas above. This section therefore discusses some properties of the inverse IRF filter. There will often be referred to two perspectives on the inverse IRF filter:

1. The inverse IRF can be seen as a description of the linear combination of IRFs that result in a Dirac function.
2. In a frequency domain perspective the inverse IRF filter can be seen as $h^{inv}(t) = \mathcal{F}^{-1}\left\{\mathcal{F}\left\{h(t)\right\}^{-1}\right\}$.

These perspectives are used while discussing the inverse IRF filter's properties below.

Existence

Not every IRF has an inverse filter per definition. For diverging IRFs there exist no inverse filter. From the perspective of linear combination, this can be explained by the fact that it is not possible to make a linear combination of IRFs that results in the Dirac function. From the frequency domain perspective, one can argue that its Fourier transform does not exist for $\omega = 0$.

Causality

When the inverse IRF filter contains information for $t < 0$, the filter is allowed to become non-causal. Choosing the impulse in the Dirac filter at another point then the starting point, basically resembles rewriting (8-26) to

$$h(t) * h^{inv}(t - o) = \delta(t - o) \tag{8-32}$$

The inverse IRF is delayed by the same amount o, as the Dirac function. Technically all values for $h^{inv}(t - o)$ for $t < o$ should equal zero, in order for the filter to be causal. When this is not the case, future information of $h(t)$ would be required to convolve to the present time step of the Dirac function. For an academic example, used to demonstrate the filter, this does not yield a problem. Keeping in mind the goal of real-time substructuring however, non-causality for the inverse IRF filter renders a problem, since no future information of the excitation is available to calculate the response for the present time.

From the perspective where the inverse filter represents the linear combination of IRFs, one can say that when information from a time later in the IRF than the present time is required, the inverse IRF filter is non-causal.

This happens for example using a velocity IRF obtained by the Newmark time integration algorithm using the initial force condition. The IRF is zero at time zero and the velocity as a result of the impulse shows up on the next time step. In order to obtain a Dirac at time $t = 0$, the velocity from the next time step (future) is required. So the inverse IRF filter can only be build using a linear combination where the first IRF used starts one step before $t = 0$, rendering the inverse filter non-causal.

In a more general sense one can say that when the IRFs value at $t = 0$ does not have the highest amplitude, the filter is automatically rendered non-causal.

Finiteness

By definition, a Finite Impulse Response (FIR) requires an Infinite Impulse Response (IIR) as its inverse, also see [18]. If both would be finite, then convolution would not be able to yield the Dirac function over the full time-domain $-\infty < t < \infty$. However, it can be seen in (8-28) that with an IRF of N samples, requiring a Dirac function of M samples, yields an inverse IRF filter of Q samples, which is finite. Both the IRF and the inverse IRF are thus able to convolve to a Dirac function over the time interval spanned by the M samples in the Dirac vector.

The convolution of the finite IRF and inverse IRF will however approximate the infinite Dirac function when one of the FIRs is an approximation of the IIR when padded with zeros. This should be this should be the case for the IRF. From the linear combination perspective, this would yield the same for the inverse filter. For all $t < 0$, the IRF equals zero by definition. For all time after the last time step of the IRF $t > t_N$, the IRF should approximate zero. Consequently, the remaining amplitude of the IRF at its truncation point t_N has a direct influence on the quality of the inverse IRF filter.

This can be directly linked to the discussion on existence above. When the IRF diverges and is truncated at t_N, the FIR does not approximate the IIR padded with zeros. This results in a diverging finite inverse filter which does not make an accurate approximation of its infinite variant.

Sensitivity to temporal discretisation

The inverse IRF filter can in two ways sensitive to deviations in the temporal discretisation, i.e. the size of time step Δt.

First, if the inverse IRF is expected to contain Dirac(-like) content represented by $\frac{1}{\Delta t}$ this will show. This is discussed and can be seen in the example, both in section 8-4-4.

Secondly, for the limit case where $\Delta t \to 0$, obtaining an inverse filter is expected to become numerically unstable. From the frequency domain perspective, one can argue that the Fourier transform of the IRF $\mathcal{F}\{h(t)\}$ will show higher frequency content for a decreasing time step. Since the amplitude of high frequency content is expected to decreases for increasing frequency, this IRF in the frequency domain (FRF), is poorly conditioned. Taking the inverse of something poorly conditioned leads towards numerical instability.

From a time domain perspective one can say that for decreasing time steps, the autocorrelation matrix R starts containing[5] higher frequency content with smaller eigenvalues. Now for a decreasing time step, the Dirac becomes shorter in time, requiring higher frequency content that due to its small eigenvalues requires higher contribution to construct the Dirac, rendering this process numerically unstable for the limit case.[6]

---

[5] By means of a single value decomposition.

[6] Note that is in fact possible to disregard higher frequency content found in matrix R by setting these eigenvalues to zero and reconstructing it. As a result it is not possible to build a perfect Dirac function, but since only high frequent content is missing, this will only show with high frequent excitations. This is very similar to obtaining the IRF by an imperfect impulse which also lacks high frequency content, as was shown in section 4-3-1.

8-4-4 Application to a single DoF

Now that the inverse IRF filter is familiar, it can be applied to a substructuring problem. For the purpose of clarity, a problem with a single compatibility equation is discussed first.

The convolution integral for the substructured system with convolution integral replaced by the asterisk symbol is the starting point of the derivation, combined with the compatibility condition:

$$\begin{cases}\mathbf{u}(t) = \mathbf{H}(t) * (\mathbf{f}(t) - \mathbf{B}^T \boldsymbol{\lambda}(t)) \\ \mathbf{B}\,\mathbf{u} = \mathbf{0}\end{cases} \tag{8-33}$$

Pre-multiplying the top equation with $\mathbf{B}$ and rearranging gives

$$\mathbf{B}\,\mathbf{H}(t) * \mathbf{B}^T \boldsymbol{\lambda}(t) = \mathbf{B}\mathbf{H}(t) * \mathbf{f}(t) \tag{8-34}$$

Similar as seen before, but now in the time domain this represents on the right side the compatibility violation of the uncoupled solution for the given excitation and on the left side the same compatibility violation as a result of the interface forces. Since $\mathbf{B}$ is not a function of time, the left side can be rearranged to

$$\mathbf{B}\,\mathbf{H}(t)\,\mathbf{B}^T * \boldsymbol{\lambda}(t) = \mathbf{B}\mathbf{H}(t) * \mathbf{f}(t) \tag{8-35}$$

Since the compatibility matrix $\mathbf{B}$ consists of only one row, representing one equation, $\mathbf{B}\,\mathbf{H}(t)\,\mathbf{B}^T$ reduces to a scalar quantity in time, a (combination of) driving point IRFs, denoted by $h_{BB}(t)$. This directly implies that the Lagrange multiplier is also a scalar quantity in time and that the right side of the equation allows pre-multiplication with a scalar quantity in time. Taking this into account yields

$$h_{BB}(t) * \lambda(t) = \mathbf{B}\mathbf{H}(t) * \mathbf{f}(t) \tag{8-36}$$

When the inverse filter of $h_{BB}(t)$ is known, it can be convolved with both sides of the equation, eventually isolating the Lagrange multiplier $\lambda(t)$:

$$\begin{aligned} h_{BB}(t) * \lambda(t) &= \mathbf{B}\mathbf{H}(t) * \mathbf{f}(t) && \text{(8-37a)} \\ h_{BB}^{inv}(t) * h_{BB}(t) * \lambda(t) &= h_{BB}^{inv}(t) * \mathbf{B}\mathbf{H}(t) * \mathbf{f}(t) \\ \delta(t) * \lambda(t) &= h_{BB}^{inv}(t) * \mathbf{B}\mathbf{H}(t) * \mathbf{f}(t) \\ \lambda(t) &= h_{BB}^{inv}(t) * \mathbf{B}\mathbf{H}(t) * \mathbf{f}(t) && \text{(8-37b)} \end{aligned}$$

As seen above, the inverse IRF filter method is able to solve for the Lagrange multiplier which can be used to solve the substructuring problem, provided that $h_{BB}^{inv}(t)$ exists.

Dimensions in discretisation

As mentioned earlier, when constructing the inverse IRF filter using (8-31), one is subjected to a choice for the Dirac vector δ. In theory the continuous Dirac function is defined as

$$\delta(t) \triangleq \begin{cases}\infty & \text{for} \quad t = 0 \\ 0 & \text{for} \quad t \neq 0\end{cases} \tag{8-38}$$

which is dimensionless and has the property that $\int_{-\infty}^{\infty} \delta(t)\,\mathrm{d}t = 1$. Now for the discrete δ there are two options:

(A) $\delta[n]$ is a vector with all zeros and at the entry representing $t = 0$ has a value of $\frac{1}{\Delta t}$. The vector δ is then assigned dimension $[s^{-1}]$, but still satisfies $\int_{-\infty}^{\infty} \delta(t)\,\mathrm{d}t = \sum_n \delta[n]\,\Delta t = 1$.

(B) $\delta[n]$ is a vector with all zeros and at the entry representing $t = 0$ has a value of 1. This renders the vector dimensionless, but integration now results in $\int_{-\infty}^{\infty} \delta(t)\,\mathrm{d}t = \sum_n \delta[n]\,\Delta t = \Delta t \neq 1$.

Now this choice determines the dimension of the inverse IRF filter $h^{inv}[n]$. Let us assume the response the IRF and force convolve to over time, has arbitrary dimension $[\xi]$. Consequently the IRF $h[n]$ has dimension $[\xi \,/\, Ns]$. Following option A or B, this renders the dimension of the inverse filter $h^{inv}[n]$ as follows:

(A) $h^{inv}[n]$ has dimension $[N \,/\, \xi]$, such that $\sum_i^n h^{inv}[n-i]\,h[i] = \delta[n]$ with dimension $[s^{-1}]$. This implies that the inverse IRF filter depends on the time step size.

(B) $h^{inv}[n]$ has dimension $[Ns \,/\, \xi]$, such that $\sum_i^n h^{inv}[n-i]\,h[i] = \delta[n]$ which is dimensionless. This render the inverse IRF filter independent of the time step size.

Now in order to obtain the interface force according (8-37b), let us define the uncoupled response as

$$\breve{u}[n] \triangleq \sum_i^n \mathbf{B}\mathbf{H}[n-i]\,\mathbf{f}[i]$$

The above options require the following in order to obtain interface forces in $[N]$:

(A) $\lambda[n] = \sum_i^n h^{inv}[n-i]\,\breve{u}[i]$ with dimension $[N]$.

(B) $\lambda[n] = \sum_i^n h^{inv}[n-i]\,\breve{u}[i]\,\frac{1}{\Delta t}$ with dimension $[N]$.

Both options have their advantages and disadvantages. Method A does not use a dimensionless Dirac vector, while method B does. Method B requires an additional division by Δt, which is a little counter intuitive in a convolution and one could argue that this division should be implied in the inverse IRF filter, rendering method A.

Example: Two DoF System Constrained

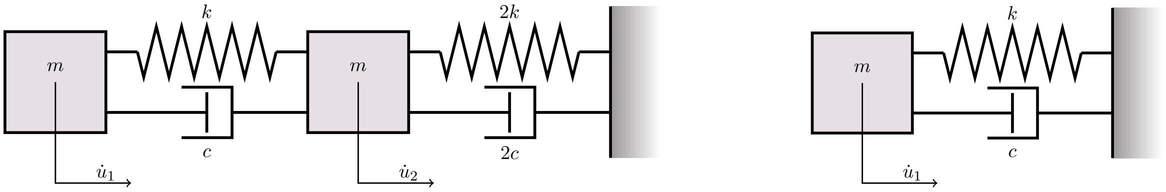

(a) Two DoF mass-spring-damper system.

(b) Single DoF mass-spring-damper system.

Figure 8-2: The two DoF system constrained on the second DoF u_2, such that the single DoF system is obtained.

Let us consider a 2-DoF mass-damper-spring-system as depicted in figure 8-2a. The parameters are chosen as follows: Mass $m = 1\,[kg]$, damping constant $c = 20\,[Ns/m]$ and stiffness $k = 1000\,[N/s]$. Courant numbers of 0.01 and 0.1 are used yielding in time steps of respectively $0.39\,[ms]$ and $3.9\,[ms]$. and In this example velocity information is used rather than displacement. The left mass, with $\dot{u}_1$, is excited with a Dirac impulse, while the right mass is constrained, i.e. $\mathbf{B} = [\,0 \quad 1\,]$, such that the system in figure 8-2b is obtained.

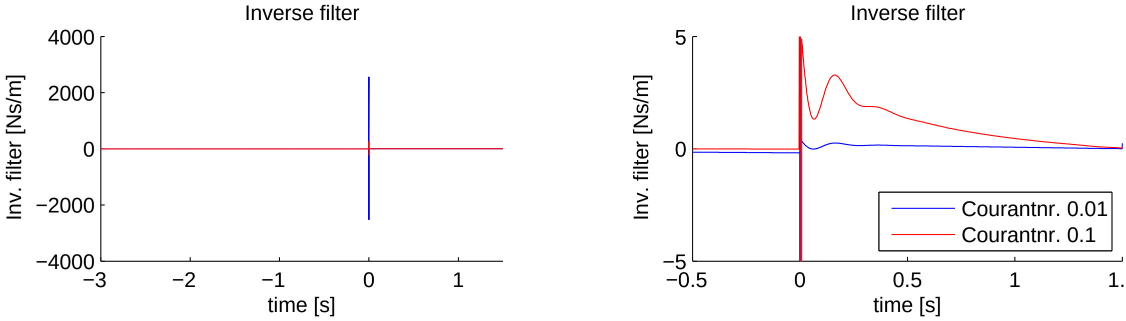

(a) Over the full calculated time interval **(b)** Zoomed in on transient behaviour.

Figure 8-3: The inverse IRF filter $\dot{h}_{22}^{inv}(t)$.

In this scenario, due to our choice for $\mathbf{B}$, the IRF to be converted is $h_{BB}(t) = \dot{h}_{22}(t)$. Its inverse IRF filter is depicted in figure 8-3a. At $t < 0$, the filter seems to approximate zero, which is desired, since it is desired to obtain a causal filter.

At $t = 0$ a positive and negative impulse seem to occur. Note the difference in amplitude for the different time steps. This difference is explained in the section above, in this study method A is used, rendering the inverse IRF filter time dependant. These peaks indicate Dirac(-like) functions and according to method A the Dirac function is time step dependent.[7]

After these Dirac-like functions some transient behaviour occurs, this is better visible in figure 8-3b and is again dependent on the time step size.

Now for the Lagrange mutiplier $\lambda(t)$, substituting in (8-37b) yields:

$$\lambda(t) = \dot{h}_{22}^{inv}(t) * \dot{h}_{21}(t) * f_1(t) \tag{8-39}$$

The result is found in figure 8-4a. It can be seen that the interface force constructed by the inverse IRF filter with Courant's number 0.01 performs equally to the reference solution. The Courant's number 0.1 solution shows some slight deviation from the reference solution.

Now examining the substructured results, it is seen in figure 8-4b that the solutions of both time steps make a fair approximation of the reference solution. It can now be verified if the compatibility criterion, $\dot{u}_2 = 0$, is satisfied. Figure 8-4c shows that this is initially not entirely the case. Nevertheless this does prove the concept of the inverse IRF filter. The compatibility

---

[7] When option B would have been chosen, this effect would not have been present.

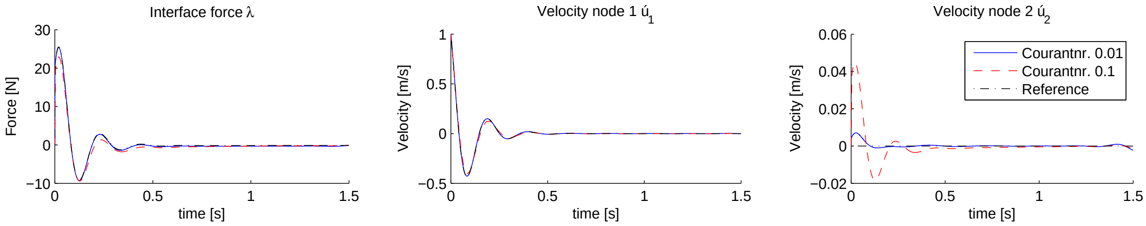

(a) The interface force keeping node 2 in place. **(b)** The resulting velocity at node 1 **(c)** The resulting velocity at node 2, which should equal zero.

Figure 8-4: Application of the inverse IRF filter. Two different time steps are depicted and compared to a reference solution. 0.01 times the critical time step (blue) and 0.1 time the critical time step (red).

violation is again time step dependent, which implies that the compatibility decreases with decreasing time step.

8-4-5 Application to multiple DoFs

Obviously, when the substructuring problem prescribes multiple compatibility equations it is no longer possible to take the inverse of $h_{BB}(t)$ as described above, since $\mathbf{B}\,\mathbf{H}(t)\,\mathbf{B}^T$ is no longer a scalar quantity in time. However, an equivalent solution to this problem exists. The solution will be demonstrated using a boolean matrix $\mathbf{B}$ with two rows.

Say $\mathbf{B}\,\mathbf{H}(t)\,\mathbf{B}^T$ is denoted with $\mathbf{H}_{BB}(t)$. In order to isolate the Lagrange multiplier vector, it is required to find an inverse filter matrix such that the matrix convolution yields a Dirac function identity matrix.

$$\mathbf{H}_{BB}^{inv}(t) * \mathbf{H}_{BB}(t) = \begin{bmatrix} \delta(t) & 0 & 0 \\ 0 & \ddots & 0 \\ 0 & 0 & \delta(t) \end{bmatrix} \tag{8-40}$$

Note that in this notation the convolution is performed along the time dimension, while matrix multiplication is assumed for the spatial dimensions.

In order to find $\mathbf{H}_{BB}^{inv}(t)$, let us first discuss the case of a matrix containing time invariant quantities. Its inverse matrix consists of the inverse of the determinant (scalar) multiplied with a residual matrix. For the two DoF example the inverse of matrix $\mathbf{A}$is given by

$$\mathbf{A} = \begin{bmatrix} a & b \\ c & d \end{bmatrix} \tag{8-41}$$

$$\mathbf{A}^{-1} = \frac{1}{\det(\mathbf{A})} \begin{bmatrix} d & -b \\ -c & a \end{bmatrix} = \frac{1}{a\,d - b\,c} \begin{bmatrix} d & -b \\ -c & a \end{bmatrix} \tag{8-42}$$

Multiplying matrix $\mathbf{A}$ with its inverse obviously results in the identity matrix. It can now be shown that if the $\frac{1}{\det(\mathbf{A})}$ part is rewritten by changing all its multiplications to convolutions and interpreting the inverse operation as the inverse filter that this yields the inverse IRF matrix filter. For a two DoF $\mathbf{H}_{BB}(t)$ matrix, this is done as follows. Say

$$\mathbf{H}_{BB}(t) = \begin{bmatrix} h_{11}(t) & h_{12}(t) \\ h_{21}(t) & h_{22}(t) \end{bmatrix}_{BB} \tag{8-43}$$

then its inverse is found by

$$\mathbf{H}^{inv}_{BB}(t) = \Big[h_{11}(t) * h_{22}(t) - h_{12}(t) * h_{21}(t)\Big]^{inv} * \begin{bmatrix} h_{22}(t) & -h_{12}(t) \\ -h_{21}(t) & h_{11}(t) \end{bmatrix} \tag{8-44}$$

It can be shown that convolution of both $\mathbf{H}_{BB}(t)$ and $\mathbf{H}^{inv}_{BB}(t)$ yields the desired Dirac identity matrix by using the associative property of convolution. For the purpose of clarity, first the 'convolution determinant' is defined

$$\det{}^*(\mathbf{H}_{BB}(t)) \triangleq h_{11}(t) * h_{22}(t) - h_{12}(t) * h_{21}(t) \tag{8-45}$$

Next, this is substituted in the convolution equation:

$$\begin{aligned} \mathbf{H}^{inv}_{BB}(t) * \mathbf{H}_{BB}(t) &= \Big[\det{}^*(\mathbf{H}_{BB}(t))\Big]^{inv} * \begin{bmatrix} h_{22}(t) & -h_{12}(t) \\ -h_{21}(t) & h_{11}(t) \end{bmatrix} * \begin{bmatrix} h_{11}(t) & h_{12}(t) \\ h_{21}(t) & h_{22}(t) \end{bmatrix} \\ &= \Big[\det{}^*(\mathbf{H}_{BB}(t))\Big]^{inv} * \begin{bmatrix} \det{}^*(\mathbf{H}_{BB}(t)) & 0 \\ 0 & \det{}^*(\mathbf{H}_{BB}(t)) \end{bmatrix} \\ &= \begin{bmatrix} \delta(t) & 0 \\ 0 & \delta(t) \end{bmatrix} \end{aligned} \tag{8-46}$$

So it can be seen that there exists an inverse IRF matrix filter $\mathbf{H}^{inv}_{BB}(t)$, if an inverse filter of $\det^*(\mathbf{H}_{BB}(t))$ can be found. Analogue to (8-37), the Lagrange multiplier vector $\boldsymbol{\lambda}(t)$ is found by

$$\boldsymbol{\lambda}(t) = \mathbf{H}^{inv}_{BB}(t) * \mathbf{BH}(t) * \mathbf{f}(t) \tag{8-47}$$

which solves the substructuring problem.

Remark. When the number of compatibility equations grows, this method grows rather comprehensive. In that case it may be more efficient to choose an approach trough the Fourier domain:

$$\mathbf{H}^{inv}_{BB}(t) = \mathcal{F}^{-1}\left\{\mathcal{F}\left\{\mathbf{H}_{BB}(t)\right\}^{-1}\right\} \tag{8-48}$$

which is basically similar to the Laplace approach shown in section 8-2.

8-4-6 Physical interpretation of inverse IRF filter

To assign some physical interpretation to the inverse IRF filter in equation

$$\dot{h}(t) * \dot{h}^{inv} = \delta(t) \tag{8-49}$$

start with recalling equation (3-5) for an arbitrary single DoF system, which can for velocities be written as

$$\dot{u}(t) = \dot{h}(t) * f(t) \tag{8-50}$$

Now imagine that the system has a prescribed velocity

$$\dot{u}(t) = \delta(t) \tag{8-51}$$

Now the only force that is capable to cause this velocity is then given by

$$f(t) = \dot{h}^{inv}(t) \tag{8-52}$$

where $\dot{h}^{inv}(t)$ is given by (8-49), such that when substituting all in (8-50), the equation is satisfied.

In terms of causality, the inverse IRF filter is said to be causal, if and only if no forces are applied to the system prior to obtaining the Dirac velocity.

One could argue, since the IRF $h(t)$ represents the transient mobility for a Dirac force, that $h^{inv}(t)$ represents some sort of impedance to velocity[8] for a Dirac velocity. Note that one can argue whether a Dirac velocity is something physical. The same goes for Dirac displacements.[9] For accelerations this does represent something physical, but not all calculated acceleration IRFs are suited to convolve to a structural response as was discussed in 4-4.

From another perspective; the inverse IRF filter represents the linear combination of delayed IRFs such that a Dirac function is obtained.

8-5 Discussion

Concluding this chapter, two topics require some additional discussion. First a comparison is made between the three discussed methods to obtain the interface forces $\boldsymbol{\lambda}(t)$. After that, the interface problem in terms of its quantity is discussed.

8-5-1 The different approaches

Comparing the three algorithms, one can argue that the analytical Laplace domain approach discussed in section 8-2 and the inverse IRF filter approach discussed in section 8-4 are implicitly the same technique. With the analytical Laplace domain approach the $\left(\mathbf{B}\,\mathbf{H}(s)\,\mathbf{B}^T\right)^{-1}$ term said to represent the deconvolution operation is also the Laplace transformed[10] of the inverse IRF filter introduced later.

---

[8] Similar as with a damper as found in most mass-spring-damper systems.

[9] Note that the IRF for velocity shows discontinuous non-smooth behaviour which we consider to be physical, so this makes it arguable whether a Dirac velocity would exist. The IRF for displacement does not show discontinuous behaviour, therefore a Dirac displacement seems very non-physical.

[10] Note that this can be done similar in the Fourier domain, as was done while discussing the properties of the inverse IRF filter in section 8-4-3.

The difference with the classical discrete method discussed in section 8-3 is the fact that the latter method computes one time step for $\boldsymbol{\lambda}(t)$ at a time, while the other two methods calculate the interface forces for the full domain, either directly the full time domain or using the Laplace domain. Now it was discussed for the inverse IRF filter, that this can only be done when a solution for the inverse IRF filter in fact exists in the time domain, see for details section 8-4-3.

The classical discrete time domain approach circumvents this, by not using an inverse operation over the full domain, but only on the zeroth time step. In the case that this value does not exist, this is circumvented by using the first time step. This where the difference in handling time history comes in. This method does require the time history of the excitation and interface forces to obtain the interface force for the current step, while the other two methods do not require this.

This relates directly to the compatibility criterion. Since the classical discrete method uses time history data, the compatibility equation is solved explicitly every time step. For the IRF filter method, this is not the case and thereby taking into account that the IRF filter is discrete and can consequently not describe the exact IRF filter makes this method prone to compatibility errors.

8-5-2 The interface problem

With the IBS equation established in the previous section, the question remains, on what quantity to couple? Displacements, velocities or accelerations? In section 4-4 it was explained that in acceleration IRFs[11] are not suited to use in the convolution product. This leaves displacement and velocity IRFs. Now recall both IRFs for a single DOF system (4-19):

$$\begin{aligned} u(t) &= \frac{\sin(\omega_d\, t)}{m\,\omega_d}\, e^{-\zeta\,\omega_n\, t} \\ \dot{u}(t) &= \frac{\omega_n}{m\,\omega_d}\, \cos(\omega_d\, t + \theta)\, e^{-\zeta\,\omega_n\, t} \end{aligned}$$

Now let us, for the sake of the discussion below, linearise these functions around $t = 0$ and discretise by substituting $t = n\,\Delta t$ and for the sake of simplicity, disregard the damping:

$$\left.\begin{aligned} u_n &\approx \frac{n\,\Delta t}{m} \\ \dot{u}_n &\approx \frac{1}{m} \end{aligned}\right\} \qquad \text{for} \qquad \omega_n\, n\,\Delta t \ll 1$$

The trend to decrease the time step size Δt in order to capture more high frequency information, now shows to have have a negative effect when using displacement IRFs in the discrete time domain impulse based substructuring that was discussed in section 8-3. For the displacement IRF, $\mathbf{H}_0$ is in theory equal to zero, thus the first time step $\mathbf{H}_1$ is used to calculate the Lagrange multipliers. The above linearisation now shows that for a decreasing time step

---

[11] With exception of acceleration IRFs obtained by Newmark time integration using initial force conditions and measured acceleration IRFs.

$\Delta t \to 0$, the displacement at the first time step decreases $\mathbf{H}_1 \to \mathbf{0}$. Since the displacements at this time step are used to obtain the Lagrange multipliers $\boldsymbol{\lambda}_{n-1}$[12], this operation becomes very sensitive to errors. Eventually this can lead to unwanted behaviour in the coupling, which is discussed in the next chapter. In contradiction to the displacement IRFs, the velocity IRFs do not encounter this problem. At time step $t = 0$ the velocity IRF is at its maximum value, which is least sensitive to errors. Therefore it is safe to conclude that applying the time discrete IBS scheme is preferably used with velocity IRFs.

When extending this topic to coupling with experimental data or coupling numerical models to experimental data. Some additional challenges arise. In [14] it is proposed to couple a structure given by its acceleration IRF, representing the 'experimental data' to a structure of which the mass-, damping- and stiffness matrix are given. This coupling is done based on accelerations and is integrated in a Newmark time stepping algorithm. The advantage of this method is that it actually allows coupling using accelerations. Note that during measurements, often acceleration is measured. This is possible since no 'true' acceleration IRFs are used in the convolution[13], which is also not the case with experimental data. The alternative is to couple on velocities. It is possible to obtain exact IRFs for the velocities from models, but this also requires velocity measurements for the experimentally obtained substructure.

---

[12] Recall section 8-3 and equation 8-23.

[13] When obtaining IRFs using a Newmark time integration scheme, approximations of the IRFs are obtained, as discussed in chapter 4, when choosing the initial applied force as initial condition, this does yield an approximation for the acceleration IRF that can be used in convolution.

Chapter 9

Coupling phenomena

In the previous chapter it was seen that the IBS algorithm is dependant on multiple variables among which the Impulse Response Function $\mathbf{H}(t)$ and the Lagrange multiplier representing the interface forces $\boldsymbol{\lambda}(t)$. For the method discussed in section 8-3 the first time step, $\mathbf{H}_0$ for velocities or $\mathbf{H}_1$ for displacements is of particular importance. It can be shown that small errors in the IRF can lead to undesired behaviour during the coupling; incomplete coupling and unstable coupling. These phenomena are discussed in this chapter and in particular, their exact causes.

The theory behind all 'cause and effect' relations in this chapter are demonstrated using two bars to be coupled with highly simplified IRFs which allow clear illustration of the effects at hand. Note that the explanations often refer to the methods discussed in 8-3. However, most of them are also directly applicable to situations where $\boldsymbol{\lambda}(t)$ is obtained using an inverse IRF filter, as discussed in section 8-4.

9-1 Sample IRF, coupling and propagation

The bar as discussed above consists of 5 nodes. A wave travels from one end to the other in exactly one second. For this sample, velocities are considered. The undamped discrete model satisfies the impulse equation, since the discrete IBS schemes are based on impulses. The outer nodes contain half the amount of mass and therefore show double the response in comparison to the inner nodes. Finally, damping is introduced in the model using an exponential decay. Every second (or crossing) the response is decreased to 80%. To achieve this a time constant $\alpha = \ln(0.8)$ is chosen and the undamped response is multiplied with $e^{\alpha t}$. The first two seconds of the structure excited by a Dirac impulse are depicted in figure 9-1. A time step of $\Delta t = 0.25\,[s]$ is used, which is conveniently chosen, exactly the time required for the pulse to travel from node to node.

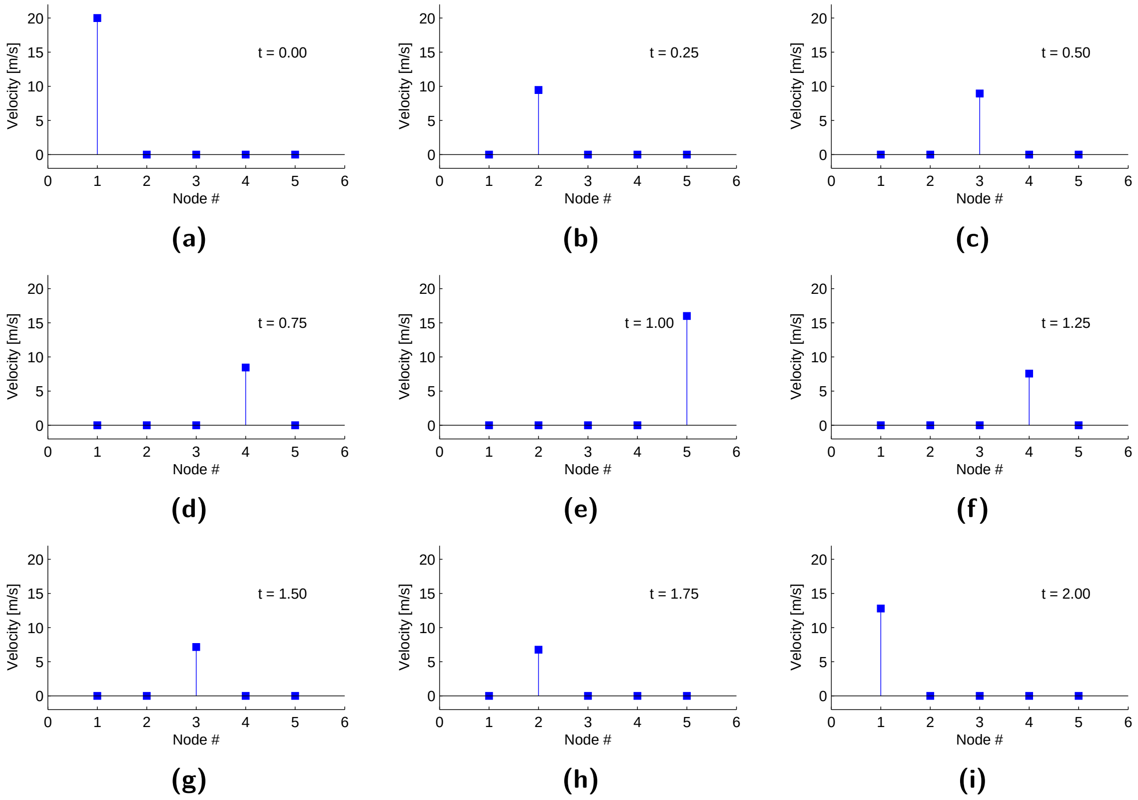

Figure 9-1: The first two seconds of a wave induced by an impulse on node 1 propagating in the sample bar

When coupling two of these bars, this means that the coupled nodes combined mass is equal to the inner nodes resulting in a nice propagating wave. How coupling works in the IBS algorithm is illustrated in figure 9-2. As mentioned above, this sample uses two equal bars with IRFs as described above. The first bar is represented by node 1 to 5 in blue, while the second bar is represented by node 6 to 10 in red. Only the first bar is excited with an impulse on node 1 (similar as in the IRF in figure 9-1). This initial situation is illustrated in figure 9-2a.

Recall equation (8-18)

$$\mathbf{u}_n = \mathbf{H}_n \left(\mathbf{f}_0 - \mathbf{B}^T \boldsymbol{\lambda}_0\right) \frac{\Delta t}{2} + \left(\sum_{i=1}^{n-1} \mathbf{H}_{n-i} \left(\mathbf{f}_i - \mathbf{B}^T \boldsymbol{\lambda}_i\right) \Delta t\right) + \mathbf{H}_0 \left(\mathbf{f}_n - \mathbf{B}^T \boldsymbol{\lambda}_n\right) \frac{\Delta t}{2}$$

for the substructuring algorithm and equation (8-22)

$$\boldsymbol{\lambda}_n = \frac{2 \left(\mathbf{B}\,\mathbf{H}_0\,\mathbf{B}^T\right)^{-1} \mathbf{B}\,\tilde{\mathbf{u}}_n}{\Delta t}$$

used to calculate the Lagrange multiplier. Also recall that $\mathbf{H}$ is a block diagonal matrix containing the IRF matrices of both substructures.

From (8-22) can be seen that there is only a Lagrange multiplier other than zero calculated when there is an incompatibility on the interface, i.e. $\mathbf{B}\,\tilde{\mathbf{u}}_n \neq 0$. This means that, as long as no incompatibility has occurred, which is for the first three time steps, the response is simply given by $\mathbf{H}_n\,\mathbf{f}_0$. This corresponds to the induced wave travelling trough the first (blue) bar, while the second (red) bar does nothing.

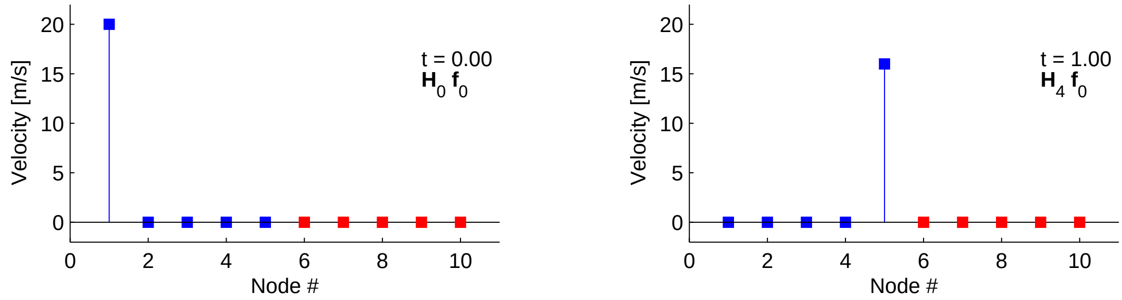

(a) Initial situation. The combined structure is excited at node 1.

(b) At $t = 1.00$, the system, only given by $\mathbf{H}_4\,\mathbf{f}_0$ reaches an incompatible situation.

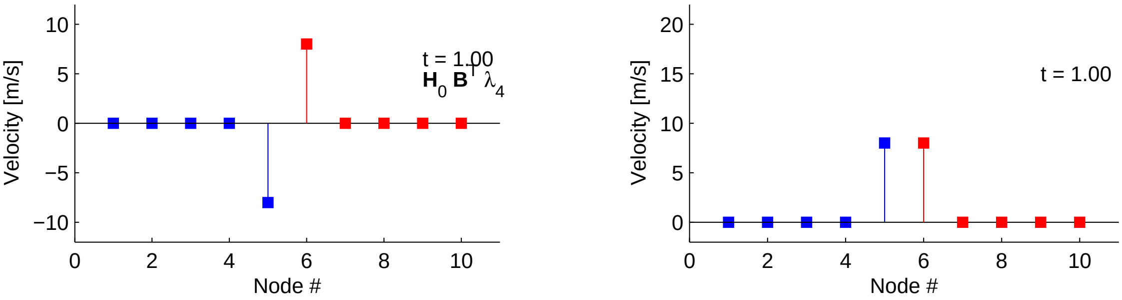

(c) The IBS algorithm calculates the required Lagrange multiplier to maintain compatibility during this time step. Its contribution is given by $-\mathbf{H}_0\,\mathbf{B}^T\,\boldsymbol{\lambda}_4\,\frac{\Delta t}{2}$.

(d) The response of the original impulse combined with the contribution of the calculated Lagrange multiplier restores compatibility.

Figure 9-2: Coupling explained: How the Lagrange multiplier is used to satisfy compatibility.

At the fourth time step ($t = 1.00$), the induced wave has crossed the bar and is now causing an incompatibility, since the response for node 5 and 6 are not equal, i.e. $\mathbf{B}\,\tilde{\mathbf{u}}_n \neq 0$. This is seen in figure 9-2b. To ensure compatibility, the required Lagrange multiplier is calculated using (8-22). Its contribution is depicted in figure 9-2c. Now complementing the predicted incompatible response, with the contribution of the Lagrange multiplier, yields the response as expected.

When investigating how the wave propagates onwards in the second bar, the next time step can be investigated. At $t = 1.25$ the contribution of the original excitation $\mathbf{H}_5\,\mathbf{f}_0$, seen in figure 9-3a, is the wave travelling backwards trough the first element. However, since the previous time step there is also a second contribution to take into account in the form of Lagrange multiplier $\boldsymbol{\lambda}_4$. According to (8-18) its contribution is now given by $-\mathbf{H}_1\,\mathbf{B}\,\boldsymbol{\lambda}_4\frac{\Delta t}{2}$. This contribution is depicted in figure 9-3b. Their combined response is shown in 9-3c, which

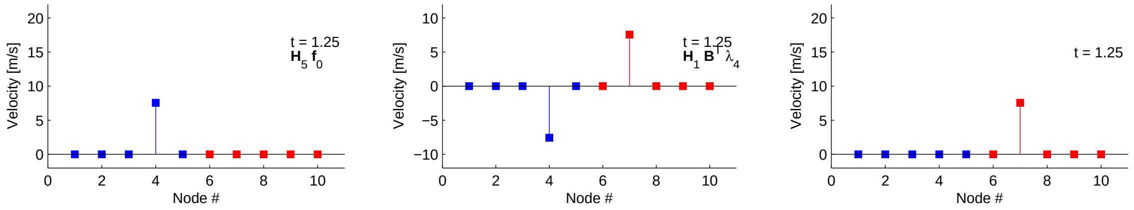

(a) Contribution of the original excitation **(b)** Contribution of the new Lagrange multiplier **(c)** The combined response

Figure 9-3: Wave propagation in the second (red) bar visualised.

shows proper propagation of the wave. The response of the Lagrange multiplier cancels out the returning wave in the first bar and causes it to show up in the second bar. There is no incompatibility, and thus no need for a Lagrange multiplier to restore this.

One can imagine that if the second bar would be infinitely long, the wave would never return to the interface. For the first (blue) bar that would mean that for $n > 4$ the effects of the original excitation $\mathbf{f}_0$ have to be cancelled out by the effect of the one Lagrange multiplier $\boldsymbol{\lambda}_4$, i.e. according to (8-18):

$$\mathbf{u}_n^{(A)} = \left(\mathbf{H}_n\,\mathbf{f}_0 - \mathbf{H}_{n-4}\,\mathbf{B}^T\,\boldsymbol{\lambda}_4\right)^{(A)} = \mathbf{0} \qquad \text{for} \qquad n > 4 \tag{9-1}$$

Here superscript (A) denotes the first (blue) of the two bars. Since an exponential decay was chosen for this example, it is possible to satisfy this condition.

9-2 Incomplete coupling

The previous section has demonstrated coupling using the simple bar example. By deviating from this example, various undesired coupling phenomena can be demonstrated. This section is dedicated to phenomena that cause incomplete coupling.

There is a distinction to be made between incomplete coupling and unstable coupling. Incomplete coupling covers everything that causes improper wave propagation, while unstable coupling covers the phenomena that cause diverging amplitudes for the structures response.

9-2-1 Failing Courant's criterion

In section 3-3-1 Courant's criterion was introduced. Courant's criterion states that there is a limit in the ratio between the spacial and temporal discretisation based on the wave propagation speed in the material that should be maintained in order to guarantee stable time stepping, as was seen in equation (3-17). This criterion can also be applied to IBS.

Failing Courant's criterion translates to using a time step bigger than the time required for information (a wave) travelling from one node to the next. So not all information of the travelling wave passes every node, including the interface node. This means that at the interface, a part of the wave is already reflected at the interface, before the coupling[1] takes place.

When examining the example from section 9-1, a time step of $\Delta t = 0.75$ could have been used, rather than the demonstrated $\Delta t = 0.25$.[2] When coupling, the response of the blue bar for the first and second time step would have respectively been given by figures 9-1d and 9-1g. In between the travelling wave has passed the interface, but this stays unobserved due to the large time step. The results is that no coupling gas taken place between those two time steps and thus, the wave does not propagate into the next bar, but stays in the first bar.
In summary, no interface force is obtained due to the fact that the wave was not observable at the interface node. A lack of interface force results in a compatibility violation, but due to failing Courant's criterion, this also stays unobserved.

9-2-2 Compatibility violations

It was discussed in section 8-1 that compatibility is one of the coupling requirements. The classical discrete time domain approach, section 8-3 explicitly satisfies the compatibility criterion every time step, but the inverse IRF filter approach, section 8-4 does not, which can lead to incompatibilities.

Consider equation (8-35):

$$\mathbf{B}\,\mathbf{H}(t)\,\mathbf{B}^T * \boldsymbol{\lambda}(t) = \mathbf{B}\mathbf{H}(t) * \mathbf{f}(t)$$

Both sides of the equation represent an interface gap. The right side represents the interface gap caused when the system would be uncoupled, while the left side of the equation represents the same gap that the interface force closes. This equation is not explicitly solved during each time step, allowing both sides of the equation to become unequal, resulting in incompatibility.

9-2-3 Non-causal IRF

In the end on section 9-1, it was demonstrated using figure 9-3, how a wave propagates after coupling. One important part that was illustrated is that the reflecting wave caused by the original excitation, figure 9-3a, is cancelled out by the effects of the Lagrange multiplier, figure 9-3b. It was already said that for proper propagation, these two have to keep cancelling each other out for all future time steps, see equation (9-1).

When those two contributions stop cancelling each other out, a residue of the original wave shows up, as if it has reflected on the interface. Consider the situation from figure 9-3, but now $\mathbf{H}_5$ contains an error, such that the contribution is higher than it should be, as seen in figure 9-4a. The contribution of the Lagrange multiplier $\boldsymbol{\lambda}_4$ stays unaltered, figure 9-4b. The result is that the combined response shows a small peak on node 4. See figure 9-4c.

---

[1] Calculating Lagrange multipliers and correcting the response.

[2] Which does satisfy Courant's criterion.

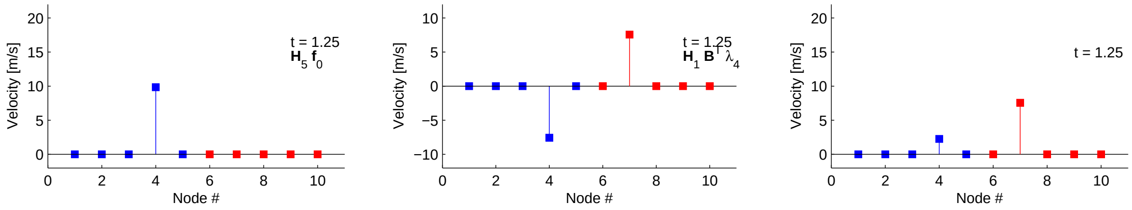

(a) Elevated contribution of the original excitation **(b)** Contribution of the Lagrange multiplier **(c)** The combined response

Figure 9-4: Wave propagation and a minor reflection caused by the IRF being non-causal.

9-2-4 Induced delays in the IRF

In a manner analogue to the manner in the previous section, it can be shown what happens when a delay is introduced in the IRF. When a delay is introduced in the IRF at some point, the reflecting wave from the original contribution can no longer be cancelled out, as was required by (9-1).

Now consider again the same situation as was shown in figure 9-3, but this time the IRF of the first (blue) bar still shows the pulse at node 5 at time $t = 1.25$, rather than back at node 4. This is shown in figure 9-5a. The contribution of the Lagrange multiplier remains unaltered, as is shown in figure 9-5b. The result, rather than a positive and negative value on node 4 cancelling each other out, is a negative pulse at node 4 travelling in backwards direction, followed by a positive pulse on node 5.

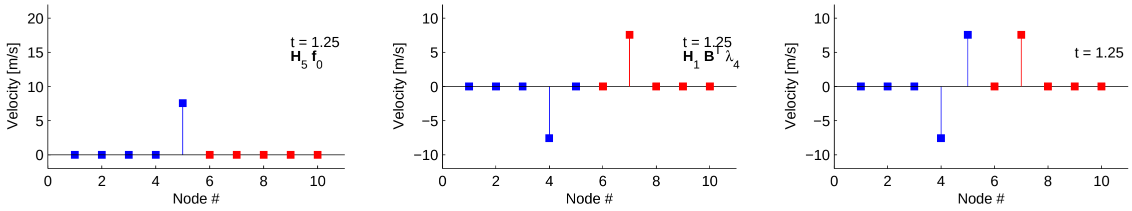

(a) Delayed contribution of the original excitation **(b)** Contribution of the Lagrange multiplier **(c)** The combined response

Figure 9-5: Wave propagation and a positive/negative impulse reflecting on the interface, caused by a delay in the IRF.

9-3 Unstable coupling

Besides coupling being incomplete, coupling can also be unstable. The coupling is said to be unstable when energy is added to the system when an interface force is present. When this is done repeatedly, the response of the system diverges. Typically, this happens when the IRF of a structure show non-causal behaviour, i.e. when a structure excited with a certain amount of energy, contains more energy at a later point in time. As it will turn out, the first time step of the IRF $\mathbf{H}_0$ has a big influence on this.

This unstable coupling will be demonstrated using the same bar example as used trough this section. The IRF shown in section 9-1 demonstrated stable coupling, since the IRF had a exponential decay. Below marginally stable (conservative) coupling will be demonstrated. This scenario will then be altered to demonstrate unstable coupling

9-3-1 Example: Marginally stable coupling (conservative)

Consider the IRF from figure 9-1, but this time without the exponential decay. Its first, third and fifth time step are given in figure 9-6 for an impulse applied to the left side. Naturally, the impulse will travel back and forth trough the bar as time proceeds. Obviously, since the bar is symmetric, the IRF is symmetric for an impulse applied to the right side.

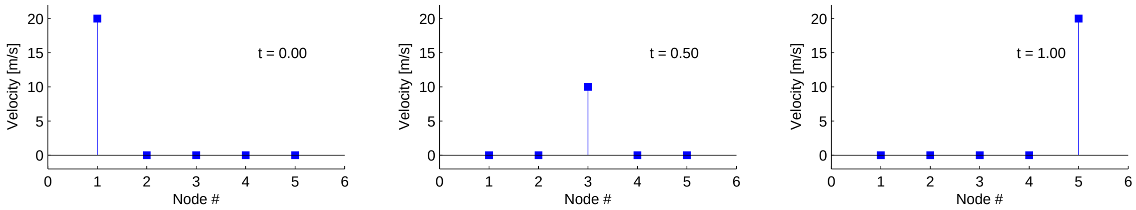

Figure 9-6: Three time steps of the IRF of a conservative sample bar.

It can be seen that the velocity of the outer nodes is 20 [m/s] when the impulse arrives and 10 [m/s] for the inner nodes. To couple to an identical bar, similar to the situation shown in figure 9-2, boolean matrix

$$\mathbf{B} = \begin{bmatrix} 0 & 0 & 0 & 0 & -1 & 1 & 0 & 0 & 0 & 0 \end{bmatrix} \tag{9-2}$$

is used. The system gets excited by a unit impulse on the left node of the left subsystem which is simulated by choosing

$$\mathbf{f}_0 = \begin{bmatrix} \frac{2}{\Delta t} & 0 & 0 & 0 & 0 & 0 & 0 & 0 & 0 & 0 \end{bmatrix}^T \tag{9-3}$$

Similar to figure 9-2b, at time $t = 1.00$ the incompatibility occurs. In this example node 5 now has a value of 10 [m/s], while node 6 has a value of 0 [m/s]. Now using equation (8-22)

$$\boldsymbol{\lambda}_n = \frac{2\left(\mathbf{B}\,\mathbf{H}_0\,\mathbf{B}^T\right)^{-1}\mathbf{B}\,\tilde{\mathbf{u}}_n}{\Delta t}$$

the required Lagrange multiplier can be calculated. Filling in; the incompatibility term is $\mathbf{B}\,\tilde{\mathbf{u}}_n = -20$ [m/s], the combined driving point interface admittance at $t = 0$ is $\mathbf{B}\,\mathbf{H}_0\,\mathbf{B}^T = 40$ [m/Ns^2] and the time step is $\Delta t = 0.25$. Filling in this yields $\boldsymbol{\lambda}_4 = -4$ [N].

Now when filling in equation (8-18)

$$\mathbf{u}_n = \mathbf{H}_n \left(\mathbf{f}_0 - \mathbf{B}^T \boldsymbol{\lambda}_0\right) \frac{\Delta t}{2} + \left(\sum_{i=1}^{n-1} \mathbf{H}_{n-i} \left(\mathbf{f}_i - \mathbf{B}^T \boldsymbol{\lambda}_i\right) \Delta t\right) + \mathbf{H}_0 \left(\mathbf{f}_n - \mathbf{B}^T \boldsymbol{\lambda}_n\right) \frac{\Delta t}{2}$$

it is seen that this yields an equal velocity at node 5 and 6 of 10 [m/s], as expected. When filling in for the next time step, time step 5 at $t = 1.25$ that the wave propagates to node 7 with 10 [m/s], as expected.

9-3-2 Example: Unstable coupling

This example is intended to demonstrate the influence of $\mathbf{H}_0$ in the stability of the coupling procedure. Compared to the IRF discussed in the example above, and partially shown in figure 9-6, the amplitude at time step 0, is reduced with 80%, from 20 to 16 [m/s], as seen in figure 9-7a. Note that the rest of the IRF remain the same. Again, since the structure is symmetrical, the same is done for the IRF caused by an impulse on the right.

Now when applying the same excitation and coupling operation as in the previous example, an incompatibility arises again at the fourth time step, i.e. $t = 1.00$, as is seen in figure 9-7b. Since the IRF at this time step is unaltered, the incompatibility is still $\mathbf{B}\,\tilde{\mathbf{u}}_n = -20$ [m/s]. The next step is to calculate the Lagrange multiplier, using equation (8-22) as done previously. This time however, the combined driving point interface admittance at $t = 0$ is $\mathbf{B}\,\mathbf{H}_0\,\mathbf{B}^T = 32$ [m/Ns^2], rather than 40 [m/Ns^2] as in the previous example. As a result the Lagrange multiplier is elevated by 25%; $\boldsymbol{\lambda}_4 = -5$ [N]. However, this does not alter its contribution as shown in figure 9-7c. Therefore after coupling, the wave still propagates at the interface, as expected, with 10 [m/s], as shown in figure 9-7d.

Up to now, everything seems fine. Investigating the contribution of the Lagrange multiplier, the effect its elevated is compensated for by the lowered value for $\mathbf{H}_0$. During the next time step however, the effects will show. At time step 5, $t = 1.25$, the original contribution $\mathbf{f}_0$ and the Lagrange multiplier from the previous time step $\boldsymbol{\lambda}_4$ contribute to the response. The contribution of the original excitation, seen in figure 9-8a, is as expected the impulse of 10 [m/s] which has reflected on the interface. Previously, the contribution of the Lagrange multiplier cancelled this out. When investigating the contribution of the Lagrange multiplier, seen in figure 9-8b, it is found that the amplitudes are to high, namely 12.5 [m/s]. As a result, the combined response, figure 9-8c, shows an elevated amplitude for the propagating wave at node 7 and a residual reflection at node 4, i.e. energy is added to the system.

9-4 Coupling of different materials

When coupling materials with different properties, reflections can occur on the interface as well. However, this is not to be confused with incomplete coupling. The coupling is full, the reflections are caused by the different material properties and the reflections would have been obtained when using a model of those structures combined without using substructuring techniques.

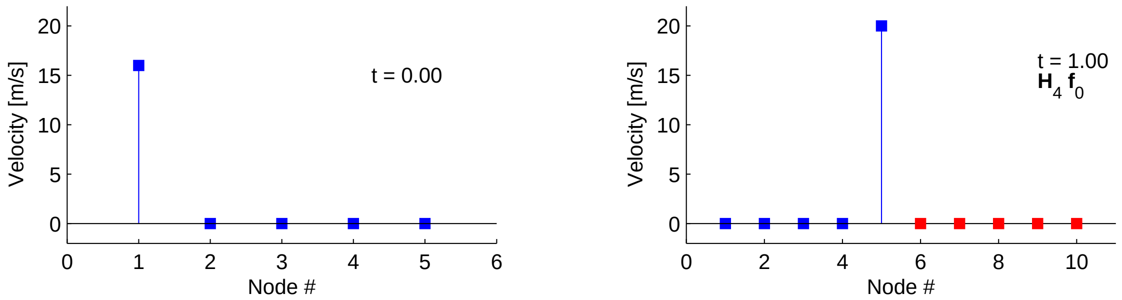

(a) The original value for $\mathbf{H}_0$ reduced to 80%.

(b) Incompatibility at the interface, with a higher amplitude as during $t = 0$.

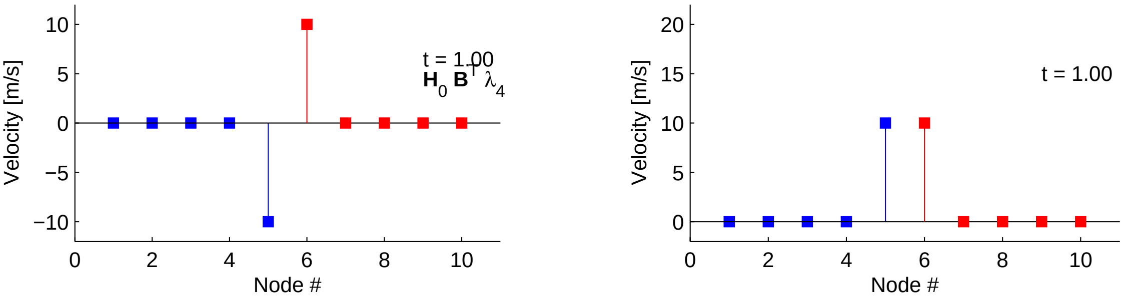

(c) The contribution of the elevated Lagrange multiplier, given by $-\mathbf{H}_0\,\mathbf{B}^T\,\boldsymbol{\lambda}_4\,\frac{\Delta t}{2}$.

(d) The combined response.

Figure 9-7: Coupling with an altered value for $\mathbf{H}_0$ at $t = 1.00$.

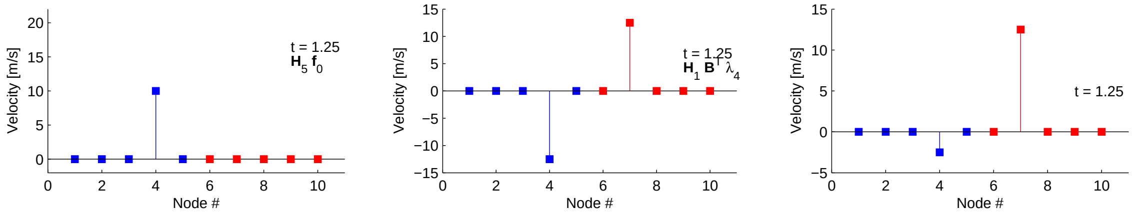

(a) Contribution of the original excitation.

(b) Contribution of the elevated Lagrange multiplier.

(c) The combined response.

Figure 9-8: The effect of unstable coupling visualised.

It might be interesting to discuss what phenomena can occur in this particular case. Section 3-3-1 has briefly discussed that the wave propagation speed in a material is given by its Young's modulus and density, i.e. $c = \sqrt{\frac{E}{\rho}}$. It is however possible that the amount of energy needed for a certain amplitude differs per material, while the wave propagation speed is equal, this happens for instance when both the Young's modulus and density of the material are scaled with the same factor.

In general four statements can be made when transferring a wave from one material (the transmitting material) to the next material (receiver material).

1. When the wave propagation speed of the receiver is lower than the the transmitter, a negative wave will reflect from the interface. This can be interpreted as if the structures movement gets constrained a little at the interface and therefore has to travel back a little.

2. When the wave propagation speed of the receiver is higher than the the transmitter, a positive wave will reflect from the interface. This can be interpreted as if the transmitter experiences too little resistance and tends to respond as if the interface was free. The interface can move a little further and takes the rest of the structure along using this wave.

3. When at the same wave propagation speed, the receiver requires less energy for the same amplitude, a positive wave will reflect from the interface. This can again be interpreted as if the transmitter experiences too little resistance and tends to respond as if the interface was free. The interface can move a little further and takes the rest of the structure along using this wave.

4. When at the same wave propagation speed, the receiver requires more energy for the same amplitude, a negative wave will reflect from the interface. This can again be interpreted as if the structures movement gets constrained a little at the interface and therefore has to travel back a little.

Note that these four statements apply to a wave of infinitesimal width. Imagine when a cosine shaped wave, as for example the result of the impulse depicted in figure 4-6a, reaches the interface. The propagating wave will broaden or narrow depending on the new wave speed. Together with the reflecting wave this illustrates how the energy is divided over the two waves after reaching the interface.

9-5 In summary: IRF requirements for successful coupling

In order to prevent unwanted behaviour when coupling experimentally obtained IRFs, there are a few conditions an IRF should satisfy. Those criteria are discussed in this section.

9-5-1 Stable coupling

Considering the first peak of cross-point IRF. There has to exist a peak earlier in the driving-point IRF of higher amplitude in order for the coupling procedure to be stable. For velocity IRFs this has been demonstrated in section 9-3 but this also holds for displacement IRFs.

In a more general sense one can say that an IRF has to be causal. After applying the impulse, the amount of energy[3] present in the system has to decay on the time interval that a wave requires to travel from the point of excitation to the point of coupling. When a travelling wave accumulates energy after it has been induced, the amount of energy contained in the wave being transferred from one substructure to the next by the interface force increases.

---

[3] The total of kinetic and potential energy.

When this happens more times sequentially the amount of energy and thus the responses of the system go eventually to infinity. From a matrix point of view this happens when values for the wave in the cross-point IRF are higher than values earlier in the driving point IRF. From a frequency domain perspective this is analogue to the fact that a dynamic stiffness matrix has to be positive definite for every frequency.

9-5-2 Complete coupling

In order to prevent incomplete coupling, the Courant number should be chosen equal to or lower than 1. This ensures that all information contained in a wave shows up at the interface node before it reflects. When a (part of) a wave does not show up at the interface due to a high Courant number, the (part of the) wave will have reflected on the interface before it could be propagated to the next substructure, resulting in incomplete coupling.

Section 9-2 has shown that for a linear bar, there has to exist a force loading at one end that is able to cancel out the travelling wave induced at the other end. For a wave that broadens and lowers in amplitude as it propagates, this means that the counter wave induced by the force loading has to be able to result in the same broadening and lowering. When decomposing the travelling wave into modes, this criterion can be simplified to stating that every mode requires to decay exponentially, such that all modes can be cancelled out accordingly.

9-5-3 Unit step tests

There are other test one can think of, namely unit step tests. These test do not necessarily relate to stability or completeness, but can serve as an additional check of the IRF. When applying a unit step force to the velocity IRF, this should yield the displacement IRF. This is due to the fact that

$$u(t) = \int_0^t \dot{u}(\tau)\,\mathrm{d}\tau \tag{9-4}$$

for a system initially at rest. One can argue that applying a unit step force to the acceleration has to result in the velocity IRF. This is however only true when the acceleration IRF is able to describe the acceleration required to obtain the initial velocity in the first place, as was extensively discussed in chapter 4.

When applying a unit step to the displacement IRFs, the response should converge to responses found in the corresponding column of the systems static admittance matrix, given that it exists.[4]

Figure 9-9: Bar model with a DoF on each end.

9-5-4 Example: Causality criterion demonstrated by inverse IRF filter on two DoF bar model

Consider the bar with two DoFs given in figure 9-9. Again, only velocities are considered. Assuming the bar is fully symmetric, its response can be obtained by:

$$\begin{bmatrix}\dot{u}_1(t)\\ \dot{u}_2(t)\end{bmatrix} = \begin{bmatrix}h_{dr}(t) & h_{cr}(t)\\ h_{cr}(t) & h_{dr}(t)\end{bmatrix} * \begin{bmatrix}f_1(t)\\ f_2(t)\end{bmatrix} \tag{9-5}$$

Formally the IRFs are velocity IRFs, but for the sake of simplicity the dot indicating the first derivative in time is omitted. It is assumed the bar behaves analogue to the behaviour the bar of the example in section 9-1. An impulse at one end travels to the other end in T seconds. Besides that an exponential decay is active on the impulse with a time factor of τ seconds. The shape of the travelling pulse is maintained; a Dirac shape. This yields the following driving point and cross point IRFs:

$$h_{dr}(t) = \delta(t) + \delta(t-2T)\,e^{-\frac{2T}{\tau}} + \delta(t-4T)\,e^{-\frac{4T}{\tau}} + \cdots + \delta(t-(2n)T)\,e^{-\frac{(2n)T}{\tau}} \tag{9-6a}$$

$$h_{cr}(t) = \delta(t-T)\,e^{-\frac{T}{\tau}} + \delta(t-3T)\,e^{-\frac{3T}{\tau}} + \delta(t-5T)\,e^{-\frac{5T}{\tau}} + \cdots + \delta(t-(2n+1)T)\,e^{-\frac{(2n+1)T}{\tau}} \tag{9-6b}$$

Now when looking for the force to be applied on node 2, to cancel out the travelling wave initiated by an impulse (Dirac force) given on node 1, equation (9-5) rewrites to:

$$\begin{bmatrix}\delta(t)\\ 0\end{bmatrix} = \begin{bmatrix}h_{dr}(t) & h_{cr}(t)\\ h_{cr}(t) & h_{dr}(t)\end{bmatrix} * \begin{bmatrix}\delta(t)\\ f_2(t)\end{bmatrix} \tag{9-7}$$

At first sight it can be seen that the solution to this system of equations for $f_2(t)$ is given by

$$f_2(t) = -\delta(t-T)\,e^{-\frac{T}{\tau}} \tag{9-8}$$

However, during this example this will be derived using the inverse IRF filter method. Rewriting the second line of the system of equations yields:

$$h_{dr} * f_2(t) = -h_{cr} * \delta(t) \tag{9-9}$$

Note that convolving with a Dirac function $\delta(t)$ yields the function itself and convolving a function with its inverse yields the Dirac function. So convolving both sides of the equation with h_{dr}^{inv} gives an expression for $f_2(t)$:

$$f_2(t) = -h_{dr}^{inv} * h_{cr} \tag{9-10}$$

---

[4] The static admittance matrix is the inverse matrix of the stiffness matrix. When the system has a rigid body mode, the stiffness matrix has a null space which means that a static response does not exist.

Now examining $h_{dr}(t)$, it can be seen that the combination $h_{dr}(t) - h_{dr}(t-2T)\, e^{-\frac{2T}{\tau}}$ would yield the dirac function again. This means that the inverse IRF filter for $h_{dr}(t)$ becomes:

$$h_{dr}^{inv} = \delta(t) - \delta(t-2T)\, e^{-\frac{2T}{\tau}} \tag{9-11}$$

Now substitution in (9-10) shows that this indeed yields the expected result as given in equation (9-8). For the purpose of verification, it can be seen that for the chosen $f_2(t)$, the first line of the system of equations is also true.

Remarks

Three remarks are to be made here

- This 2 DoF system is rather simple. However, more nodes can be added in between. As long as the velocity vector $\dot{\mathbf{u}}(t)$ describes only the initial pulse travelling from one end to the other between time $0 \leq t < T$ and the proper IRFs are incorporated, the result stays the same.
- When the number of nodes approaches infinity, the velocity field becomes continuous $\dot{u}(x,t)$ and the travelling pulse might be better describable by the wave equation, as was also discussed in section 4-4. One can imagine this system of equation would then yield a combination of two travelling waves for time $t \geq T$ cancelling each other out.
- One could argue whether the velocity for $\dot{u}_2(t)$ shouldn't show a delayed Dirac function $\delta(t-T)$. It is assumed that upon applying an impulse, the Dirac shows at that same instance as velocity on the node. Since the time for the pulse to cross the bar is assumed to be T seconds, it will show at every location of the bar, except for the actual end during times $0 \leq t < T$. At time $t = T$ itself, the pulse has reached the actual end, but is already cancelled out by the Dirac applied at this time. In summary this means that the pulse will never actually show on the DoF $\dot{u}_2(t)$.

Chapter 10

Practical studies

This chapter discusses the two practical studies performed on coupling two 50 element linear bar models. First the different coupling methods are tested on this substructuring problem. During the second case, this problem is subjected to an attempt to couple using the inverse IRF filter of acceleration IRFs.

10-1 Two 50 element linear bar models coupled

This case study concerns the coupling of two 50 element linear bar models as was used as case study in chapter 6. The bars will be coupled sequential as shown in figure 10-1 using the inverse IRF filter method, discussed in section 8-4 and the classical discrete time domain approach, discussed in section 8-3.

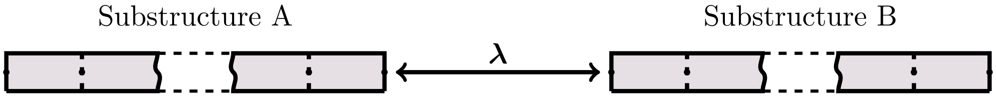

Figure 10-1: Coupling two 50 element linear bar models.

Similar as in chapter 6, the IRFs of the structure are built using MSP. The highest frequency present is $2.58\,10^{-5}\,[rad/s]$. Choosing a Courant's number of 0.5, this yields time steps of $\Delta t = 3.88\,10^{-6}\,[s]$. Again a total time of $10\,[ms]$ is taken into account. Again velocity IRFs and responses are considered.

During both coupling methods an attempt is done to solve

$$\begin{cases} \dot{\mathbf{u}}(t) = \int_0^t \dot{\mathbf{H}}(t-\tau)\,\Big(\mathbf{f}(\tau) - \mathbf{B}^T\boldsymbol{\lambda}(\tau)\Big)\,\mathrm{d}\tau \\ \mathbf{B}\,\dot{\mathbf{u}}(t) = \mathbf{0} \end{cases}$$

For this case study the IRFs of the substructures are incorporated as follows:

$$\dot{\mathbf{H}}(t) \triangleq \begin{bmatrix} \dot{\mathbf{H}}^{\mathrm{A}}(t) & \mathbf{0} \\ \mathbf{0} & \dot{\mathbf{H}}^{\mathrm{B}}(t) \end{bmatrix}$$

This renders the velocity vector $\dot{\mathbf{u}}$ and force vector $\mathbf{f}$ as follows:

$$\dot{\mathbf{u}}(t) \triangleq \begin{bmatrix} \dot{u}_1^{\mathrm{A}}(t) \\ \vdots \\ \dot{u}_{51}^{\mathrm{A}}(t) \\ \dot{u}_1^{\mathrm{B}}(t) \\ \vdots \\ \dot{u}_{51}^{\mathrm{B}}(t) \end{bmatrix} \qquad \mathbf{f}(t) \triangleq \begin{bmatrix} f_1^{\mathrm{A}}(t) \\ \vdots \\ f_{51}^{\mathrm{A}}(t) \\ f_1^{\mathrm{B}}(t) \\ \vdots \\ f_{51}^{\mathrm{B}}(t) \end{bmatrix}$$

In order to couple, boolean matrix $\mathbf{B}$ is chosen such that

$$\mathbf{B}\,\dot{\mathbf{u}}(t) = \dot{u}_1^{\mathrm{B}}(t) - \dot{u}_{51}^{\mathrm{A}}(t) = 0 \tag{10-1}$$

10-1-1 Coupling using true IRFs

First, the 'true' IRFs obtained by MSP are used. An attempt is done to obtain the driving point IRF of the first node of the coupled structure. Therefore the applied load is defined as

$$\mathbf{f}(t) = \begin{bmatrix} f_1^{\mathrm{A}}(t) \\ 0 \\ 0 \\ \vdots \\ 0 \end{bmatrix} \qquad \text{with} \qquad f_1^{\mathrm{A}}(t) = \begin{cases} \frac{2}{\Delta t} & \text{for} \quad t = t_0 \\ 0 & \text{for} \quad t \neq t_0 \end{cases} \tag{10-2}$$

Three solutions are discussed. The solution for the classical discrete time domain approach and two solutions for the inverse IRF filter. As discussed in section 8-4, the obtained filter can contain some non-causal information as well. Therefore a causal solution is considered, referred to as the inverse IRF method and a non-causal solution is considered, taking into account information from before $t = 0$, which is referred to as the full inverse IRF solution. For the purpose of reference, a bar with twice the length of the original bar consisting of 100 elements is modelled. Its IRF is obtained by MSP.

Consider figure 10-2, giving the obtained solutions for the different substructuring approaches. All methods yield an initial velocity of $101\,[m/s]$ which is not shown due to cropping of the graph. After the initial velocity, various differences are observed.

First consider the reference solution. It is seen that the wave returns after roughly $2.7\,[ms]$ which is twice the amount of time as was the case with the original bar as was seen in chapter 6, figure 6-2b. The generated wave now has to travel twice the distance so this is intuitive. Now consider the classical discrete solution. Its response almost overlaps the reference solution, rendering it a good match. In between the wave passing by a little velocity is observable

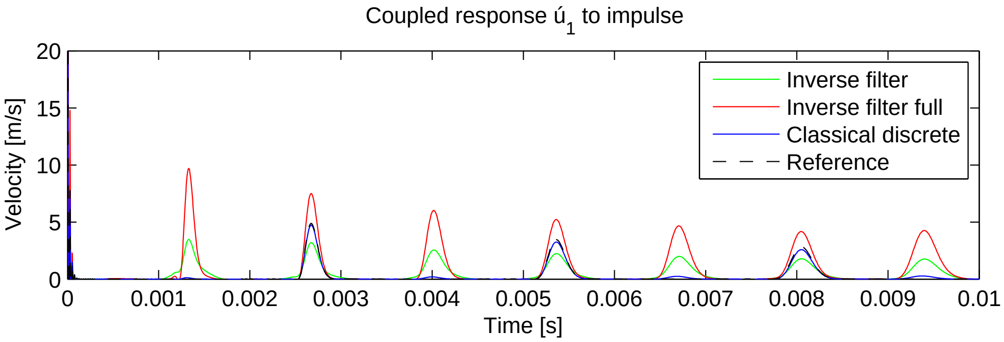

Figure 10-2: Driving point IRF of the coupled structure

which indicates a small reflection of the wave on the interface, as is also discussed in section 9.

Finally, consider the solutions obtained using the inverse IRF filter. First it can be seen that both do not approximate the amplitude of the wave accurately at the moments the wave is actually there. The inverse filter solution underestimates its amplitude, while the full inverse filter solution overestimates the amplitude of the wave. Secondly at the moments where the IRF of the substructure[1] showed the wave passing, but where it should have propagated to the other end of substructure B in the coupled system, these solutions still show the wave as if it reflected on the interface.

In order to understand why the solutions obtained using the inverse filter make such a poor approximation, (by means of reverse engineering) the calculated interfaces of those solutions and the interface force calculated by the classical discrete algorithm can be compared. Figure 10-3 shows the calculated interface force. It is seen that when the wave first arrives at the interface, after roughly 6.6 $[ms]$ the interface force calculated using the inverse filter deviates significantly from the interface force calculated with the classical discrete method, which has proven to have made a decent approximation. Next, the second and third time the wave is expected to pass this interface, again a significant underestimation of the interface force is made. Later in the time, the interface force calculated with the inverse filter seem to have completely 'damped out.'

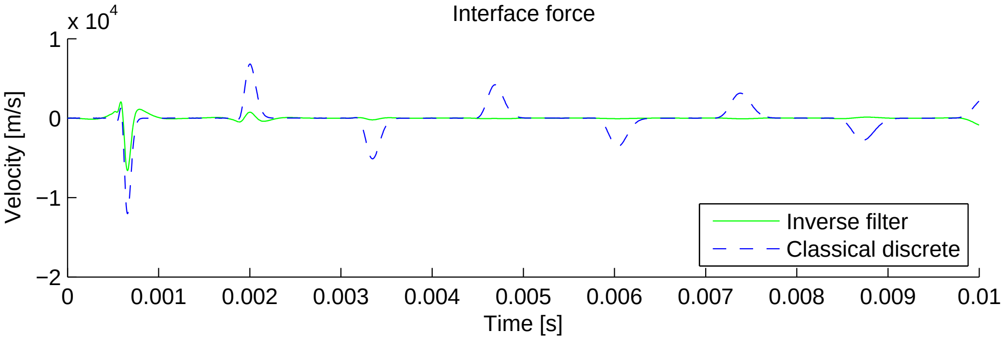

Figure 10-3: Interface force between the substructures

---

[1] Chapter 6, figure 6-2b.

The influence of taking the full time interval presented by the inverse filter approach can be investigated. Figure 10-4 depicts the filter over the obtained time domain. The interface forces are expected to equal zero before applying the impulse, since the system is at rest, figure 10-4 shows differently though for the inverse filter approach. So this explains the difference in the solution between the inverse IRF approach and the full inverse IRF approach. But this does not explain why these interface forces do not match the expected interface force.

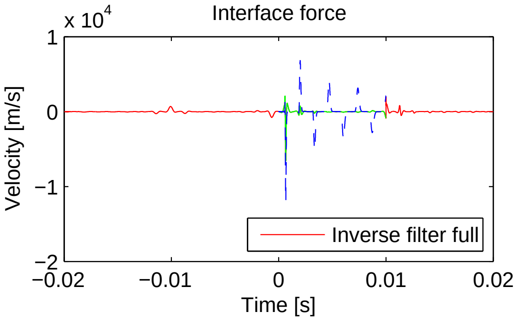

Figure 10-4: Interface force between the substructures including for the time interval presented by the inverse filter calculation.

Now recall equation (8-36):

$$h_{BB}(t) * \lambda(t) = \mathbf{BH}(t) * \mathbf{f}(t)$$

The inverse IRF filter was designed such that the interface gap that would have been caused when the structure was uncoupled $\mathbf{BH}(t) * \mathbf{f}(t)$, gets compensated for by the combined interface IRF convolved with the interface forces $h_{BB}(t) * \lambda(t)$. Both are depicted in figure 10-5. The figure shows that the full inverse filter approach yields quite an accurate approximation compared to actual gap that would have been caused by the uncoupled system. Only the first peak shows a significant difference in amplitude. The inverse filter using only the causal part of the filter yields a slightly worse approximation which can be assigned to the disregarding of information.

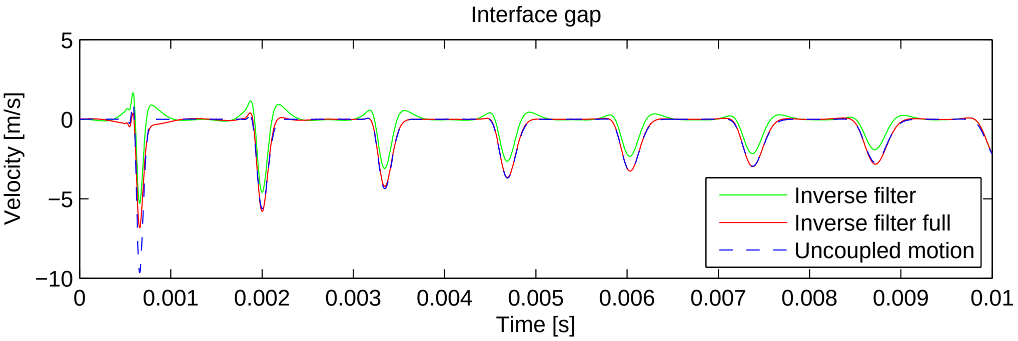

Figure 10-5: The interface gap for the uncoupled system and the compensation calculated by the inverse IRF filter approach.

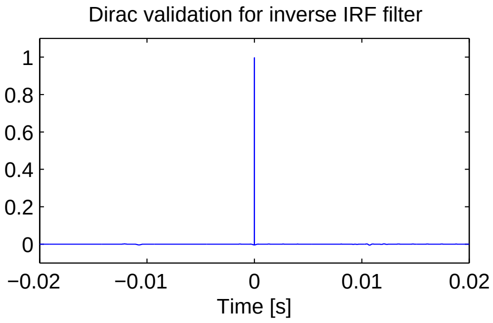

Figure 10-6: Verification of $h_{BB}^{inv}(t) * h_{BB}(t) = \delta(t)$.

Still the inverse IRF filter was designed to give a 'perfect' match for these gaps, recall (8-37b):

$$\lambda(t) = h_{BB}^{inv}(t) * \mathbf{BH}(t) * \mathbf{f}(t)$$

Which is only true if

$$h_{BB}^{inv}(t) * h_{BB}(t) = \delta(t)$$

which is verified in figure 10-6. It is seen that convolution of both yields the Dirac function. Closer examination of the results shows that error made on time steps other than $t = 0$ is not larger than 0.5%, although this is not clearly visible in the graph.

Compatibility Verification

Early in chapter 2 it is explained that substructuring requires satisfaction of two conditions; compatibility and equilibrium. In all substructuring algorithms introduced in chapter 8 equilibrium is satisfied by using $\boldsymbol{\lambda}$ as intreface forces as it has been defined in (2-2b). But is the compatibility condition (2-2a) also automatically satisfied?

The classical discrete method attempts to satisfy compatibility explicit at every time step by choosing the Lagrange multiplier $\boldsymbol{\lambda}$ accordingly. For the inverse IRF filter method, this is not the case. The interface forces are calculated on forehand based on only the uncoupled motion, as is discussed above. The effect this has on the compatibility is shown in figure 10-7.

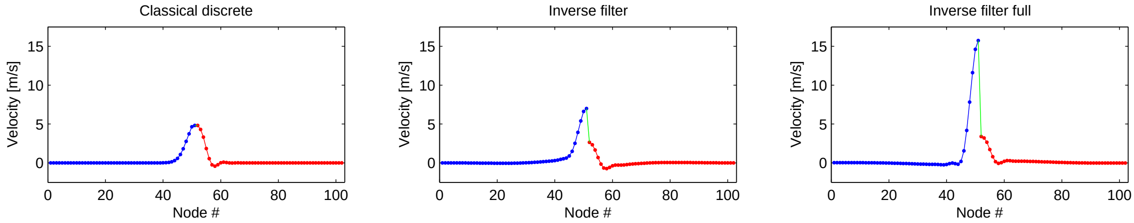

(a) The classical discrete approach **(b)** The inverse IRF filter approach **(c)** The inverse IRF filter approach using the full time domain available

Figure 10-7: Visualisation of the coupled structure at $t = 0.66\,[ms]$, when the wave transits from substructre A to substructure B.

The figure shows the first transition of the wave from substructure A to substructure B. As expected, figure 10-7a shows a compatible situation for the classical discrete method. The two inverse IRF filter methods however, shown in 10-7b and 10-7c show a significant incompatibility on the interface. For the inverse filter method in figure 10-7b, it looks like not enough interface force has been present, giving an overestimation of the amplitudes on substructure A and a underestimation of similar order of the amplitudes on substructure B. The inveres IRF filter approach using the full available time domain, shown in figure 10-7b has even worse compatibility. The amplitudes on substructure B are similar to those using the regular inverse IRF filter approach. The amplitudes on substructure A however, are highly overestimated.

Modal content

Section 8-3-1 discussed that interaction between modes occurs due to the coupling. When examining the modal content of the coupled structure using the classical discrete method, by projecting the response of the coupled system on the modes of the substructures, some interesting effects are observable. See figure 10-8.

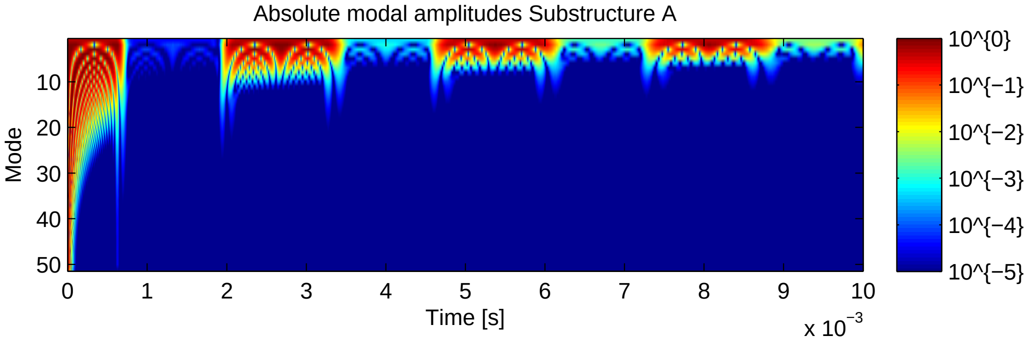

(a) Substructure A

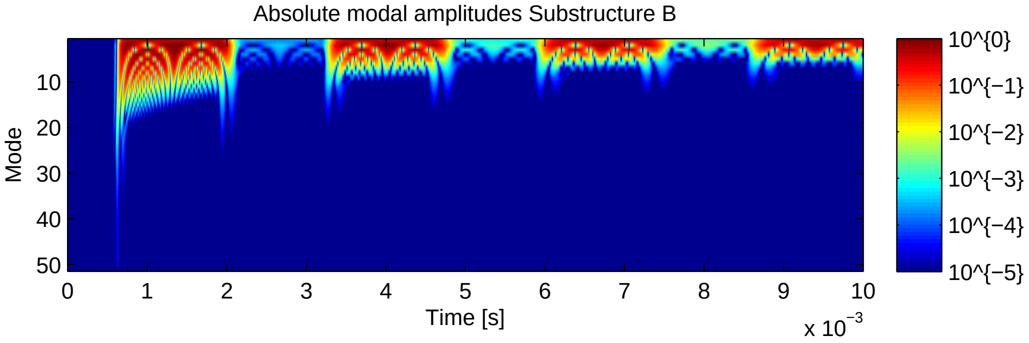

(b) Substructure B

Figure 10-8: Modal amplitudes over time for the travelling wave trough the structure, for the modes of the substructures.

When applying the initial impact on substructure A, the modal content, shown in figure 10-8a, is equal to the modal content of the single bar, as was shown in section **??**, figure 6-4. When the wave reaches the interface, some of the higher frequent content that was actually damped out, becomes visible again until the wave transferred to substructure B. While the wave travels back and forth in substructure B, some minor activity is visible in substructure A, but at this moment this is still negligible. As time proceeds, three things can be noted from the graphs:

- First, it is seen that when the wave transits from one substructure to another that the modal amplitudes deviate from their damping oscillating behaviour. This is explained in chapter 6.

- Secondly, more overlap seems to be visible between the modal amplitudes of the two substructures as time proceeds. This can be assigned to the fact that the wave broadens due to faster damping of the higher modes and during the transit from one substructure to another, modal content of both substructures is required.
- Finally, as time proceeds the modal amplitudes present in the substructures, while the wave is in the other substructure increases. This is expected to be the result of minor reflection at the interface.

Energetic content

For the purpose of comparison with the situation where imperfect IRFs are used, it is useful to review the energetic content of the substructures, depicted in figure 10-9.

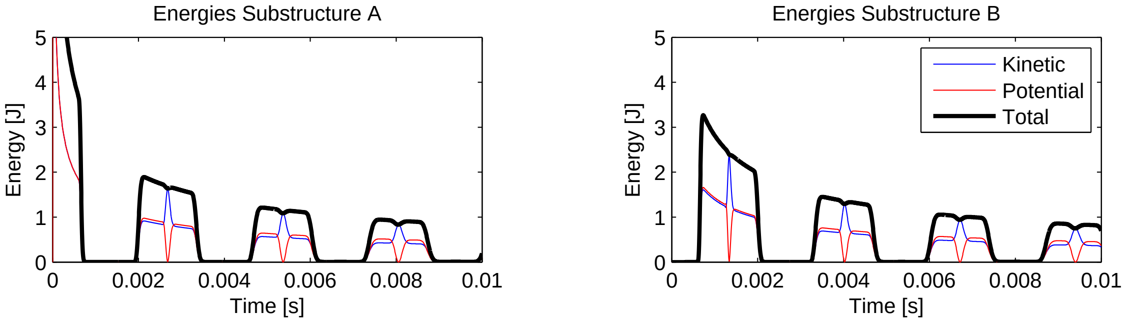

(a) Energies in substructure A. Note that the graph has been cropped on the Energy axis. The initial total energy of the substructure is $50\,[J]$.

(b) Energies in substrucure B.

Figure 10-9: Kinetic, potential and the total energy present in the two substructures.

It is clearly seen that the energy present in the substructures transfers from one substructure to another as the travelling wave does. Besides that, it can be seen that the total amount of energy shows decaying behaviour as would be expected.

10-1-2 Coupling using imperfect IRFs

Next, the same thing is done using IRFs obtained by an imperfect impulse. The IRFs used are the same IRFs obtained in section 6-2. The applied load is the same load as described by (10-2). Again, an attempt is done to obtain the driving point IRF for the coupled structure using three methods. The classical discrete time domain method approach is used and again two approaches using the inverse IRF filter, the solution using only the part of the filter where $t \geq 0$, referred to as inverse IRF filter and the full filter using also information from $t < 0$, referred to as the full inverse IRF filter. For the purpose of reference, a bar with twice the length of the original bar is consisting of 100 elements is modelled and subjected to the same imperfect impulse.

The driving point IRF obtained by the different methods are found in figure 10-10. Considering the reference solution it can be seen that a wave formed velocity shows initially as a result of the applied imperfect impulse. After $0.9\,[ms]$ the velocity has reduced to $0\,[m/s]$. After roughly $2.6\,[ms]$ the travelling wave shows up again.

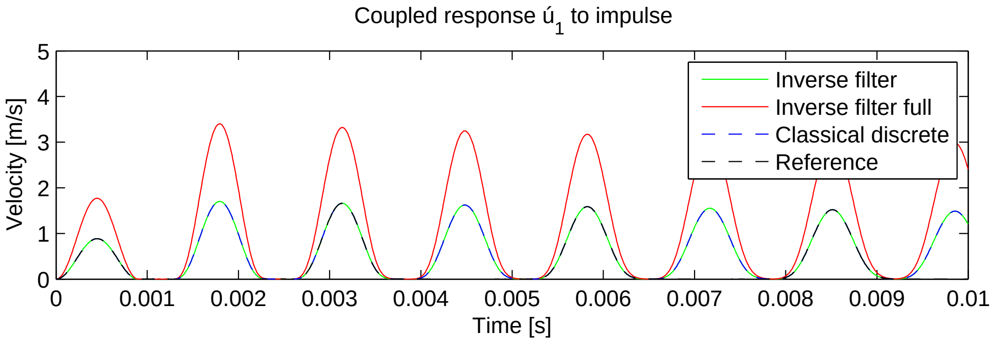

Figure 10-10: Driving point IRF of the coupled structure obtained using IRFs by imperfect impulses.

Now when considering the other three solutions, it appears that the travelling wave has reflected on the interface and appears again at the driving point. The difference in amplitude of the waves given by the three different solutions is significant. The classical discrete solution and the inverse filter solution give equal amplitudes as the reference solution, but occur twice as much. The amplitude of the solution using the full inverse filter is twice as high.

Let us now consider the cross-point IRF, from one end of the coupled structure, node 1, to the response at the other end, node 102. The results for the different methods are found in figure 10-11.

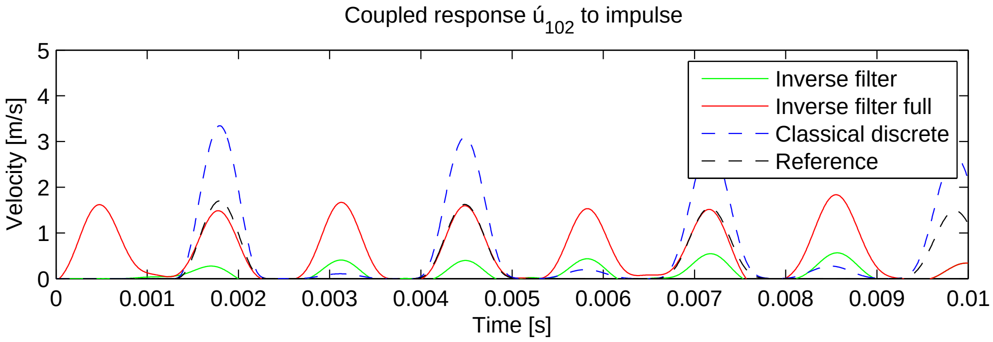

Figure 10-11: Cross-point IRFs for the coupled structure from end of the bar, node 1 to a response at the other end of the bar, ndoe 102.

The results differ a lot per method. The classical discrete method shows the travelling wave at the same moments as the reference solution does, only this time, unlike with the driving point IRF, the classical discrete method overestimates the travelling wave roughly by a factor two. The solution generated by the inverse filter tends to show the first arriving wave at the right time, but after that the wave in substructure B seems to be reflecting on the interface as well. Besides that the amplitudes are underestimated. Finally , the full inverse filter solution shows a response before the travelling wave would even been able to reach the end of the coupled structure. After that, it shows the same reflecting behaviour. The amplitude of the wave, does however match the amplitude of the reference solution.

Finally let us consider what occurs on the interface. The response of the last node of substructure A, node 51 and the response of the first node of substructure B, node 52, are depicted in figure 10-12.

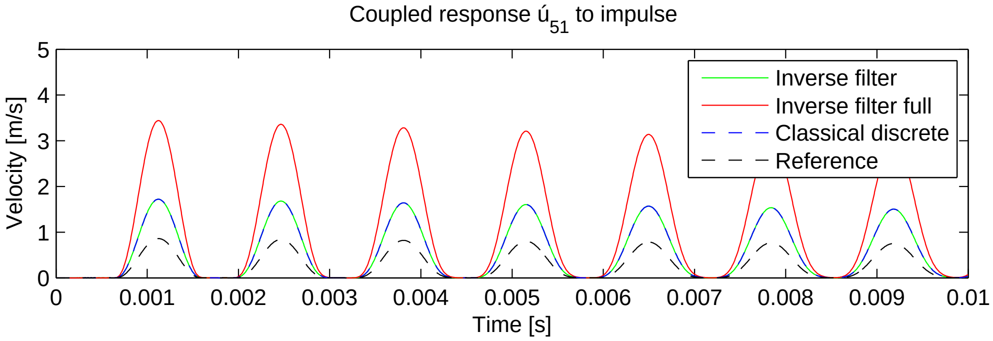

(a) Substructure A

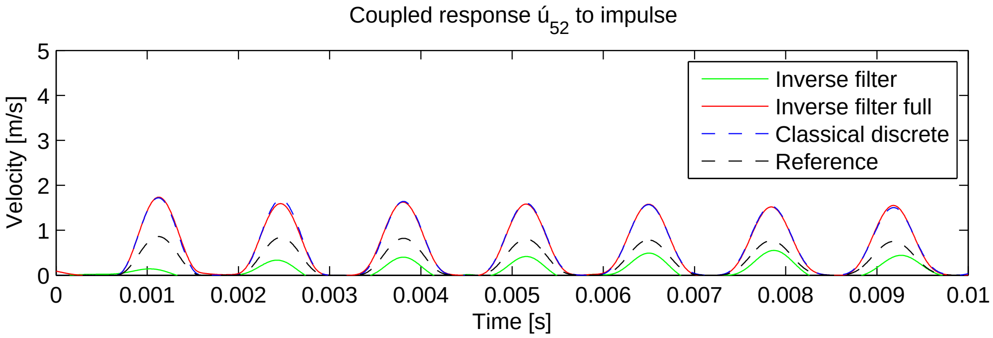

(b) Substructure B

Figure 10-12: The cross-point IRFs for the interface nodes of the coupled structure for an impulse at the other end of substructure A, node 1.

It is seen that in terms of timing, for all solutions, the travelling wave appears at and disappears from the interface at the same time as the reference solution. The difference is found in the amplitudes. At substructure A, the inverse filter solution equals the solution of the classical discrete method, while at substructure B the full inverse filter solution equals the solution of the classical discrete method. None of them however, equal the reference solution.

These different amplitudes imply compatibility violations. For all three methods, the moment that the peak of the induced wave transits from substructure A to substructure B is visualised, see figure 10-13. As seen before, both inverse filter solutions have yielded an incompatible situation. The classical discrete method yields a compatible situation, as is expected due to the nature of the method.

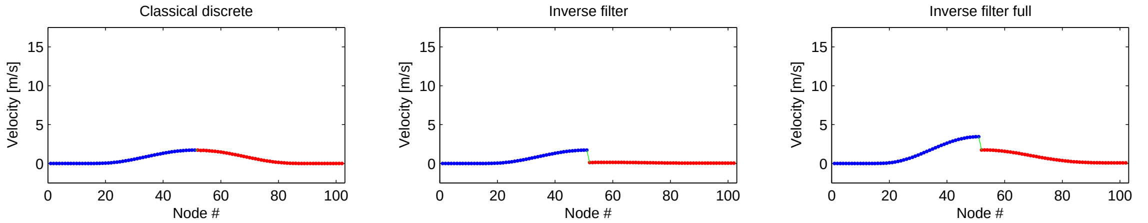

(a) The classical discrete approach **(b)** The inverse IRF filter approach **(c)** The inverse IRF filter approach using the full time domain available

Figure 10-13: Visualisation of the coupled structure at $t = 1.12\,[ms]$, when the peak of the wave transits from substructre A to substructure B.

Interface force and interface gap

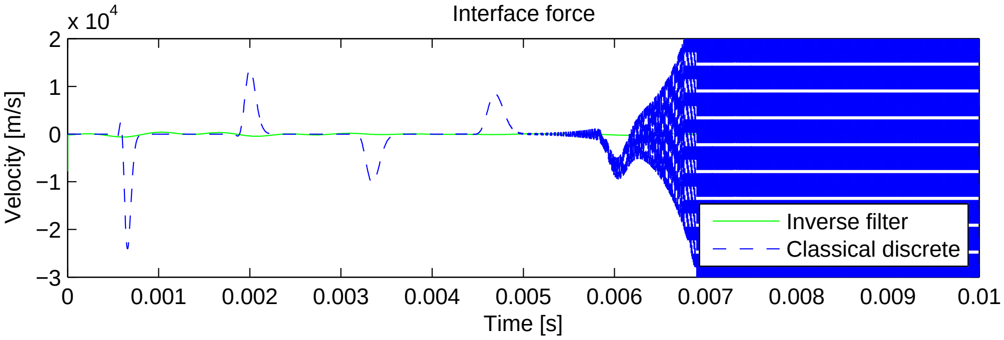

Figure 10-14: The interface force between the two substructures

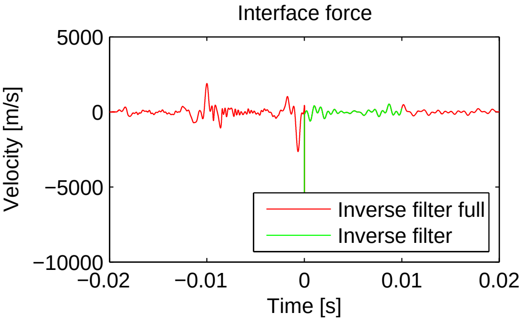

Figure 10-15: The interface force between the two substructures visualised over the full time domain presented by the full inverse IRF filter.

So despite the fact that none of the substructuring methods has yielded the correct answer, the inverse filter solutions also have shown compatibility violations. In order to find out what causes this compatibility violation, the interface forces are shown in figure 10-14. Two interesting things emerge. First it is seen that the inverse IRF filter has resulted in lower interface forces compared to the classical discrete method. This can explain the behaviour of the induced wave reflecting on the interface in substructure A and barely transitioning to substructure B. Secondly it is seen that the interface force calculated with the classical discrete method is unstable. This instability seems to occur in the higher frequency content of the interface force. Initially, up to $0.5\,[ms]$ the interface force consists mostly of lower frequency content, as expected. After this time, the increasing high frequency content becomes dominant. This unstable behaviour does not show yet on the response of the coupled structure. The used impulse to obtain the IRFs used here for coupling, contained too little content of this frequency, making this high-frequency contribution insignificant. This was also explained in section 4-3-1.

To see what difference is made by using the full inverse IRF filter, consider the interface force over the full time domain, show in figure 10-15. It is seen that interface force is applied before $t = 0$, rendering the full inverse IRF filter non-causal. To see what effect this has on the earlier discussed interface gap, consider figure 10-16. It is seen that the non-causal full inverse IRF filter is in fact able to compensate for the interface gap, which exists for $t \geq 0$.

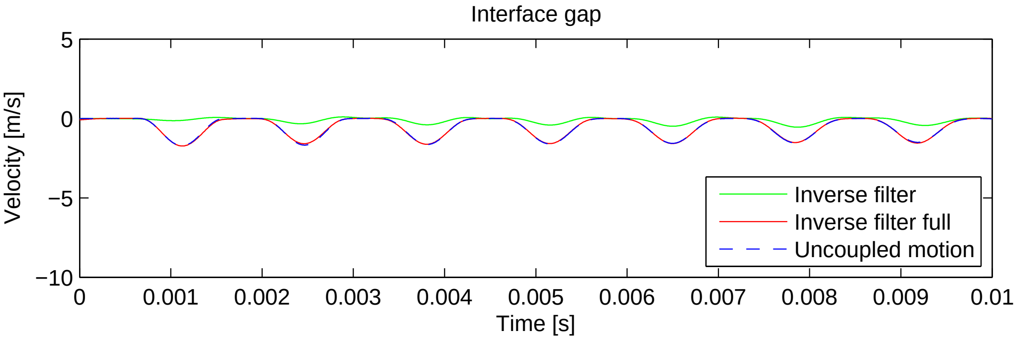

Figure 10-16: The interface gap for the uncoupled system and the compensation calculated by the inverse IRF filter approach.

The interface gap of the full inverse IRF filter explained

Above it is shown that when using the full inverse IRF filter, the interface gap that would be caused by uncoupled behaviour is exactly compensated for. In order to explain this, recall that the inverse filter has been designed to do so, recall (8-36):

$$h_{BB}(t) * \lambda(t) = \mathbf{BH}(t) * \mathbf{f}(t)$$

However, the free uncoupled motion $\mathbf{BH}(t) * \mathbf{f}(t)$ and the combined driving point interface IRF $h_{BB}(t)$ are only specified on time interval for $0 \leq t \leq 0.01\,[s]$. The full inverse IRF filter however, allows the interface force λ to be specified outside this interval. This allows λ to contain values other than zero before $t = 0$ rendering the filter and the interface force non-causal but still allows compensation of the interface gap on this limited time interval.

Energetic content

It was discussed in section 9-5 that the energy in a subsystem, described by its IRFs, has to decay in order to guarantee successful coupling. Since an imperfect impulse is used to obtain the IRFs used for coupling during this case study, this is definitely not the case.[2] Let us therefore discuss the energetic content of the coupled system for the solution given by the classical discrete method, as seen in figure 10-17.

---

[2] Also see section 4-3-1.

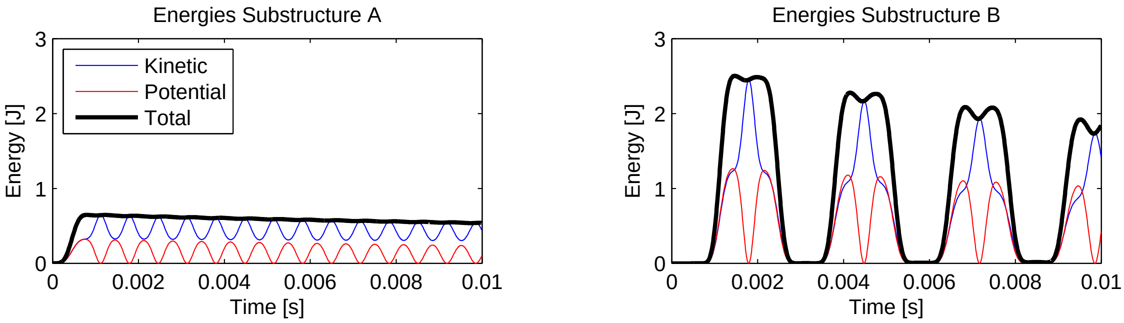

(a) Energies in substructure A.

(b) Energies in substrucure B.

Figure 10-17: Kinetic, potential and the total energy present in the two substructures for the results obtained by the classical discrete method.

It can be seen that after 1.3 $[ms]$, when the wave reaches the interface the energy in substructure B increases beyond the amount of energy conserved in substructure A. This is explained by the fact that every time step that interface force is applied, energy is added to the system, since this is described in the system of IRFs. The fact that the amount of energy in substructure A remains unaltered[3] can be explained due to the symmetry of this substructuring problem. The same explanation may go for the decrease in energy for substructure B after the received wave is back at the interface after roughly 3.7 $[ms]$. The reflecting wave in substructure A that first added energy to subsystem B has simultaneously returned at the interface and now the opposite thing happens where the wave in substructure B is cancelled out, reducing its amount of energy.

To see whether this is anything different for the results obtained by the inverse IRF filter method, consider figure 10-18. It is seen that prior to the impulse $(t < 0)$, substructure A does not contain energy. Substructure B however does posses some energy roughly 10 $[ms]$ before the impact is applied. This can be directly assigned to the non-causality of the inverse IRF filter. Furthermore the energetic content of substructure A shows the same behaviour as with the classical discrete method, only the amplitudes are overestimated. The energy content of substructure B seems to fluctuate as long as waves travel trough the substructure. There is no recognisable pattern in this content.

---

[3] Although decreasing

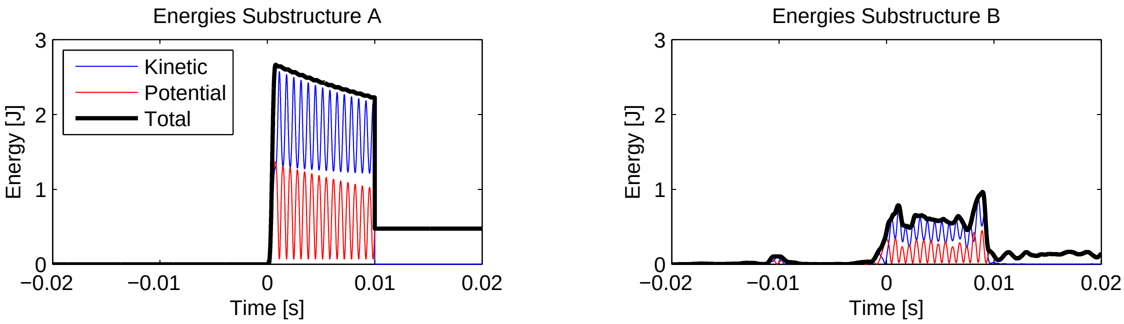

(a) Energies in substructure A.

(b) Energies in substrucure B.

Figure 10-18: Kinetic, potential and the total energy present in the two substructures for the results obtained by the full inverse IRF filter method.

10-2 Acceleration IRF Inverse filter

It has been discussed previously in chapter 4 that an acceleration IRF that captures the acceleration required to obtain the initial velocity of a structure, is suited to be used in the convolution integral. The acceleration IRF obtained by Newmark time intergration using the initial force condition satisfies this. Therefore, as discussed in section 8-5 that IRF should be suited for coupling as well.

Again consider the substructuring problem from the previous section, illustrated in figure 10-1. In this section an attempt is made to solve the problem using the inverse filter of the acceleration IRF. Figure 10-19 depicts the acceleration IRF of the driving point and the cross-point.

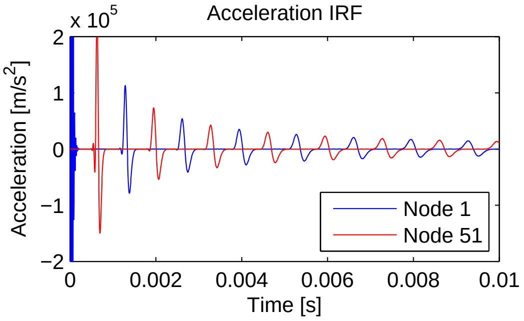

Figure 10-19: Driving point and cross-point acceleration IRFs for an impulse on node 1. Node that the figure has been cropped on the velocity axis. The initial acceleration for node 1 is $5.2\,10^7$ $[m/s^2]$

For the coupling the inverse filter of $h_{BB}(t) = \mathbf{B}\,\mathbf{H}(t)\,\mathbf{B}^T$ needs to be obtained. For this problem, due to symmetry, that equals two times the driving point IRF. Since the driving point IRF has its maximum value at $t = 0$, the inverse filter is expected to be causal.[4] Since the filter is expected to be causal, the filter will be used over the full time interval it describes. The filter is depicted in figure 10-20. In figure 10-20a it is clearly seen that the inverse IRF filter has a high peak at $t = 0$. When zooming on the inverse filter, figure 10-20b, transient behaviour is observed. Also, the filter has some oscillating content before $t = 0$ with an amplitude in the order of 10^{-9} $[Ns^2/m]$. This is possibly caused by the fact that the IRF is not fully damped out after the used $10\,[ms]$.

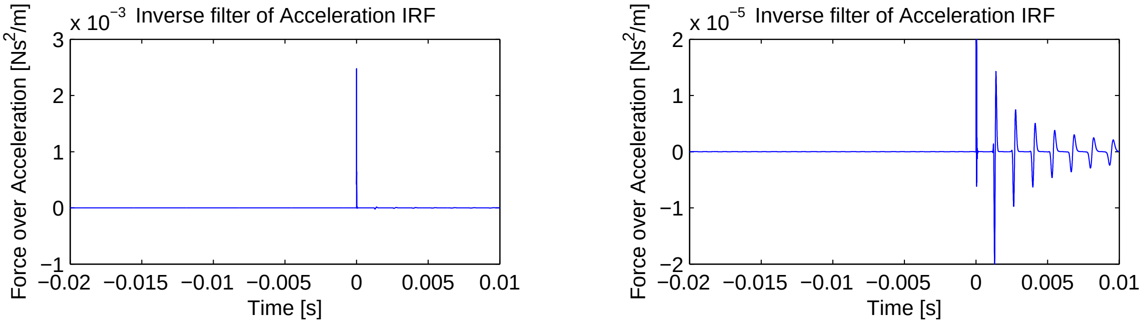

(a) The inverse IRF filter.

(b) The inverse IRF filter, zoomed in.

Figure 10-20: The inverse filter of $h_{BB}(t)$, describing accelerations.

---

[4] For more information on this the reader is referred to section 8-4.

Let us now examine the interface force which is the result of the inverse filter and the uncoupled motion, depicted in figure 10-21. It is seen that in fact no interface force are obtained for $t = 0$, which was expected. The first peak in interface force occurs at roughly $0.6\,[ms]$ when the travelling wave has reached the interface. From there on onward, the graph for the interface force nicely depicts the travelling wave passing by. This is promising for the results.

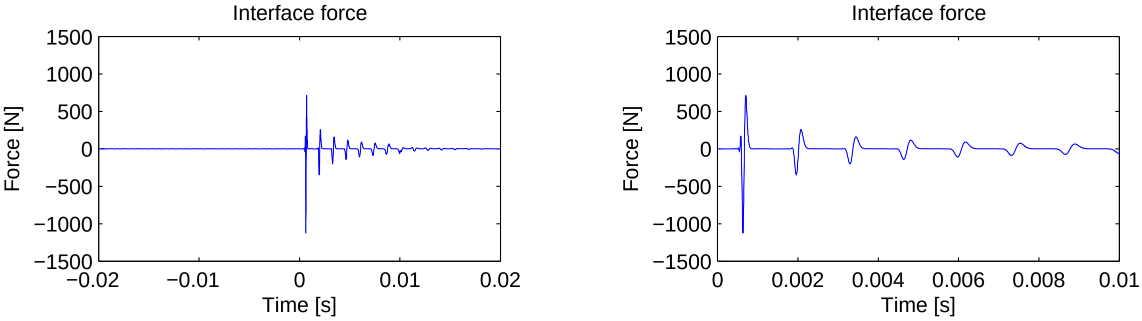

(a) The obtained interface force **(b)** The obtained interface force, zoomed in.

Figure 10-21: The interface force obtained by convolution of the uncoupled acceleration and the inverse IRF filter over time.

Let us then finally consider some of the coupled structure's responses and compare them to a reference solution.[5] The accelerations for the first and last nodes of both substructures are given in figure 10-22. Considering the driving point response, given in figure 10-22a it is seen that the coupled structure behaves as if it would still be uncoupled, which indicates that (the larger part of) the wave has reflected on the interface. When considering the other end of the coupled structure, seen in figure 10-22b, it is seen that the travelling wave arrives at same moment as for the reference solution, although it is much smaller in amplitude. After this wave seems to be reflecting on the interface making it travel back and forth trough substructure B. Finally, consider the acceleration of the interface nodes given in figures 10-22c and 10-22d. It is seen that the travelling wave shows at the right times on the interface nodes. However, the amplitude differs from the amplitude of the reference solution. The amplitude for substructure A is overestimated, whereas the amplitudes for substructure B are underestimated. This indicates insufficient coupling, causing a significant part of the travelling wave to reflect on the interface. This can be assigned to underestimation of the interface forces.

Summarised, it is seen that the structure is not fully coupled, or the coupling is incomplete. This incomplete coupling is induced by underestimation of the interface force. In section 8-4-4 it was seen that choosing a smaller Courant's number, the compatibility error decreases. Therefore it is expected that in the example the compatibility error can also be decreased by choosing a smaller Courant's number.

---

[5] The reference solution is obtained similar as before; by simulating a bar twice the length divided over 100 elements and obtain its acceleration IRF using Newmark time integration using the initial force condition.

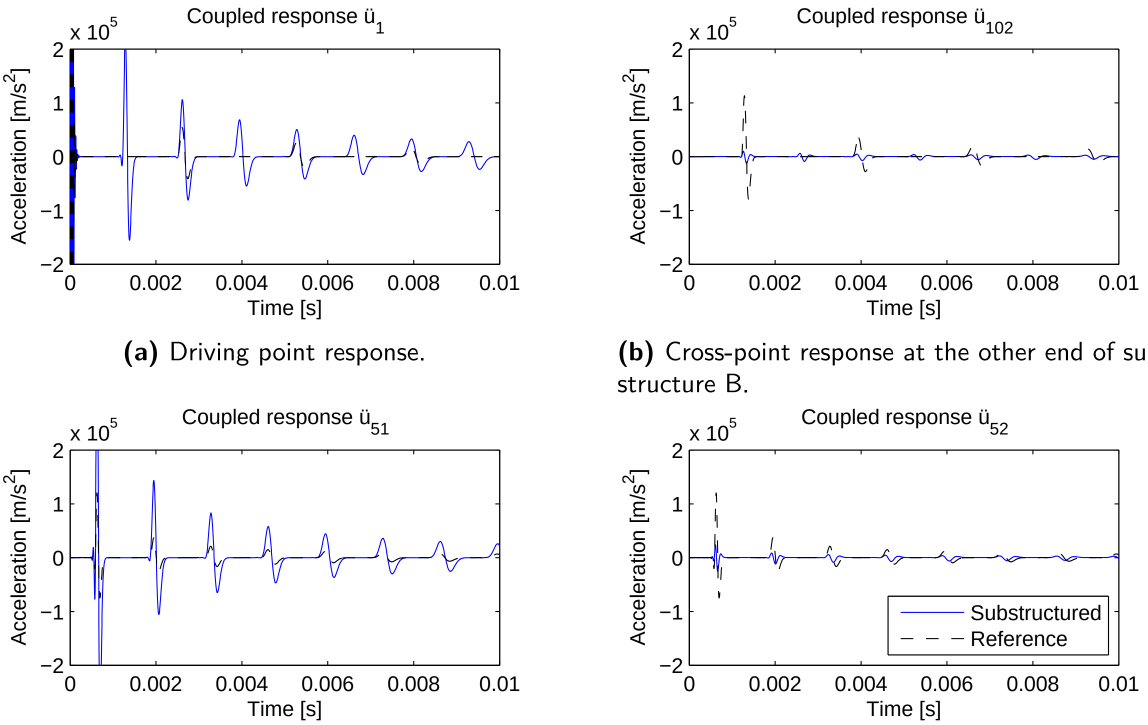

(a) Driving point response.

(b) Cross-point response at the other end of substructure B.

(c) Interface response for substructure A.

(d) Interface response for substructure B.

Figure 10-22: Accelerations for the coupled structure for an impact on the left end of substructure A, i.e. node 1.

Chapter 11

Conclusions and recommendations

This chapter concludes part II. First the last few chapters are concluded in section 11-1. Next, recommendations are made in section 11-2.

11-1 Conclusions

This part has shown that it is possible to couple the dynamics of structures using their Impulse Response Functions. Chapter 8 has discussed three different methods to do so, namely by using either the analytical approach, the classical discrete time domain approach and the proposed inverse IRF filter approach. All methods derive the interface forces required for coupling, but a distinction can be made in how this is done.
The classical approach derives the interface forces for the current time step using the time history of the coupled system. This method ensures compatibility since the compatibility equation is explicitly solved for every time the interface force is calculated. The method is however, sensitive to errors on the first time step of driving point IRFs of the coupling nodes. The analytical approach and the inverse IRF derive a full-domain solution for the interface force at once without using any time history data of the coupled system. For the analytical approach, this can be done only when the analytical expression for the IRF is available, which is in practice hardly ever the case. For the inverse IRF filter approach, which uses discrete data, it was seen that solving the interface force for the full domain at once has a disadvantage. The equilibrium condition is not explicitly solved every time step, as is done in the classical discrete time domain approach, making the method prone to compatibility errors.

It was discussed that the proposed inverse IRF filter approach is not always suited to couple structural dynamics. There has to exist an inverse filter for the driving point IRFs to be coupled on. This inverse filter requires the IRFs to be converging. In order for the filter to be causal, it is also required that the IRF has its maximum value at $t = 0$. These requirements do not apply to the classical discrete time domain approach.

Chapter 9 illustrates the contributions of the excitation and interface force for the example of a propagating wave in a bar. The contribution of the excitation showed a wave travelling back and forth trough the bar, reflecting at the ends. The contribution of the interface force showed a 'negative' wave with the same behaviour cancelling out the original wave after it should have propagated to the next structure. This constant cancellation of previous contributions only by satisfying coupling criteria, makes the procedure prone to errors, especially on the first time step of the driving point IRFs used for coupling. The effects as a results of these errors can be divided in two categories; incomplete and unstable coupling.
Incomplete coupling consists of information being not properly transmitted from one substructure to the next. This happens typically when Courant's criterion is not satisfied, i.e. the information never appears on the interface DoFs. Also non-causalities in the IRFs disturb this cancellation process resulting in errors in the coupled response.
Unstable coupling occurs when energy keeps being added to the system. It was shown that energy is added to the system when an impulse requires more energy to cancel out than was used to initiate it. This typically happens when the first values of a driving point IRF of a point for coupling, describing the initiated wave are underestimated. In order to prevent this, the system of IRFs should be causal at all time, i.e. the amount of energy present in the system can never increase. This prohibits an increase in total energy caused by the interface force which transits information, e.g. a wave, from one substructure to the next.

The case studies performed in chapter 10 has shown successful coupling using analytically obtained IRFs by MSP. The classical discrete approach has shown proper propagation of the wave, while the inverse IRF approach showed incomplete coupling, which is assigned to the Courant's number. It was discussed earlier that inverse IRF method yields better results when the Courant's number is chosen smaller.
Furthermore it was shown that when using IRFs obtained using an imperfect impulse, all coupling algorithms fail. This is directly assigned to the fact that these IRFs are non-causal, i.e. their energy increases over the period where the impulse is applied.
The case study shown was rather strict. Relatively high frequent content is required to show smooth reflecting and propagating waves in a bar. When for instance a plate is used, more coupling present between the nodes, yielding in a more diffuse response for an impulse, which is expected to be less prone to the discussed errors.

11-2 Recommendations

Towards successful coupling with experimentally obtained IRFs it is useful to describe a method which allows altering of the IRF such that the errors leading to incomplete and unstable coupling disappear, but the fundamental behaviour of the structure described by the IRF remains unchanged. The criteria formulated in chapter 9 can form the basis for this work.

The substructuring methods described in this work have not yet been applied in a real-time environment. When one desires to do so, unforeseen limitation may arise which require more research.

Finally, improvements for the current state of Impulse Based Structuring may be sought for in the domain of using NARMAX[1] techniques.[19] The finite impulse response can be included implicitly in this technique which is used to predict the coupled response. This is ongoing research at Technische Universität München.[2]

---

[1] Nonlinear Auto-Regressive Moving Average with eXogenous inputs

[2] Fakultät für Maschinenwesen, Chair of Applied Mechanics

Appendix A

Error piecewise linear approximation

This chapter derives the order of the error made when assuming piecewise linear behaviour for the functions in the convolution product by means of a Taylor expansion. The derivation of the error on functions $h(t)$ and $f(t)$ themselves are derived using $f(t)$ as example for t on an interval $[a, b]$, with size Δt. Next an interval $[0, \Delta t]$ is substituted in the obtained functions and the convolution product is solved.

Consider the following two Taylor expansions for f_a and f_b around arbitrary point $f(t)$.

$$f_a = f(t) + (a-t)\, f'(t) + \frac{1}{2}\,(a-t)^2\, f''(t) + \mathcal{O}((a-t)^3 f'''(t)) \tag{A-1a}$$

$$f_b = f(t) + (b-t)\, f'(t) + \frac{1}{2}\,(b-t)^2\, f''(t) + \mathcal{O}((b-t)^3 f'''(t)) \tag{A-1b}$$

Next, the piecewise linear force is defined as $p(t)$ and can be written such that:

$$p(t) \triangleq \frac{t-b}{a-b}\, f_a - \frac{t-a}{a-b}\, f_b \qquad \text{for} \qquad t \in [a, b] \tag{A-2}$$

Now substitution of (A-1) in (A-2) gives:

$$\begin{aligned} p(t) &= \frac{(t-b)-(t-a)}{a-b}\, f(t) + \frac{(t-b)(a-t)-(t-a)(b-t)}{a-b}\, f'(t) \\ &\quad + \frac{1}{2}\left(\frac{(t-b)(a-t)^2-(t-a)(b-t)^2}{a-b}\right) f''(t) + \mathcal{O}(\Delta t)^3 f'''(t)) \\ &= f(t) + \frac{1}{2}(t-a)(t-b)\, f''(t) + \mathcal{O}(\Delta t^3 f'''(t)) \end{aligned} \tag{A-3}$$

Given that $\max\Big((t-a)(t-b)\Big) = \frac{\Delta t^2}{4}$ for $t \in [a, b]$, so the error made is of order $\mathcal{O}(\Delta t^2 f''(t))$, giving for $f(t)$:

$$f(t) = \frac{t-b}{a-b}\, f_a - \frac{t-a}{a-b}\, f_b - \frac{1}{2}(t-a)(t-b)\, f''(t) + \mathcal{O}(\Delta t^3 f'''(t)) \qquad \text{for} \qquad t \in [a, b] \tag{A-4}$$

And similarly for IRF $h(t)$:

$$h(t) = \frac{t-b}{a-b}\,h_a - \frac{t-a}{a-b}\,h_b - \frac{1}{2}(t-a)(t-b)\,h''(t) + \mathcal{O}(\Delta t^3 h'''(t)) \qquad \text{for} \qquad t \in [a,b] \quad \text{(A-5)}$$

As said, both functions can now be substituted in the convolution product (3-5) using interval $[0, \Delta t]$, seeking for a solution on time $t = t_n$.

$$\begin{aligned} u_n &= \int_0^{\Delta t} h(\Delta t - \tau)\, f(\tau)\,\mathrm{d}\tau \\ &= \int_0^{\Delta t} \left[\left(\frac{\tau}{\Delta t}h_0 + \frac{\Delta t - \tau}{\Delta t}h_n + \frac{1}{2}(\Delta t - \tau)\tau h''(t) + \mathcal{O}(\Delta t^3 h'''(t))\right) \dots \right. \\ &\qquad \left. \left(\frac{\Delta t - \tau}{\Delta t}f_0 + \frac{\tau}{\Delta t}f_n + \frac{1}{2}\tau(\Delta t - \tau)f''(t) + \mathcal{O}(\Delta t^3 f'''(t))\right)\right] \mathrm{d}\tau \end{aligned} \qquad \text{(A-6)}$$

Next, the parenthesis can be worked out. It is seen that the residual from both the IRF $h(t)$ and the excitation $f(t)$ is now combined in one residual $\mathcal{O}(\Delta t^3)$, which is still of the same order.

$$\begin{aligned} u_n = \int_0^{\Delta t} & \frac{-\tau^2 + \Delta t\tau}{\Delta t^2}h_0 f_0 + \frac{\tau^2 - 2\tau\Delta t + \Delta t^2}{\Delta t^2}h_n f_0 + \frac{\tau^3 - 2\tau^2\Delta t + \tau\Delta t^2}{2\Delta t}h''(t) f_0 \\ & + \frac{\tau^2}{\Delta t^2}h_0 f_n + \frac{-\tau^2 + \tau\Delta t}{\Delta t^2}h_n f_n + \frac{-\tau^3 + \tau^2\Delta t}{2\Delta t}h''(t) f_n \\ & + \frac{-\tau^3 + \tau 2\Delta t}{2\Delta t}h_0 f''(t) + \frac{\tau^3 - 2\tau^2\Delta t + \tau\Delta t^2}{2\Delta t}h_n f''(t) \\ & + \frac{\tau^4 - 2\tau^3\Delta t + \tau^2\Delta t^2}{4}h''(t) f''(t) + \mathcal{O}(\Delta t^3)\,\mathrm{d}\tau \end{aligned} \qquad \text{(A-7)}$$

Next, the integral can be solved.

$$\begin{aligned} u_n = & \left(\frac{-\tau^3}{3\Delta t^2} + \frac{\tau^2\Delta t}{2\Delta t^2}\right) h_0 f_0 + \left(\frac{\tau^3}{3\Delta t^2} - \frac{\tau^2\Delta t}{\Delta t^2} + \frac{\tau\Delta t^2}{\Delta t^2}\right) h_n f_0 \\ & + \left(\frac{\tau^4}{8\Delta t} - \frac{\tau^3\Delta t}{3\Delta t} + \frac{\tau^2\Delta t^2}{4\Delta t}\right) h''(t) f_0 + \frac{\tau^3}{3\Delta t^2}h_0 f_n + \left(\frac{-\tau^3}{3\Delta t^2} + \frac{\tau^2\Delta t}{2\Delta t^2}\right) h_n f_n \\ & + \left(\frac{-\tau^4}{8\Delta t} + \frac{\tau^3\Delta t}{6^{\Delta}t}\right) h''(t) f_n + \left(\frac{-\tau^4}{8\Delta t} + \frac{\tau^3\Delta t}{6^{\Delta}t}\right) h_0 f''(t) \\ & + \left(\frac{\tau^4}{8\Delta t} - \frac{\tau^3\Delta t}{3\Delta t} + \frac{\tau^2\Delta t^2}{4\Delta t}\right) h_n f''(t) + \left(\frac{\tau^5}{20} - \frac{\tau^4\Delta t}{8} + \frac{\tau^3\Delta t^2}{12}\right) h''(t) f''(t) \\ & + \mathcal{O}(\Delta t^4)\Big|_0^{\Delta t} \end{aligned} \qquad \text{(A-8)}$$

Note that the original order of the original residue has increased due to the integration. Now solving for the specified interval $[0, \Delta t]$:

$$\begin{aligned} u_n = & \frac{\Delta t}{6}h_0 f_0 + \frac{\Delta t}{3}h_n f_0 + \frac{\Delta t^3}{24}h''(t) f_0 + \frac{\Delta t}{3}h_0 f_n + \frac{\Delta t}{6}h_n f_n + \frac{\Delta t^3}{24}h''(t) f_n \\ & + \frac{\Delta t^3}{24}h_0 f''(t) + \frac{\Delta t^3}{24}h_n f''(t) + \mathcal{O}(\Delta t^4) \end{aligned} \qquad \text{(A-9)}$$

A lot of third order terms of Δt appear. Regarding those as residue, this can be written as

$$u_n = \frac{\Delta t}{6} h_0 f_0 + \frac{\Delta t}{3} h_n f_0 + \frac{\Delta t}{3} h_0 f_n + \frac{\Delta t}{6} h_n f_n + \mathcal{O}(\Delta t^3) \tag{A-10}$$

It can be seen that the obtained solution equals the discrete formulation of the convolution product using piecewise linear functions, as discussed in section 3-2. This proves that the error made using this algorithm is of third order.

Appendix B

Exact IRF Derivation

This chapter is dedicated to the derivation of single DoF Impulse Response Functions. First the harmonic oscillation is derived. Afterwards rigid body motion is discussed.

B-1 Harmonic oscillation

This section first derives the IRF of a harmonic oscillation. When the displacement IRF is known, the velocity and acceleration IRF is determined by taking its derivative.

B-1-1 Displacement IRF

A single DoF system is subjected to the following equation of motion:

$$m\,\ddot{u}(t) + c\,\dot{u} + k\,u(t) = \delta(t) \tag{B-1}$$

Using a transformation to the Laplace domain, the equation rewrites to

$$\mathcal{L}\left\{m\,\ddot{u}(t) + c\,\dot{u} + k\,u(t)\right\}(s) = \mathcal{L}\{\delta(t)\}(s) \tag{B-2}$$

$$m\,\left(s^2\,U(s) - s\,u(0) - \dot{u}(0)\right) + c\,\left(s\,U(s) - u(0)\right) + k\,U(s) = 1 \tag{B-3}$$

$$(m\,s^2 + c\,s + k)\,U(s) = 1 + m\,\left(s\,u(0) + \dot{u}(0)\right) + c\,u(0) \tag{B-4}$$

The system is assumed to be initially at rest. Hence, $u(0) = 0$ and $\dot{u}(0) = 0$. This reduces the equation to

$$U(s) = \frac{1}{m\,s^2 + c\,s + k} \tag{B-5}$$

which can be used to find a solution for $u(t)$ after some rewriting. We can define:

$$\begin{aligned}
\omega_n &\triangleq \sqrt{\frac{k}{m}} \\
\zeta &\triangleq \frac{c}{2\sqrt{m\,k}} = \frac{c}{2\,m\,\omega_n} \\
\omega_d &\triangleq \omega_n\sqrt{1-\zeta^2} = \sqrt{\omega_n^2-\zeta^2\,\omega_n^2}
\end{aligned}$$

And we can choose complex pair:

$$\lambda \triangleq \zeta\,\omega_n - i\,\omega_d \tag{B-6}$$

$$\bar{\lambda} \triangleq \zeta\,\omega_n + i\,\omega_d \tag{B-7}$$

Continuing to rewrite the expression:

$$U(s) = \frac{1}{2\,i\,\omega_d\,m}\left(\frac{2\,i\,\omega_d}{s^2+\frac{c}{m}\,s+\frac{k}{m}}\right) \tag{B-8}$$

$$U(s) = \frac{1}{2\,i\,\omega_d\,m}\left(\frac{2\,i\,\omega_d}{s^2+2\,\zeta\,\omega_n\,s+\omega_n^2}\right) \tag{B-9}$$

$$U(s) = \frac{1}{2\,i\,\omega_d\,m}\left(\frac{\bar{\lambda}-\lambda}{s^2+(\lambda+\bar{\lambda})\,s+\lambda\,\bar{\lambda}}\right) \tag{B-10}$$

$$U(s) = \frac{1}{2\,i\,\omega_d\,m}\left(\frac{s+\bar{\lambda}}{(s+\lambda)(s+\bar{\lambda})}-\frac{s+\lambda}{(s+\lambda)(s+\bar{\lambda})}\right) \tag{B-11}$$

$$U(s) = \frac{1}{2\,i\,\omega_d\,m}\left(\frac{1}{s+\lambda}-\frac{1}{s+\bar{\lambda}}\right) \tag{B-12}$$

Note that this notation represents a pole/residue parametrisation.[4] The latter expression allows transformation back to the time domain trough inverse Laplace transformation and eventually yields a neat expression for $u(t)$.

$$\mathcal{L}^{-1}\{U(s)\}(t) = \mathcal{L}^{-1}\left\{\frac{1}{2\,i\,\omega_d\,m}\left(\frac{1}{s+\lambda}-\frac{1}{s+\bar{\lambda}}\right)\right\}(t) \tag{B-13}$$

$$u(t) = \frac{e^{-\lambda\,t}-e^{-\bar{\lambda}t}}{2\,i\,\omega_d\,m} \tag{B-14}$$

$$u(t) = \frac{e^{(-\zeta\,\omega_n+i\,\omega_d)\,t}-e^{(-\zeta\,\omega_n-i\,\omega_d)\,t}}{2\,i\,\omega_d\,m} \tag{B-15}$$

$$u(t) = \frac{\sin(\omega_d\,t)}{m\,\omega_d}\,e^{-\zeta\,\omega_n\,t} \tag{B-16}$$

The found expression for the displacements is the result of a perfect Dirac impulse and can therefore be used as IRF.

B-1-2 Velocity IRF

To obtain the velocity IRF $\dot{u}(t)$, we start from taking the derivative of (B-15).

$$\dot{u}(t) = \frac{(-\zeta\,\omega_n+i\,\omega_d)\,e^{(-\zeta\,\omega_n+i\,\omega_d)\,t}-(-\zeta\,\omega_n-i\,\omega_d)\,e^{(-\zeta\,\omega_n-i\,\omega_d)\,t}}{2\,i\,\omega_d\,m} \tag{B-17}$$

After rewriting and using $\theta = \tan^{-1} \frac{\zeta\,\omega_n}{\omega_d}$, the following relation is obtained:

$$\dot{u}(t) = \frac{1}{2\,m} \left(e^{(-\zeta\,\omega_n + i\,\omega_d)\,t} + e^{(-\zeta\,\omega_n - i\,\omega_d)\,t}\right) + \frac{\zeta\,\omega_n}{2\,i\,\omega_d\,m} \left(e^{(-\zeta\,\omega_n - i\,\omega_d)\,t} - e^{(-\zeta\,\omega_n + i\,\omega_d)\,t}\right) \tag{B-18}$$

$$\dot{u}(t) = \frac{1}{m} \left(\cos\omega_d\,t - \frac{\zeta\,\omega_n}{\omega_d}\,\sin\omega_d\,t\right) e^{-\zeta\,\omega_n\,t} \tag{B-19}$$

$$\dot{u}(t) = \frac{\omega_n}{m\,\omega_d}\,\cos\left(\omega_d\,t + \theta\right) e^{-\zeta\,\omega_n\,t} \tag{B-20}$$

B-1-3 Acceleration IRF

Next, to obtain the acceleration IRF $\ddot{u}(t)$, we start from taking the second derivative of (B-15) and start rewriting:

$$\ddot{u}(t) = \frac{(-\zeta\,\omega_n + i\,\omega_d)^2\,e^{(-\zeta\,\omega_n + i\,\omega_d)\,t} - (-\zeta\,\omega_n - i\,\omega_d)^2\,e^{(-\zeta\,\omega_n - i\,\omega_d)\,t}}{2\,i\,\omega_d\,m} \tag{B-21}$$

$$\ddot{u}(t) = \frac{(\zeta^2\,\omega_n^2 - 2\,i\,\zeta\,\omega_n\,\omega_d - \omega_d^2)\,e^{(-\zeta\,\omega_n + i\,\omega_d)\,t} - (\zeta^2\,\omega_n^2 + 2\,i\,\zeta\,\omega_n\,\omega_d - \omega_d^2)\,e^{(-\zeta\,\omega_n - i\,\omega_d)\,t}}{2\,i\,\omega_d\,m} \tag{B-22}$$

$$\ddot{u}(t) = \frac{\zeta^2\,\omega_n^2 - \omega_d^2}{2\,i\,\omega_d\,m} \left(e^{(-\zeta\,\omega_n + i\,\omega_d)\,t} - e^{(-\zeta\,\omega_n - i\,\omega_d)\,t}\right) - \frac{\zeta\,\omega_n}{m} \left(e^{(-\zeta\,\omega_n + i\,\omega_d)\,t} + e^{(-\zeta\,\omega_n - i\,\omega_d)\,t}\right) \tag{B-23}$$

$$\ddot{u}(t) = -\left(\frac{\omega_d^2 - \zeta^2\,\omega_n^2}{\omega_d\,m}\,\sin(\omega_d\,t) + \frac{2\,\zeta\,\omega_n}{m}\,\cos(\omega_d\,t)\right) e^{-\zeta\,\omega_n\,t} \tag{B-24}$$

It would be convenient to obtain a solution in a form analogue to those of $u(t)$ and $\dot{u}(t)$, which could be

$$\ddot{u}(t) = -A\,\sin(\omega_d\,t + \phi)\,e^{-\zeta\,\omega_n\,t} \tag{B-25}$$

A solution in this form can be found. First, solving for the amplitude A, using Pythagoras :

$$A = \sqrt{\left(\frac{\omega_d^2 - \zeta^2\,\omega_n^2}{\omega_d\,m}\right)^2 + \left(\frac{2\,\zeta\,\omega_n}{m}\right)^2} \tag{B-26}$$

$$= \frac{\sqrt{(\omega_d^2 - \zeta^2\,\omega_n^2)^2 + (2\,\zeta\,\omega_n\,\omega_d)^2}}{\omega_d\,m} \tag{B-27}$$

$$= \frac{\sqrt{(\omega_d^4 - 2\,\zeta^2\,\omega_n^2\,\omega_d^2 + \zeta^4\,\omega_n^4) + (4\,\zeta^2\,\omega_n^2\,\omega_d^2)}}{\omega_d\,m} \tag{B-28}$$

$$= \frac{\sqrt{(\omega_d^2 + \zeta^2\,\omega_n^2)^2}}{\omega_d\,m} \tag{B-29}$$

$$A = \frac{\omega_n^2}{\omega_d\,m} \tag{B-30}$$

Next, solving for the phase shift ϕ:

$$\phi = \tan^{-1}\left(\frac{\left(\frac{2\,\zeta\,\omega_n}{m}\right)}{\left(\frac{\omega_d^2-\zeta^2\,\omega_n^2}{\omega_d\,m}\right)}\right) = \tan^{-1}\left(\frac{2\,\zeta\,\omega_n\,\omega_d}{\omega_d^2-\zeta^2\,\omega_n^2}\right) \tag{B-31}$$

Now to show that this phase shift between velocity and acceleration is consistent with the phase shift between displacement and velocity, the following inverse trigonometric relation can be applied:

$$\tan^{-1}(x) = 2\,\tan^{-1}\left(\frac{x}{1+\sqrt{1+x^2}}\right) \tag{B-32}$$

Substituting

$$x = \frac{2\,\zeta\,\omega_n\,\omega_d}{\omega_d^2-\zeta^2\,\omega_n^2} \tag{B-33}$$

and rewriting yields

$$\phi = 2\,\tan^{-1}\left(\frac{\frac{2\,\zeta\,\omega_n\,\omega_d}{\omega_d^2-\zeta^2\,\omega_n^2}}{1+\sqrt{1+\left(\frac{2\,\zeta\,\omega_n\,\omega_d}{\omega_d^2-\zeta^2\,\omega_n^2}\right)^2}}\right) \tag{B-34}$$

$$\phi = 2\,\tan^{-1}\left(\frac{2\,\zeta\,\omega_n\,\omega_d}{\omega_d^2-\zeta^2\,\omega_n^2+\sqrt{(\omega_d^2-\zeta^2\,\omega_n^2)^2+4\,\zeta^2\,\omega_n^2\,\omega_d^2}}\right) \tag{B-35}$$

$$\phi = 2\,\tan^{-1}\left(\frac{2\,\zeta\,\omega_n\,\omega_d}{\omega_d^2-\zeta^2\,\omega_n^2+\sqrt{(\omega_d^4-2\,\zeta^2\,\omega_n^2\,\omega_d^2+\zeta^4\,\omega_n^4)+4\,\zeta^2\,\omega_n^2\,\omega_d^2}}\right) \tag{B-36}$$

$$\phi = 2\,\tan^{-1}\left(\frac{2\,\zeta\,\omega_n\,\omega_d}{\omega_d^2-\zeta^2\,\omega_n^2+\sqrt{(\omega_d^2+\zeta^2\,\omega_n^2)^2}}\right) \tag{B-37}$$

$$\phi = 2\,\tan^{-1}\left(\frac{\zeta\,\omega_n}{\omega_d}\right) = 2\,\theta \tag{B-38}$$

Hence, the solution for $\ddot{u}(t)$ can be neatly written as

$$\ddot{u}(t) = -\frac{\omega_n^2}{\omega_d\,m}\,\sin(\omega_d\,t+2\,\theta)\,e^{-\zeta\,\omega_n\,t} \tag{B-39}$$

B-1-4 n-th derivative IRF

In a more generic way, it is possible to write:

$$\frac{\partial^n\,u(t)}{\partial\,t^n} = \frac{(-\zeta\,\omega_n+i\,\omega_d)^n\,e^{(-\zeta\,\omega_n+i\,\omega_d)\,t}-(-\zeta\,\omega_n-i\,\omega_d)^n 2\,e^{(-\zeta\,\omega_n-i\,\omega_d)\,t}}{2\,i\,\omega_d\,m} \tag{B-40}$$

This relation can eventually be rewritten to

$$\frac{\partial^n\,u(t)}{\partial\,t^n} = \frac{\omega_n^n}{\omega_d\,m}\,\sin(\omega_d\,t+n\,(\frac{\pi}{2}+\theta))\,e^{-\zeta\,\omega_n\,t} \tag{B-41}$$

which might be useful for programming purposes. The relation also holds for negative values for n indicating primitive functions.

B-2 Rigid Body Motion

This section derives the IRFs for rigid body movement. First the undamped case is discussed, afterwards the undamped case.

B-2-1 Undamped RBM

A rigid body, assumed to undergo undamped rigid body motion is subjected to the following equation of motion:

$$m\,\ddot{u}(t) = \delta(t) \tag{B-42}$$

Applying the Laplace transformation and rewriting yields:

$$\mathcal{L}\{m\,\ddot{u}(t)\} = \mathcal{L}\{\delta(t)\} \tag{B-43}$$

$$m\,\left(s^2\,U(s) - s\,u(0) - \dot{u}(0)\right) = 1 \tag{B-44}$$

Since we assume the system to be initially at rest, the equation can be reduced. This reduction and the inverse Laplace transformation yield:

$$U(s) = \frac{1}{m\,s^2} \tag{B-45}$$

$$\mathcal{L}^{-1}\{U(s)\} = \mathcal{L}^{-1}\left\{\frac{1}{m\,s^2}\right\} \tag{B-46}$$

$$u(t) = \frac{t}{m} \tag{B-47}$$

And to obtain the expressions for velocity $\dot{u}(t)$ and acceleration $\ddot{u}(t)$, taking the derivative functions yields:

$$\dot{u}(t) = \frac{1}{m} \tag{B-48}$$

$$\ddot{u}(t) = 0 \tag{B-49}$$

B-2-2 Damped RBM

A rigid body, assumed to undergo damped rigid body motion is subjected to the following equation of motion:

$$m\,\ddot{u}(t) + c\,\dot{u}(t) = \delta(t) \tag{B-50}$$

Applying the Laplace transformation and rewriting yields:

$$\mathcal{L}\{m\,\ddot{u}(t) + c\,\dot{u}(t)\} = \mathcal{L}\{\delta(t)\} \tag{B-51}$$

$$m\,\left(s^2\,U(s) - s\,u(0) - \dot{u}(0)\right) + c\,\left(s\,U(s) - u(0)\right) = 1 \tag{B-52}$$

Since we assume the system to be initially at rest, the equation can be reduced. This reduction and the inverse Laplace transformation yield:

$$U(s) = \frac{1}{m\,s^2 + c\,s} \tag{B-53}$$

$$U(s) = \frac{1}{c}\,\frac{\frac{c}{m}}{s\,(s+\frac{c}{m})} \tag{B-54}$$

$$\mathcal{L}^{-1}\{U(s)\} = \mathcal{L}^{-1}\left\{\frac{1}{c}\,\frac{\frac{c}{m}}{s\,(s+\frac{c}{m})}\right\} \tag{B-55}$$

$$u(t) = \frac{1}{c}\,\left(1 - e^{-\frac{c}{m}\,t}\right) \tag{B-56}$$

And to obtain the expressions for velocity $\dot{u}(t)$ and acceleration $\ddot{u}(t)$, taking the derivative functions yields:

$$\dot{u}(t) = \frac{1}{m}\,e^{-\frac{c}{m}\,t} \tag{B-57}$$

$$\ddot{u}(t) = -\frac{c}{m^2}\,e^{-\frac{c}{m}\,t} \tag{B-58}$$

It can be even be shown that when $c \to 0$, this solution yields the solutions for the undamped system:

$$u(t) = \lim_{c\to 0} \frac{1}{c}\,\left(1 - e^{-\frac{c}{m}\,t}\right) = \frac{t}{m} \tag{B-59}$$

$$\dot{u}(t) = \lim_{c\to 0} \frac{1}{m}\,e^{-\frac{c}{m}\,t} = \frac{1}{m} \tag{B-60}$$

$$\ddot{u}(t) = \lim_{c\to 0} -\frac{c}{m^2}\,e^{-\frac{c}{m}\,t} = 0 \tag{B-61}$$

Appendix C

Matrix Recurrence Procedure Derivation

This chapter is dedicated to the derivation of the matrix recurrence procedure for modes. First, the algorithm for the vibration mode is extensively derived. Afterwards, this derivation is extended for undamped and damped rigid body modes.

C-1 Vibration mode

A vibration mode is subjected to the following equation of motion:

$$\ddot{\eta}(t) + 2\,\zeta\,\omega_n\,\dot{\eta}(t) + \omega_n^2\eta(t) = \phi(t) \tag{C-1}$$

An expression for the modal amplitude $\eta(t)$ can be found using a transformation trough the Laplace domain.

$$\mathcal{L}\left\{\ddot{\eta}(t) + 2\,\zeta\,\omega_n\,\dot{\eta}(t) + \omega_n^2\eta(t)\right\} = \mathcal{L}\left\{\phi(t)\right\} \tag{C-2}$$

$$s^2\eta(s) - s\eta(0) - \dot{\eta}(0) + (2\,\zeta\,\omega_n)(s\eta(s) - \eta(0)) + \omega_n^2\eta(s) = \phi(s) \tag{C-3}$$

$$\eta(s) = \frac{\eta(0)\,s}{s^2 + 2\,\zeta\,\omega_n + \omega_n^2} + \frac{\dot{\eta}(0) + 2\,\zeta\,\omega_n\eta(0)}{s^2 + 2\,\zeta\,\omega_n + \omega_n^2} + \frac{\phi(s)}{s^2 + 2\,\zeta\,\omega_n + \omega_n^2} \tag{C-4}$$

Now by defining the modal Impulse Response function and its derivative using

$$\mathcal{L}^{-1}\left\{\frac{1}{s^2 + 2\,\zeta\,\omega_n + \omega_n^2}\right\} = h(t) = \frac{\sin(\omega_d t)}{\omega_d}\,e^{-\zeta\omega_n t} \tag{C-5}$$

$$\mathcal{L}^{-1}\left\{\frac{s}{s^2 + 2\,\zeta\,\omega_n + \omega_n^2}\right\} = \dot{h}(t) = \frac{\omega_n}{\omega_d}\,\cos(\omega_d t + \theta)\,e^{-\zeta\omega_n t} \tag{C-6}$$

and applying the inverse Laplace transformation, we can set up the expression for the modal amplitude $\eta(t)$ as

$$\eta(t) = \eta(0)\,\dot{h}(t) + (\dot{\eta}(0) + 2\,\zeta\,\omega_n\eta(0))\,h(t) + \int_0^t \phi(\tau)\,h(t-\tau)\,\mathrm{d}\tau \tag{C-7}$$

Now since the initial conditions are still preserved in the equation by substituting interval $[0; t]$ with $[t_n; t_{n+1}]$:

$$\begin{aligned}\eta_{n+1} = \eta_n\, \dot{h}(\Delta t) + \left(\dot{\eta}_{n+1} + 2\,\zeta\,\omega_n\eta_n\right) h(\Delta t) \\ + \int_{t_n}^{t_{n+1}} \phi(\tau)\, h(t_{n+1}-\tau)\,\mathrm{d}\tau\end{aligned} \tag{C-8}$$

C-1-1 Solving the convolution integral

In order to solve the convolution integral $\int_{t_n}^{t_{n+1}} \phi(\tau)\, h(t_{n+1}-\tau)\,\mathrm{d}\tau$, integration by parts is required. Integration by parts states $\int U dV = UV - \int V dU$. Applying this yields:

$$\begin{aligned}\int_{t_n}^{t_{n+1}} \phi(\tau)\, h(t_{n+1}-\tau)\,\mathrm{d}\tau = &\underbrace{\phi(\tau)\int h(t_{n+1}-\tau)\mathrm{d}\tau\Big|_{t_n}^{t_{n+1}}}_{\mathbf{A}} \\ &\underbrace{- \int_{t_n}^{t_{n+1}} \dot{\phi}(\tau)\int h(t_{n+1}-\tau)\mathrm{d}\tau\mathrm{d}\tau}_{\mathbf{B}}\end{aligned} \tag{C-9}$$

The solution can be split into two parts which can be solved separately. To do so, the integral and double integral of $h(t)$ are required. Fortunately is can be shown that these follow the same rules as shown earlier with its derivatives[1]:

$$h(t_{n-1}-\tau) = \frac{\sin(\omega_d(t_{n-1}-\tau))}{\omega_d}\, e^{-\zeta\omega_n(t_{n-1}-\tau)} \tag{C-10a}$$

$$\int h(t_{n-1}-\tau)\,\mathrm{d}\tau = \frac{\cos(\omega_d(t_{n-1}-\tau)-\theta)}{\omega_d\omega_n}\, e^{-\zeta\omega_n(t_{n-1}-\tau)} \tag{C-10b}$$

$$\iint h(t_{n-1}-\tau)\,\mathrm{d}\tau\mathrm{d}\tau = -\frac{\sin(\omega_d(t_{n-1}-\tau)-2\theta)}{\omega_d\omega_n^2}\, e^{-\zeta\omega_n(t_{n-1}-\tau)} \tag{C-10c}$$

For the excitation $\phi(\tau)$ a piecewise linear variation is assumed. Its derivative $\dot{\phi}(\tau)$ is eventually also required and is found by taking the derivative with respect to τ:

$$\phi(\tau) = \phi_n\frac{t_{n+1}-\tau}{\Delta t} + \phi_{n+1}\frac{\tau - t_n}{\Delta t} \tag{C-11a}$$

$$\dot{\phi}(\tau) = \frac{\phi_{n+1}-\phi_n}{\Delta t} \tag{C-11b}$$

Now starting with solving part **A** of (C-9):

$$\phi(\tau)\int h(t_{n+1}-\tau)\mathrm{d}\tau\Big|_{t_n}^{t_{n+1}}$$

$$= \left(\phi_n\frac{t_{n+1}-\tau}{\Delta t} + \phi_{n+1}\frac{\tau - t_n}{\Delta t}\right)\frac{\cos(\omega_d(t_{n-1}-\tau)-\theta)}{\omega_d\omega_n}\, e^{-\zeta\omega_n(t_{n-1}-\tau)}\Big|_{t_n}^{t_{n+1}} \tag{C-12}$$

$$= \frac{\phi_{n+1}}{\omega_d\omega_n}\cos(-\theta) - \frac{\phi_n}{\omega_d\omega_n}\cos(\omega_d\Delta t - \theta)\, e^{-\zeta\omega_n\Delta t} \tag{C-13}$$

---

[1] Also see equations (5-14)

Solving part $\mathbf{B}$ of (C-9):

$$\int_{t_n}^{t_{n+1}} \dot{\phi}(\tau) \int h(t_{n+1}-\tau)\mathrm{d}\tau\mathrm{d}\tau$$

$$\begin{aligned}
&= \frac{\phi_{n+1}-\phi_n}{\omega_d\omega_n\Delta t} \int_{t_n}^{t_{n+1}} \cos(\omega_d(t_{n-1}-\tau)-\theta)\, e^{-\zeta\omega_n(t_{n-1}-\tau)}\,\mathrm{d}\tau && \text{(C-14)}\\
&= -\frac{\phi_{n+1}-\phi_n}{\omega_d\omega_n^2\Delta t} \sin(\omega_d(t_{n-1}-\tau)-2\theta)\, e^{-\zeta\omega_n(t_{n-1}-\tau)}\Big|_{t_n}^{t_{n+1}} && \text{(C-15)}\\
&= \frac{\phi_{n+1}-\phi_n}{\omega_d\omega_n^2\Delta t}\big(\sin(\omega_d\Delta t-2\theta)\, e^{-\zeta\omega_n\Delta t} - \sin(-2\theta)\big) && \text{(C-16)}
\end{aligned}$$

Substituting both results in (C-9) then yields:

$$\int_{t_n}^{t_{n+1}} \phi(\tau)\, h(t_{n+1}-\tau)\,\mathrm{d}\tau$$

$$\begin{aligned}
&= \frac{\phi_n}{\omega_d\omega_n}\left(-\cos(\omega_d\Delta t-\theta)\, e^{-\zeta\omega_n\Delta t} + \frac{\sin(\omega_d\Delta t-2\theta)\, e^{-\zeta\omega_n\Delta t}+\sin(2\theta)}{\omega_n\Delta t}\right)\\
&+ \frac{\phi_{n+1}}{\omega_d\omega_n}\left(\cos(\theta) - \frac{\sin(\omega_d\Delta t-2\theta)\, e^{-\zeta\omega_n\Delta t}+\sin(2\theta)}{\omega_n\Delta t}\right)
\end{aligned} \tag{C-17}$$

Substituting the found solution for the convolution integral back into equation (C-7):

$$\begin{aligned}
\eta_{n+1} &= \eta_n\,\frac{\omega_n}{\omega_d}\,\cos(\omega_d\Delta t+\theta)\, e^{-\zeta\omega_n\Delta t}\\
&+ (\dot{\eta}_n + 2\,\zeta\,\omega_n\eta_n)\,\frac{\sin(\omega_d\Delta t)}{\omega_d}\, e^{-\zeta\omega_n\Delta t}\\
&+ \frac{\phi_n}{\omega_d\omega_n}\left(-\cos(\omega_d\Delta t-\theta)\, e^{-\zeta\omega_n\Delta t} + \frac{\sin(\omega_d\Delta t-2\theta)\, e^{-\zeta\omega_n\Delta t}+\sin(2\theta)}{\omega_n\Delta t}\right)\\
&+ \frac{\phi_{n+1}}{\omega_d\omega_n}\left(\cos(\theta) - \frac{\sin(\omega_d\Delta t-2\theta)\, e^{-\zeta\omega_n\Delta t}+\sin(2\theta)}{\omega_n\Delta t}\right)
\end{aligned} \tag{C-18}$$

C-1-2 Deriving modal velocity

The modal amplitude at time t_{n+1} requires, among other things, the modal velocity at time t_n. Therefore the modal velocity requires implementation in the recursive scheme. The modal velocity is determined by taking the derivative of η_{n+1} with respect to t_{n+1} and split into four parts as follows:

$$\begin{aligned}
\frac{\mathrm{d}\eta_{n+1}}{\mathrm{d}t_{n+1}} &= \dot{\eta}_{n+1} \\
&= \underbrace{\frac{\mathrm{d}}{\mathrm{d}t_{n+1}}\left[\eta_n \frac{\omega_n}{\omega_d}\cos(\omega_d \Delta t + \theta)\, e^{-\zeta\omega_n \Delta t}\right]}_{\mathbf{A}} \\
&\quad + \underbrace{\frac{\mathrm{d}}{\mathrm{d}t_{n+1}}\left[(\dot{\eta}_n + 2\,\zeta\,\omega_n \eta_n)\frac{\sin(\omega_d \Delta t)}{\omega_d}\, e^{-\zeta\omega_n \Delta t}\right]}_{\mathbf{B}} \\
&\quad + \underbrace{\frac{\mathrm{d}}{\mathrm{d}t_{n+1}}\left[\frac{\phi_n}{\omega_d\omega_n}\left(-\cos(\omega_d \Delta t - \theta)\, e^{-\zeta\omega_n \Delta t} + \frac{\sin(\omega_d \Delta t - 2\theta)\, e^{-\zeta\omega_n \Delta t} + \sin(2\theta)}{\omega_n \Delta t}\right)\right]}_{\mathbf{C}} \\
&\quad + \underbrace{\frac{\mathrm{d}}{\mathrm{d}t_{n+1}}\left[\frac{\phi_{n+1}}{\omega_d\omega_n}\left(\cos(\theta) - \frac{\sin(\omega_d \Delta t - 2\theta)\, e^{-\zeta\omega_n \Delta t} + \sin(2\theta)}{\omega_n \Delta t}\right)\right]}_{\mathbf{D}}
\end{aligned} \tag{C-19}$$

Starting by solving part **A** of (C-19):

$$\frac{\mathrm{d}}{\mathrm{d}t_{n+1}}\left[\eta_n \frac{\omega_n}{\omega_d}\cos(\omega_d \Delta t + \theta)\, e^{-\zeta\omega_n \Delta t}\right] = -\eta_n \frac{\omega_n^2}{\omega_d}\sin(\omega_d \Delta t + 2\theta)\, e^{-\zeta\omega_n \Delta t} \tag{C-20}$$

Next, solving part **B** of (C-19):

$$\begin{aligned}
&\frac{\mathrm{d}}{\mathrm{d}t_{n+1}}\left[(\dot{\eta}_{n+1} + 2\,\zeta\,\omega_n \eta_n)\frac{\sin(\omega_d \Delta t)}{\omega_d}\, e^{-\zeta\omega_n \Delta t}\right] \\
&\qquad = (\dot{\eta}_n + 2\,\zeta\,\omega_n \eta_n)\frac{\omega_n}{\omega_d}\cos(\omega_d \Delta t + \theta)\, e^{-\zeta\omega_n \Delta t}
\end{aligned} \tag{C-21}$$

Following up, part **C** of (C-19):

$$\begin{aligned}
&\frac{\mathrm{d}}{\mathrm{d}t_{n+1}}\left[\frac{\phi_n}{\omega_d\omega_n}\left(-\cos(\omega_d \Delta t - \theta)\, e^{-\zeta\omega_n \Delta t} + \frac{\sin(\omega_d \Delta t - 2\theta)\, e^{-\zeta\omega_n \Delta t} + \sin(2\theta)}{\omega_n \Delta t}\right)\right] \\
&\qquad = \frac{\phi_n}{\omega_d\omega_n}\left(\omega_n \sin(\omega_d \Delta t)\, e^{-\zeta\omega_n \Delta t} + \frac{\cos(\omega_d \Delta t - \theta)\, e^{-\zeta\omega_n \Delta t}}{\Delta t}\right. \\
&\qquad\qquad \left. - \frac{\sin(\omega_d \Delta t - 2\theta)\, e^{-\zeta\omega_n \Delta t}}{\omega_d \Delta t^2} - \frac{\sin(2\theta)}{\omega_n \Delta t^2}\right)
\end{aligned} \tag{C-22}$$

And for part **D** of (C-19), noting that $\frac{\mathrm{d}\phi_{n+1}}{\mathrm{d}t_{n+1}} = \frac{\phi_{n+1}-\phi_n}{\Delta t}$, we find:

$$\begin{aligned}
\frac{\mathrm{d}}{\mathrm{d}t_{n+1}} & \left[\frac{\phi_{n+1}}{\omega_d\omega_n}\left(\cos(\theta) - \frac{\sin(\omega_d\Delta t - 2\theta)\, e^{-\zeta\omega_n\Delta t} + \sin(2\theta)}{\omega_n\Delta t}\right)\right] \\
&= \frac{\phi_{n+1}-\phi_n}{\omega_d\omega_n\Delta t}\cos(\theta) - \frac{\phi_{n+1}-\phi_n}{\omega_d\omega_n\Delta t}\frac{\sin(\omega_d\Delta t - 2\theta)e^{-\zeta\omega_n\Delta t}}{\omega_n\Delta t} \\
&\quad - \frac{\phi_{n+1}}{\omega_d\omega_n}\left(\frac{\cos(\omega_d\Delta t - \theta)\, e^{-\zeta\omega_n\Delta t}}{\Delta t} - \frac{\sin(\omega_d\Delta t - 2\theta)\, e^{-\zeta\omega_n\Delta t}}{\omega_n\Delta t^2}\right) \\
&\quad - \frac{\phi_{n+1}-\phi_n}{\omega_d\omega_n\Delta t}\frac{\sin(2\theta)}{\omega_n\Delta t} - \frac{\phi_{n+1}}{\omega_d\omega_n}\frac{\sin(\omega_d\Delta t - 2\theta)\, e^{-\zeta\omega_n\Delta t}}{\omega_n\Delta t^2}
\end{aligned} \tag{C-23}$$

Fortunately, when substituting the above acquired terms back in (C-19), some terms from part **C** and **D** cancel out. The substitution eventually yields:

$$\begin{aligned}
\dot{\eta}_{n+1} &= -\eta_n\frac{\omega_n^2}{\omega_d}\sin(\omega_d\Delta t + 2\theta)\, e^{-\zeta\omega_n\Delta t} \\
&\quad + \left(\dot{\eta}_n + 2\,\zeta\,\omega_n\eta_n\right)\frac{\omega_n}{\omega_d}\cos(\omega_d\Delta t + \theta)\, e^{-\zeta\omega_n\Delta t} \\
&\quad + \frac{\phi_n}{\omega_d\omega_n}\left(\frac{\cos(\omega_d\Delta t - \theta)\, e^{-\zeta\omega_n\Delta t}}{\Delta t} + \omega_n\sin(\omega_d\Delta t)\, e^{-\zeta\omega_n\Delta t} - \frac{\cos(\theta)}{\Delta t}\right) \\
&\quad + \frac{\phi_{n+1}}{\omega_d\omega_n}\left(-\frac{\cos(\omega_d\Delta t - \theta)\, e^{-\zeta\omega_n\Delta t}}{\Delta t} + \frac{\cos(\theta)}{\Delta t}\right)
\end{aligned} \tag{C-24}$$

C-1-3 The matrix recurrence algorithm

Equations (C-18)and (C-24) indicate that advancing the solution from t_n to t_{n+1} can be performed by applying the matrix recurrence procedure.

First recall:

$$\begin{aligned}
h^{(-2)}(t) &= -\frac{\sin(\omega_d t - 2\theta)}{\omega_d\omega_n^2}\, e^{-\zeta\omega_n t} \\
h^{(-1)}(t) &= -\frac{\cos(\omega_d t - \theta)}{\omega_d\omega_n}\, e^{-\zeta\omega_n t} \\
h^{(0)}(t) &= \frac{\sin(\omega_d t)}{\omega_d}\, e^{-\zeta\omega_n t} \\
h^{(1)}(t) &= \frac{\omega_n}{\omega_d}\cos(\omega_d t + \theta)\, e^{-\zeta\omega_n t} \\
h^{(2)}(t) &= -\frac{\omega_n^2}{\omega_d}\sin(\omega_d t + 2\theta)\, e^{-\zeta\omega_n t}
\end{aligned}$$

Next, define these two constants:

$$\begin{aligned}
c_1 &= \frac{\cos\theta}{\omega_d\omega_n} \\
c_2 &= \frac{\sin 2\theta}{\omega_d\omega_n^2}
\end{aligned}$$

Now, the recursive scheme is given by rewriting (C-18)and (C-24) to:

$$\begin{aligned}\begin{bmatrix}\eta_{n+1}\\ \Delta t\,\dot{\eta}_{n+1}\end{bmatrix} &= \begin{bmatrix}h^{(1)}(\Delta t)+2\zeta\omega_n\,h^{(0)}(\Delta t) & \frac{h^{(0)}(\Delta t)}{\Delta t}\\ \Delta t\,h^{(2)}(\Delta t)+2\zeta\omega_n\Delta t\,h^{(1)}(\Delta t) & h^{(1)}(\Delta t)\end{bmatrix}\begin{bmatrix}\eta_n\\ \Delta t\,\dot{\eta}_n\end{bmatrix}\\ &+\begin{bmatrix}h^{(-1)}(\Delta t)-\frac{h^{(-2)}(\Delta t)}{\Delta t}+\frac{c_2}{\Delta t} & c_1+\frac{h^{(-2)}(\Delta t)}{\Delta t}-\frac{c_2}{\Delta t}\\ -h^{(-1)}(\Delta t)+\Delta t\,h^{(0)}(\Delta t)-c_1 & h^{(-1)}(\Delta t)+c_1\end{bmatrix}\begin{bmatrix}\phi_n\\ \phi_{n+1}\end{bmatrix}\end{aligned} \tag{C-25}$$

C-2 Rigid Body Mode

A similar derivation can be done for rigid body modes. First the undamped RBM is briefly discussed. Next, the damped case is discussed in a similar way as the vibration mode.

C-2-1 Undamped RBM

Fortunately, the derivation of the recursive scheme for the undamped rigid body mode is slightly simpler. The mode is subjected to the following equation of motion:

$$\ddot{\eta}(t) = \phi(t) \tag{C-26}$$

Trough the Laplace domain the following expression for the modal amplitude can be derived:

$$s^2\eta(s) - s\eta(0) - \dot{\eta}(0) = \phi(s) \tag{C-27}$$

$$\eta(s) = \frac{\eta(0)}{s} + \frac{\dot{\eta}(0)}{s^2} + \frac{\phi(s)}{s^2} \tag{C-28}$$

$$\eta(t) = \eta(0) + \dot{\eta}(0)\,t + \int_0^t \phi(\tau)(t-\tau)\,\mathrm{d}\tau \tag{C-29}$$

Remember the piecewise linear assumption (C-11a) for excitation $\phi(t)$. Now solving the convolution integral and implementing stepping from t_n to t_{n+1} results in:

$$\eta_{n+1} = \eta_n + \dot{\eta}_n\,t + \phi_n\frac{\Delta t^2}{3} + \phi_{n+1}\frac{\Delta t^2}{6} \tag{C-30}$$

Its derivative with respect to t_{n+1} is then given by:

$$\dot{\eta}_{n+1} = \dot{\eta}_n + \frac{\phi_n + \phi_{n+1}}{2}\Delta t \tag{C-31}$$

And finally, the latter two equations combine to the recursive scheme for the undamped rigid body mode:

$$\begin{bmatrix}\eta_{n+1}\\ \Delta t\,\dot{\eta}_{n+1}\end{bmatrix} = \begin{bmatrix}1 & 1\\ 0 & 1\end{bmatrix}\begin{bmatrix}\eta_n\\ \Delta t\,\dot{\eta}_n\end{bmatrix} + \frac{\Delta t^2}{6}\begin{bmatrix}2 & 1\\ 3 & 3\end{bmatrix}\begin{bmatrix}\phi_n\\ \phi_{n+1}\end{bmatrix} \tag{C-32}$$

C-2-2 Damped RBM

Finding the recursive scheme for the damped RBM is analogue to the derivation of scheme for the vibration mode. The modal equation of motion is given by

$$\ddot{\eta}(t) + \alpha\,\dot{\eta}(t) = \phi(t) \tag{C-33}$$

An expression for the modal amplitude $\eta(t)$ can again be found using a transformation trough the Laplace domain.

$$\mathcal{L}\left\{\ddot{\eta}(t) + \alpha\,\dot{\eta}(t)\right\} = \mathcal{L}\left\{\phi(t)\right\} \tag{C-34}$$

$$s^2\eta(s) - s\eta(0) - \dot{\eta}(0) + \alpha(s\eta(s) - \eta(0)) = \phi(s) \tag{C-35}$$

$$\eta(s) = \frac{\eta(0)}{s+\alpha} + \frac{\dot{\eta}(0) + \alpha\,\eta(0)}{s^2 + \alpha\,s} + \frac{\phi(s)}{s^2 + \alpha\,s} \tag{C-36}$$

Now by defining the modal Impulse Response Function and its derivative, using

$$\mathcal{L}^{-1}\left\{\frac{1}{s^2 + \alpha\,s}\right\} = h(t) = \frac{1 - e^{-\alpha\,t}}{\alpha} \tag{C-37}$$

$$\mathcal{L}^{-1}\left\{\frac{1}{s + \alpha}\right\} = \dot{h}(t) = e^{-\alpha\,t} \tag{C-38}$$

and applying the inverse Laplace transformation again, we can set up the expression for the modal amplitude $\eta(t)$ as

$$\eta(t) = \eta(0)\,\dot{h}(t) + \left(\dot{\eta}(0) + \alpha\,\eta(0)\right)h(t) + \int_0^t \phi(\tau)\,h(t-\tau)\,\mathrm{d}\tau \tag{C-39}$$

Similar as before, the initial conditions are preserved in the expression and therefore substituting time interval $[0;t]$ with $[t_n;t_{n+1}]$ yields a recursive expression:

$$\begin{aligned}\eta_{n+1} =& \eta_n\,\dot{h}(\Delta t) + \left(\dot{\eta}_{n+1} + \alpha\,\eta_n\right)h(\Delta t) \\ &+ \int_{t_n}^{t_{n+1}} \phi(\tau)\,h(t_{n+1}-\tau)\,\mathrm{d}\tau\end{aligned} \tag{C-40}$$

Recall from (C-9), the convolution integral can be solved as follows:

$$\begin{aligned}\int_{t_n}^{t_{n+1}} \phi(\tau)\,h(t_{n+1}-\tau)\,\mathrm{d}\tau =& \underbrace{\phi(\tau)\int h(t_{n+1}-\tau)\mathrm{d}\tau\Big|_{t_n}^{t_{n+1}}}_{\mathbf{A}} \\ &\underbrace{-\int_{t_n}^{t_{n+1}} \dot{\phi}(\tau)\int h(t_{n+1}-\tau)\mathrm{d}\tau\mathrm{d}\tau}_{\mathbf{B}}\end{aligned} \tag{C-41}$$

Similar as in section C-1-3, some derivatives and primitives of $h(t)$ can be derived:

$$h^{(-2)}(t) = \frac{t^2}{2\alpha} - \frac{e^{-\alpha\,t}}{\alpha^3} \tag{C-42a}$$

$$h^{(-1)}(t) = \frac{t}{\alpha} + \frac{e^{-\alpha\,t}}{\alpha^2} \tag{C-42b}$$

$$h^{(0)}(t) = \frac{1 - e^{-\alpha\,t}}{\alpha} \tag{C-42c}$$

$$h^{(1)}(t) = e^{-\alpha\,t} \tag{C-42d}$$

$$h^{(2)}(t) = -\alpha\,e^{-\alpha\,t} \tag{C-42e}$$

Also recall the assumption for piecewise linear excitation force from equation (C-11a).

Starting by solving part **A** of (C-41)

$$\phi(\tau)\int h(t_{n+1}-\tau)\mathrm{d}\tau\Big|_{t_n}^{t_{n+1}}$$

$$\begin{aligned}
&= \left(\phi_n \frac{t_{n+1}-\tau}{\Delta t} + \phi_{n+1}\frac{\tau - t_n}{\Delta t}\right)\left(-\frac{t_{n+1}-\tau}{\alpha} - \frac{e^{-\alpha\,(t_{n-1}-\tau)}}{\alpha^2}\right)\Bigg|_{t_n}^{t_{n+1}} && \text{(C-43)}\\
&= \frac{-\phi_{n+1}}{\alpha^2} + \phi_n\left(\frac{\Delta t}{\alpha} + \frac{e^{-\alpha\,\Delta t}}{\alpha^2}\right) && \text{(C-44)}
\end{aligned}$$

Next, solving part **B** of (C-41)

$$\int_{t_n}^{t_{n+1}} \dot{\phi}(\tau)\int h(t_{n+1}-\tau)\mathrm{d}\tau\mathrm{d}\tau$$

$$\begin{aligned}
&= \frac{\phi_{n+1}-\phi_n}{\Delta t}\left(\frac{(t_{n+1}-\tau)^2}{2\,\alpha} - \frac{e^{-\alpha\,(t_{n+1}-\tau)}}{\alpha^3}\right)\Bigg|_{t_n}^{t_{n+1}} && \text{(C-45)}\\
&= \frac{\phi_{n+1}-\phi_n}{\Delta t}\left(-\frac{1}{\alpha^3} - \frac{\Delta t^2}{2\,\alpha} + \frac{e^{-\alpha\,\Delta t}}{\alpha^3}\right) && \text{(C-46)}
\end{aligned}$$

Now substitution of the latter two expression in (C-40) using (C-41)

$$\begin{aligned}
\eta_{n+1} =& \eta_n\, e^{-\alpha\,\Delta t} + \left(\dot{\eta}_{n+1} + \alpha\,\eta_n\right)\frac{1-e^{-\alpha\,\Delta t}}{\alpha}\\
&+ \phi_n\left(\frac{\Delta t}{\alpha} + \frac{e^{-\alpha\,\Delta t}}{\alpha^2} - \frac{1}{\alpha^3\,\Delta t} - \frac{\Delta t}{2\,\alpha} + \frac{e^{-\alpha\,\Delta t}}{\alpha^3\,\Delta t}\right) \qquad \text{(C-47)}\\
&+ \phi_{n+1}\left(-\frac{1}{\alpha^2} + \frac{1}{\alpha^3\,\Delta t} + \frac{\Delta t}{2\,\alpha} - \frac{e^{-\alpha\,\Delta t}}{\alpha^3\,\Delta t}\right)
\end{aligned}$$

Again, an expression for the modal velocity is required. Therefore the derivative of the modal amplitude with respect to t_{n+1} is taken, which is split into three different parts:

$$\begin{aligned}
\frac{\mathrm{d}\eta_{n+1}}{\mathrm{d}t_{n+1}} = \dot{\eta}_{n+1} =& \underbrace{\frac{\mathrm{d}}{\mathrm{d}t_{n+1}}\left[\eta_n\, e^{-\alpha\,\Delta t} + \left(\dot{\eta}_{n+1}+\alpha\,\eta_n\right)\frac{1-e^{-\alpha\,\Delta t}}{\alpha}\right]}_{\mathbf{A}}\\
&+ \underbrace{\frac{\mathrm{d}}{\mathrm{d}t_{n+1}}\left[\phi_n\left(\frac{\Delta t}{\alpha} + \frac{e^{-\alpha\,\Delta t}}{\alpha^2} - \frac{1}{\alpha^3\,\Delta t} - \frac{\Delta t}{2\,\alpha} + \frac{e^{-\alpha\,\Delta t}}{\alpha^3\,\Delta t}\right)\right]}_{\mathbf{B}} \qquad \text{(C-48)}\\
&+ \underbrace{\frac{\mathrm{d}}{\mathrm{d}t_{n+1}}\left[\phi_{n+1}\left(-\frac{1}{\alpha^2} + \frac{1}{\alpha^3\,\Delta t} + \frac{\Delta t}{2\,\alpha} - \frac{e^{-\alpha\,\Delta t}}{\alpha^3\,\Delta t}\right)\right]}_{\mathbf{C}}
\end{aligned}$$

Starting with solving part **A** of (C-48):

$$\frac{\mathrm{d}}{\mathrm{d}t_{n+1}}\left[\eta_n\, e^{-\alpha\,\Delta t} + \left(\dot{\eta}_{n+1} + \alpha\,\eta_n\right)\frac{1-e^{-\alpha\,\Delta t}}{\alpha}\right]$$

$$= -\alpha\,\eta_n\, e^{-\alpha\,\Delta t} + \left(\dot{\eta}_{n+1} + \alpha\,\eta_n\right)e^{-\alpha\,\Delta t} \tag{C-49}$$

Next, solving part **B** of (C-48):

$$\frac{\mathrm{d}}{\mathrm{d}t_{n+1}}\left[\phi_n\left(\frac{\Delta t}{\alpha} + \frac{e^{-\alpha\,\Delta t}}{\alpha^2} - \frac{1}{\alpha^3\,\Delta t} - \frac{\Delta t}{2\,\alpha} + \frac{e^{-\alpha\,\Delta t}}{\alpha^3\,\Delta t}\right)\right]$$

$$= \phi_n\left(\frac{1}{\alpha} - \frac{e^{-\alpha\,\Delta t}}{\alpha} + \frac{1}{\alpha^3\,dt^2} - \frac{1}{2\alpha} - \frac{e^{-\alpha\,\Delta t}}{\alpha^2\,\Delta t} - \frac{e^{-\alpha\,\Delta t}}{\alpha^3\,\Delta t^2}\right) \tag{C-50}$$

And finally solving part **C** of (C-48):

$$\frac{\mathrm{d}}{\mathrm{d}t_{n+1}}\left[\phi_{n+1}\left(-\frac{1}{\alpha^2} + \frac{1}{\alpha^3\,\Delta t} + \frac{\Delta t}{2\,\alpha} - \frac{e^{-\alpha\,\Delta t}}{\alpha^3\,\Delta t}\right)\right]$$

$$\begin{aligned} &= \frac{\phi_{n+1}-\phi_n}{\Delta t}\left(-\frac{1}{\alpha^2} + \frac{1}{\alpha^3\,\Delta t} + \frac{\Delta t}{2\,\alpha} - \frac{e^{-\alpha\,\Delta t}}{\alpha^3\,\Delta t}\right)\\ &\quad + \phi_{n+1}\left(-\frac{1}{\alpha^3\,dt^2} + \frac{1}{2\alpha} + \frac{e^{-\alpha\,\Delta t}}{\alpha^2\,\Delta t} + \frac{e^{-\alpha\,\Delta t}}{\alpha^3\,\Delta t^2}\right)\end{aligned} \tag{C-51}$$

Substituting the above acquired terms back into (C-48) then yields:

$$\begin{aligned}\dot{\eta}_{n+1} &= -\alpha\,\eta_n\, e^{-\alpha\,\Delta t} + \left(\dot{\eta}_{n+1} + \alpha\,\eta_n\right)e^{-\alpha\,\Delta t}\\ &\quad + \phi_n\left(\frac{1}{\alpha} - \frac{e^{-\alpha\,\Delta t}}{\alpha} - \frac{1}{\alpha} - \frac{e^{-\alpha\,\Delta t}}{\alpha^2\,\Delta t} + \frac{1}{\alpha^2}\right)\\ &\quad + \phi_{n+1}\left(-\frac{1}{\alpha^2\,\Delta t} + \frac{1}{\alpha} + \frac{e^{-\alpha\,\Delta t}}{\alpha^2\,\Delta t}\right)\end{aligned} \tag{C-52}$$

Now recall equations (C-42) and define the following constants:

$$\begin{aligned} c_1 &= -\frac{1}{\alpha^2}\\ c_2 &= -\frac{1}{\alpha^3}\end{aligned}$$

Now eq (C-47) and (C-52) can again be rewritten to the recursive matrix scheme which was given by (C-25):

$$\begin{aligned}\begin{bmatrix}\eta_{n+1}\\ \Delta t\,\dot{\eta}_{n+1}\end{bmatrix} &= \begin{bmatrix} h^{(1)}(\Delta t) + 2\zeta\omega_n\, h^{(0)}(\Delta t) & \frac{h^{(0)}(\Delta t)}{\Delta t}\\ \Delta t\, h^{(2)}(\Delta t) + 2\zeta\omega_n \Delta t\, h^{(1)}(\Delta t) & h^{(1)}(\Delta t)\end{bmatrix}\begin{bmatrix}\eta_n\\ \Delta t\,\dot{\eta}_n\end{bmatrix}\\ &+ \begin{bmatrix} h^{(-1)}(\Delta t) - \frac{h^{(-2)}(\Delta t)}{\Delta t} + \frac{c_2}{\Delta t} & c_1 + \frac{h^{(-2)}(\Delta t)}{\Delta t} - \frac{c_2}{\Delta t}\\ -h^{(-1)}(\Delta t) + \Delta t\, h^{(0)}(\Delta t) - c_1 & h^{(-1)}(\Delta t) + c_1\end{bmatrix}\begin{bmatrix}\phi_n\\ \phi_{n+1}\end{bmatrix}\end{aligned} \tag{C-53}$$

Bibliography

[1] R. Courant, K. Friedrichs, and H. Lewy. Über die partiellen Differenzengleichungen der mathematischen Physik. *Mathematische Annalen*, 100(1):32–74, December 1928.

[2] D. de Klerk, D. J. Rixen, and S. N. Voormeeren. General Framework for Dynamic Substructuring: History, Review and Classification of Techniques. *AIAA Journal*, 46(5):1169–1181, May 2008.

[3] Dennis de Klerk, Daniel J. Rixen, S. N. Voormeeren, and F. Pasteuning. Solving the RDoF Problem in Experimental Dynamic Substructuring. In *Proceedings of IMAC-XXVII: International Modal Analysis Conference, Orlando, FL*, Bethel, CT, 2008. Society for Experimental Mechanics.

[4] Etienne Balmès (Office National d'Etudes et de Recherches). Frequency domain identification of structural dynamics using the pole/residue parametrization. In *IMAC*, 1996.

[5] Bernard Friedland. *Control System Design: An Introduction to State-Space Methods.* Dover Publications, 2012.

[6] M. Géradin and D. Rixen. *Mechanical Vibrations. Theory and Application to Structural Dynamics.* Wiley & Sons, 2nd edition, 1997.

[7] N.M. Newmark. A Method of computation for structural dynamics. *Journal of the Engineering Mechanics Division*, 85(7):67–94, 1959.

[8] D. J. Rixen. A Substructuring Technique Based on Measured and Computed Impulse Response Functions of Components. In *Proceedings of the International Conference on Noise and Vicration Engineering (ISMA 2010), Leuven, Belgium, 20-22 September, 2010*, 2010.

[9] Daniel J. Rixen. Substructuring using Impulse Response Functions for Impact Analysis. In *Proceedings of the IMAC-XXVIII, February 1-4, 2010, Jacksonville, Florida, USA*, Bethel, CT, 2010. Society for Experimental Mechanics.

[10] Daniel J. Rixen and Nazgol Haghighat. Truncating the Impulse Responses of Substructures to Speed Up the Impulse-Based Substructuring. In *Proceedings of the SEM IMAC - XXX, Jacksonville, Florida, USA*, Bethel, CT, 2012. Society for Experimental Mechanics.

[11] Daniël D. van den Bosch, Maarten V. van der Seijs, and Dennis de Klerk. Validation of Blocked-Force Transfer Path Analysis with Compensation for Test Bench Dynamics. In *Conference Proceedings of the Society for Experimental Mechanics Series*, 2014.

[12] Tim van der Horst. Experimental dynamic substructuring using direct time-domain deconvolved impulse response functions. Master's thesis, Delft University of Technology, 2014.

[13] Maarten V. van der Seijs, Dennis de Klerk, Daniel J. Rixen, and Siamand Rahimi. Validation of Current State Frequency Based Substructuring Technology for the Characterisation of Steering Gear Vehicle Interaction. In *Proceedings of the XXXI International Modal Analysis Conference, Los Angeles, CA*, Conference Proceedings of the Society for Experimental Mechanics Series, Bethel, CT, 2013. Society for Experimental Mechanics.

[14] Maarten V. van der Seijs and Daniel J. Rixen. Efficient Impulse Based Substructuring using truncated impulse response functions and mode superposition. In *Proceedings of the International Conference on Noise and Vicration Engineering (ISMA 2012)*, Leuven, 2012.

[15] Maarten V. van der Seijs, Daniël D. van den Bosch, Daniel J. Rixen, and Dennis de Klerk. An Improved Methodology for the Virtual Point Transformation of Measured Frequency Response Functions in Dynamic Substructuring. In M. Papadrakakis, V. Papadopoulos, and V. Plevris, editors, *4th ECCOMAS Thematic Conference on Computational Methods in Structural Dynamics and Earthquake Engineering*, volume 2013, 2013.

[16] Maarten V. van der Seijs, Paul L. C. van der Valk, Tim van der Horst, and Daniel J. Rixen. Towards Dynamic Substructuring Using Measured Impulse Response Functions. In Matt Allen, Randy Mayes, and Daniel Rixen, editors, *Proceedings of the 32nd IMAC, A Conference and Exposition on Structural Dynamics, 2014*, pages 73–82. Springer International Publishing, 2014.

[17] Paul L. C. van der Valk and Daniel J. Rixen. An Effective Method for Assembling Impulse Response Functions to Linear and Non-linear Finite Element Models. In R. Mayes, D. Rixen, D.T. Griffith, D. De Klerk, S. Chauhan, S.N. Voormeeren, and M.S. Allen, editors, *Proceedings of the SEM IMAC - XXX, Jacksonville, Florida, USA*, Bethel, CT, 2012. Springer New York.

[18] W.-C. Wang and R.A. Scholtz. Signal design for infinite impulse response inverse filters. In *Proceedings of MILCOM '93 - IEEE Military Communications Conference*, volume 2, pages 460–464. IEEE, 1993.

[19] K. Worden and G.R. Tomlinson. *Nonlinearity in Structural Dynamics: Detection, Identification and Modelling.* Taylor & Francis, 2000.